Impact of the adaptive immune system in bone fracture healing

D i s s e r t a t i o n

zur Erlangung des akademischen Grades

d o c t o r r e r u m n a t u r a l i u m

(Dr. rer. nat.)

im Fach Biologie

eingereicht an der

Lebenswissenschaftlichen Fakultät

der Humboldt-Universität zu Berlin

von

Diplom-Biologin Claudia Schlundt

Präsidentin der Humboldt-Universität zu Berlin

Prof. Dr.-Ing. Dr. Sabine Kunst

Dekan der Lebenswissenschaftlichen Fakultät

Prof. Dr. Bernhard Grimm

Gutachter/innen:	1. Prof. Georg N. Duda
	2. Prof. Hans-Dieter Volk
	3. Prof. Andreas Radbruch
Tag der mündlichen Prüfung:	18. Juli 2017

Declaration of Academic Honesty

Hiermit erkläre ich, dass ich die vorliegende Arbeit selbstständig und eigenhändig sowie ohne unerlaubte fremde Hilfe und ausschließlich unter Verwendung der aufgeführten Quellen und Hilfsmittel angefertigt habe.

I herewith declare that I have prepared the present thesis autonomously by my own without unauthorized assistance and solely using the specified sources and equipment.

Berlin, March 13, 2017

Für Leonie

Danksagung

An dieser Stelle möchte ich die Gelegenheit nutzen um mich bei allen zu bedanken, die zum Gelingen meiner Dissertation beigetragen haben.

Ein herzlicher Dank geht an Herrn Prof. Georg N. Duda, dem Direktor des Julius Wolff Institutes, der mir die Möglichkeit gegeben hat meine Arbeit an diesem Institut durchzuführen. Des Weiteren danke ich ihm für die Übernahme des Erstgutachters.

Ein weiterer großer Dank geht an Herrn Prof. Hans-Dieter Volk. Ich danke ihm für die Übernahme des Zweitgutachters, aber im Besonderen für seine kritischen, aber stets hilfreichen Anmerkungen zu dem immunologischen Part meines Projektes.

Das größte und herzlichste Dankeschön geht an meine Mentorin Kate, die durch ihre begeisternde Art mein Interesse für das Projekt weckte. Vor allem danke ich ihr für ihre grenzenlose Bereitschaft auftretende experimentelle Schwierigkeiten zu meistern, stets hinter mir zu stehen und mich das ein oder andere Mal wieder aufzubauen! Ich danke dir Kate!

Ein lieber und großer Dank geht an Norma. An erster Stelle danke ich dir für deine große Hilfe bei experimentellen Arbeiten im Labor. Besonders danke ich dir aber für die vielen Gespräche außerhalb der Wissenschaft.

Ein Dankeschön geht natürlich auch an die gesamte AG Schmidt-Bleek: Christian, Hanna, Sebastian und Henrik. Danke für eure Zusammenarbeit. Hierbei danke ich vor allem Christian für viele fruchtende Gespräche fachlicher, aber auch privater Art. Des Weiteren möchte ich mich bei Susann und Carolin für die vielen schönen gemeinsamen Stunden im Institut, aber auch privater Natur bedanken.

Meine lieben Freunde, euch danke ich einfach dafür, dass es euch gibt!

Liebe Familie Schlundt, euch danke ich ebenfalls. Ohne euch wäre ich sicherlich nicht so weit gekommen.

Der größte Dank geht an Mathias. Ich danke dir für deine unbändige Geduld und deine oft notwendigen aufbauenden Worte während der Zeit meiner Promotion. Du weisst gar nicht, wie sehr du mich die letzten 5 Jahre unterstützt hast und wie viel mir das geholfen hat!!! Ich liebe dich.

Abstract

Bone fracture healing is a highly complex process involving different cell and tissue types. It consists of different but overlapping phases that have to be well organized and regulated for a successful healing outcome. Bone tissue possesses the remarkable capacity to fully regenerate after injury. However, in 10–15 % of patients, unsuccessful bone repair is still a preset problem that has to be considered. The bone and the immune system are highly interconnected. Components of the adaptive immune system play an indispensable role in bone regeneration, probably due to their cellular interactions and their secreted cytokine profile. For CD8+ terminally differentiated effector memory T cells (T_{EMRA}), a negative correlation of an increased amount and an impaired bone repair process was already shown in patients. The here presented PhD thesis focused on a deeper analysis of the impact of the adaptive immunity in bone regeneration in order to better understand their influence in tissue repair. More precisely, the interaction of CD4+ regulatory T cells (T_{Reg}) during fracture healing was evaluated. T_{Reg} are a promising candidate for playing a positive modulating role in bone repair. However, their sole influence in bone regeneration was not analyzed so far.

In a murine osteotomy model of a non-critical size defect, the spatial and temporal distribution of distinct immune and bone cell subsets was analyzed within the healing tissue of the osteotomized bone. Cells of the innate (macrophages) and adaptive (T and B cells) immunity are detectable throughout the whole healing cascade in the injured area. The appearance of anti-inflammatory M2 macrophages coincided with the formation of new vessels which reestablished the necessary oxygen and nutrition supply. M2 macrophages further co-localized with osteoblasts in the fracture gap indicating an orchestrating function of macrophages for the production of bone by osteoblasts. T and B cells also directly co-localized with osteoblasts and osteoclasts, respectively, in the early fracture healing phase. These results highlight the interconnectivity of immune and bone cells during regeneration which was not analyzed and shown in any other study before.

By adoptive transfer of freshly isolated murine regulatory T cells prior to osteotomy, an immunomodulatory approach to improve bone healing was conducted. The activation status of the adaptive immunity prior to surgery was included into this analysis. Mice possessing an unexperienced immune system (housing in an SPF environment) showed a consistent improved healing outcome after adoptive transfer of T_{Reg} in comparison to the control group 21 days post-osteotomy. However, mice with a more experienced immune system (semi-sterile housing environment) receiving an adoptive T_{Reg} transfer demonstrated a controversial healing outcome after 21 days: half of the mice showed a significantly improved and the other half a significantly poorer healing outcome. In the mice with a poorer healing outcome, a higher ratio between CD8+ effector T cells and T_{Reg} was observed. In a following proof of concept study, a pre-osteotomy defined ratio of CD8+ effector T cells and T_{Reg} could predict the healing outcome 21 days after adoptive transfer of T_{Reg} and osteotomy.

A potential positive impact of T_{Reg} in bone repair was confirmed in this study. However, the tremendous impact of the environment and thereby of the immune status prior to immunomodulation was also clearly demonstrated. Transferring these findings to the clinical situation reveals how individually each patient might react to the same immunomodulatory therapy and how this therapy could affect the results of the treatment in an unfavorable way. Hence, for the clinic, it is even more important to develop and to apply patient based treatment approaches in the field of immunotherapy considering the individual immune status of each patient prior to treatment.

Zusammenfassung

Die Heilung nach einem Knochenbruch ist ein sehr komplexer Prozess, an dem verschiedenste Zellen und Gewebe beteiligt sind. Sie verläuft in mehreren in einander übergehenden Phasen, die für einen erfolgreichen Heilungsverlauf klar reguliert sein müssen. Knochengewebe besitzt die einzigartige Fähigkeit sich nach einem Bruch komplett zu regenerieren. Dennoch zeigen 10–15 % der Patienten einen gestörten Heilungsverlauf und Heilungserfolg. Das Immunsystem ist mit dem Knochengewebe stark vernetzt. Immunzellen spielen eine entscheidende Rolle in der Frakturheilung durch die Sekretion spezifischer Zytokine. Für CD8+ T-Zellen konnte bereits ein negativer Einfluss auf den Frakturheilungsprozess gezeigt werden. Im Rahmen der hier präsentierten Doktorarbeit wurde der Einfluss der adaptiven Immunität, insbesondere der CD4+ regulatorischen T-Zellen, auf die Knochenheilung untersucht. Dadurch sollte ein besseres Verständnis über die Wirkung von regulatorischen T-Zellen in der Regeneration erlangt werden.
Unter Verwendung eines Maus-Osteotomy-Modelles wurde die zeitliche und räumliche Verteilung ausgewählter Immun- und Knochenzellen im osteotomierten Knochen über den Heilungsverlauf untersucht. Dabei konnte gezeigt werden, dass sowohl Zellen der angeborenen (Makrophagen), als auch der adaptiven (B- und T-Zellen) Immunität im gesamten Heilungsverlauf in der Frakturzone zu finden waren. Hierbei korrelierte das Auftreten von anti-inflammatorischen M2-Makrophagen mit der Revaskularisierung des Frakturbereiches. Desweiteren konnten M2-Makrophagen gleichzeitig mit Osteoblasten im Frakturbereich detektiert werden. Dies lässt eine regulatorische Funktion von Makrophagen auf die Bildung von neuem Knochengewebe durch Osteoblasten vermuten. B- und T-Zellen kolokalisierten ebenfalls mit Osteoblasten, aber auch mit Osteoklasten in der frühen Phase der Frakturheilung. Diese Ergebnisse zeigen deutlich die starke Interaktion zwischen dem Knochen- und dem Immunsystem. Systemische Veränderungen über den Heilungsprozess waren vor allem in der Population der Gedächtnis-T-Zellen, als auch der der regulatorischen T-Zellen zu sehen, und diese vorwiegend im Knochenmark.
Ein adaptiver Transfer frisch isolierter muriner regulatorischer T-Zellen vor dem Setzen der Osteotomie diente als immunmodulatorischer Ansatz um den Frakturheilungsprozess zu verbessern. Hierbei wurde desweiteren der Immunstatus der Mäuse vor OP berücksichtigt. Tiere mit einem weniger stark aktivierten Immunsystem (SPF-Haltung) zeigten nach Transfer regulatorischer T-Zellen konstant eine Verbesserung der Heilung im Vergleich zur Kontrollgruppe. Dem hingegen war bei den Mäusen mit einem stärker aktivierten Immunsystem (semi-sterile Haltung) ein kontroverser Heilungserfolg zu beobachten. Hierbei heilte eine Hälfte der Mäuse signifikant besser als die Kontrollgruppe und die andere Hälfte signifikant schlechter. Die Schlechtheiler zeigten eine höhere Ratio von CD8+ Effektor-T-Zellen zu regulatorischen T-Zellen im Vergleich zu den Gutheilern. In einer darauffolgenden *Proof-of-concept*-Studie konnte gezeigt werden, dass eine prä-OP definierte Ratio von CD8+ Effector-T-Zellen zu regulatorischen T-Zellen mit dem Heilungserfolg nach Osteotomie korrelierte.
Im Rahmen dieser Doktorarbeit konnte ein potentiell positiver Einfluss von regulatorischen T-Zellen auf den Frakturheilungsprozess bestätigt werden. Dennoch wurde auch der enorme Einfluss des prä-OP Immunstatus auf den Heilungserfolg deutlich gezeigt. Mit Hinblick auf den Patienten in der Klinik wird deutlich wie individuell jeder dieser auf eine immunmo-dulatorische Therapie reagieren kann und wie dadurch der Erfolg dieser Therapie (negativ) beeinflusst werden kann. Demzufolge ist es im Rahmen der Immuntherapie umso wichtiger Patienten-basierte Therapieformen zu entwickeln und anzuwenden, bei denen der individuelle Immunstatus eines jeden Patienten vor Anwendung der Therapie berücksichtigt wird.

List of Abbreviations

ACK	ammonium-chloride-potassium
APCs	antigen presenting cells
BCR	B cell receptor
BMD	bone mineral density
BMPs	bone morphogenetic proteins
BSA	bovine serum albumin
BV	bone volume
cAMP	cyclic adenosine monophosphate
CCR	CC chemokine receptor
CK	cathepsin k
CTLA	cytotoxic T lymphocyte-associated antigen
d	day
DAPI	4',6-diamidino-2-phenylindole
DCs	dendritic cells
DEREG	depletion of regulatory T cell
DNA	deoxyribonucleic acid
EDTA	ethylenediaminetetraacetic acid
eGFP	enhanced green fluorescence protein
EL	erythrocyte lysis
FACS	fluorescence-activated cell sorting
FBS	fetal bovine serum
FGF	fibroblast growth factor
FMO	fluorescence minus one
FOX	forkhead box
FSC	forward scatter
GITR	glucocorticoid-induced TNFR-related protein
HIF	hypoxia-inducible factors
HSCs	hematopoietic stem cells
IDO	indoleamine 2,3-dioxygenase
IFN	interferon
IGF	insulin-like growth factor
IHC	immunohistochemistry

IL	interleukin
IPEX	immune dysregulation, polyendocrinopathy, enteropathy, X-linked
iT_{Reg}	induced regulatory T cells
LN	lymph nodes
MACS	Magnetic activated cell sorting
M-CSF	macrophage colony-stimulating factor
MHC	major histocompatibility complex
µCT	micro–computed tomography
MP	Movat Pentachrome
MSCs	mesenchymal stromal cells
non-SPF	semi-sterile
nT_{Reg}	natural regulatory T cells
OC	osteocalcin
OPG	osteoprotegerin
PAMPs	pathogen-associated molecular patterns
PBS/ BSA	1x PBS with 1 % BSA and 0.1 % sodium azide
PBS	phosphate buffered saline
PDGF	platelet-derived growth factor
PFA	paraformaldehyde
PMA	phorbol-12-myristat-13-acetat
POC	proof of concept
PRRs	pattern recognition receptors
RANKL	receptor activator of NF-κ B ligand
ROI	region of interest
RT	room temperature
RUNX2	runt-related transcription factor 2
SPF	specific pathogen free
SSC	sideward scatter
T_{EF}	effector T cells
T_{Reg}	regulatory T cells
T_{Resp}	responder T cells
T_{CM}	central memory T cells
T_{EFM}	effector memory T cells

T_{EMRA}	terminally differentiated effector memory T cells
TBS	tris-buffered saline
TCR	T cell receptor
TGF	transforming growth factor
Th	T helper
TNF	tumor necrosis factor
TNFR	tumor necrosis factor receptor
TV	total callus volume
VEGF	vascular endothelial growth factor
VOI	volume of interest
WT	wild type

Contents

List of Figures

List of Tables

1 Introduction

Bone is an impressive tissue because next to liver, it is the only organ that possesses the capacity to fully self-repair without scar formation after injury. Thus, under normal healing conditions, after fracture, bone completely regenerates gaining the same biomechanical properties as the original bone. Although bone repair is for the most part a really efficient process, delayed or even non-unions are still considerable problems in today's society, especially in the aging population, resulting in higher burden for the patient itself but also for the socio-economic and health system [1, 2]. Therefore, a better understanding of the principle processes in fracture healing is necessary for the development of new and improved therapeutic strategies in order to overcome impaired bone repair.
The immune system is highly interconnected with the bone system and vice versa, leading to the introduction of an own research field at the beginning of the 21^{th} century focusing on the interplay of both systems: osteoimmunology [3]. Both, the innate and the adaptive immune systems play important roles in fracture healing, in the early as well as in the later healing phases [4, 5]. Immune cells are one of the first cells infiltrating the fracture area. Especially T cells, as part of the adaptive immunity, seem to be one of the key players in bone healing by determining the local cytokine milieu in the fracture area [6, 7, 8, 9, 10, 11, 12]. A pivotal role for T cells in the healing outcome of wounds was already shown by Barbul *et al.* [6] and Efron *et al.* [13] without identifying the finally responsible cell subset. For CD8+ T cells, we could already show that they have a negative impact on successful bone repair [4]. Regulatory T cells (T_{Reg}), a subpopulation of CD4+ T cells, are a promising candidate playing a crucial positive modulating role in bone regeneration [14, 15, 16, 17, 18]. In a murine calvarial defect model, the application of T_{Reg} together with bone marrow mesenchymal stromal cells led to advanced bone formation [15, 16, 17]. However, the understanding of the impact and mode of action of T_{Reg} under normal healing conditions is just at the beginning.
In my PhD thesis, a non-critical size defect murine osteotomy model was used in order to better understand the immune cell composition over the healing cascade of an unaltered healing process. After analyzing the impact of the immune system in bone regeneration in a normal healing situation, a possible immunomodulatory therapeutic approach to improve the healing outcome was investigated. Therefore, an adoptive transfer of regulatory T cells prior to surgery was done. Hereby, the status of the immune system of the recipient mice prior to surgery was considered into the analysis, due to a different housing of the mice: specific pathogen free (SPF) vs. semi-sterile (non-SPF) housing. In this respect, we could already show that the housing of mice has an influence on the outcome of an unaltered healing process comparing both conditions [4]. At the end of the project, a potential identified biomarker determining the healing outcome after osteotomy could be confirmed in a proof of concept study.

1.1 Bone tissue

Bone tissue serves as a scaffold for the body and is part of its musculoskeletal system enabling movement. Besides its mechanical function, it also has a protecting function for underlying organs (e. g. the sternum and the costal arches). It further functions as a reservoir for mineral salts (e. g. calcium and phosphate), hormones and harbors different cell and tissue types. Bone is a highly active and adaptable biomaterial in respect of its microarchitecture and shape, dependent on the mechanical stimuli from the environment the bone is exposed to, the strain stress [19]. Meaning, the bone is constantly remodeled to adapt to the changing loading conditions. This is enabled due to its unique structure (Chap. 1.1.1).

1.1.1 Structure of long bones

There exist two different types of bone in the human body: long bones (e. g. femur, tibia, humerus) and flat bones (e. g. scull, ileum). Within both bone forms, two main structural types of mature bone can be distinguished: trabecular (cancellous) bone and compact (lamellar) bone [20].
In the following, the structure of long bones will be further described. The overall shape of a long bone can be divided into 5 parts (Fig. 1.1): a proximal and distal epiphysis (ends of the bone), the adjacent metaphyses and the middle part, the long shaft, the diaphysis. The outer layer of the bone is the periosteum. The periosteum consists of two layers, harboring osteogenic (progenitors) cells and fibrous tissue, which enables the bone to widen [21]. The diaphysis, in which the medullary cavity is enclosed, is also coated with an inner layer, identified as the endosteum. The bone tissue itself consists of organic material, including osteogenetic cells (Chap. 1.1.2) and extracellular matrix (30 %), and of an inorganic part including minerals in the form of hydroxyapartite crystals (70 %) [22]. The extracellular matrix presents the ground substance of the bone. It mainly contains water, collagen fibers and proteoglycans, in which different cell types and minerals are embedded. The main collagen the bone is composed of is collagen type I. In cortical bone, the collagen fibers are organized as triple-helices which are orientated in regular layers, the lamellae, along the axis of the bone (Fig. 1.1). Thereby, there are concentrically arranged around a central canal, the Haversian canal. Next to the collagen fibers, the Haversian system contains blood vessels and lymphatic nerves (Fig. 1.1). In contrast, in trabeculae bone, the mineralized collagen fibers are orientated in parallel to each other, aligned along the stress they are exposed to. The methaphysial shaft of a long bone consists of compact bone, whereas trabecular bone is found within the ends of long bones. The basic unit of the cortical bone is the osteon (Fig. 1.1). It consists of the Haversian canal that ensures the vascular supply and the surrounding bone lamellae [23]. This central canal is further connected via canaliculi to osteocytes (Chap. 1.1.2.2) which are located within the concentric lamellae of the compact bone. The osteocytes itself are also interconnected via their canaliculi.

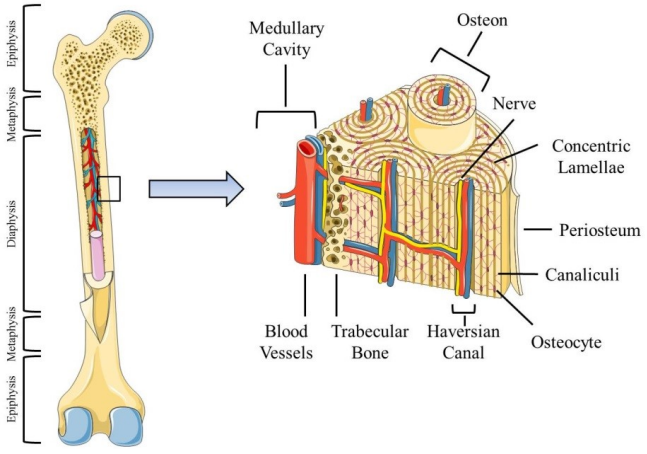

Figure 1.1: Schematic illustration of the structure of long bones (left) and a more detailed view of a segment of cortical bone (right). Long bones are divided into epiphyses, metaphysis and the diaphysis, containing the medullary cavity. Cortical bone is organized by osteons, consisting of an inner canal, the Haversian canal. The collagen fibers are orientated as concentric lamellae around the Haversian canal. Osteocytes are interconnected via canaliculi. Picture adapted from Medical Art (www.servier.de)

1.1.2 Cells of the bone matrix

The three main cell types of the bone matrix are bone producing osteoblasts (Chap. 1.1.2.1), osteocytes (Chap. 1.1.2.2) and bone resorbing osteoclasts (Chap. 1.1.2.3). In bone homeostasis, a close cross-talk between these cell types has to happen in order to enable a balanced bone resorption and formation at the right time and at the right place of the skeletal system. This ensures the adaptation of the bone to stress strains from the environment.
Bone is a highly dynamic organ due to its constant remodeling through the action of osteoblasts, osteoclasts and osteocytes. Julius Wolff published in 1892 the Wolff's Law which describes that the bony architecture, in particular the orientation of the trabeculae bone, is based on the mechanical forces the bone is exposed to. Meaning, the bone adapts to the applied forces from the mechanical environment [24].

1.1.2.1 Osteoblasts

Bone tissue is formed by osteoblasts. Under the stimulation by e. g. bone morphogenetic proteins (BMPs) and members of the Wnt pathway, mesenchymal stromal cells (MSCs) differentiate into osteoblasts. One of the master transcription factors that have to be expressed in the early stage of osteoblastic differentiation is the runt-related transcription factor 2 (RUNX2) [25]. Mature osteoblasts are characterized by their production and secretion of a non-mineralized organic bone matrix (osteoid), which consists among others of the bone matrix proteins osteocalcin and collagen type I. In a following step, this bone matrix is then mineralized. The final mineralized bone matrix mainly contains crystals of calcium and phosphate, the hydroxyapatite crystals. Mature osteoblasts are located along the bone surface having a cuboidal shape [25]. Time lapse fluorescence imaging approaches revealed a movement of mature osteoblasts over the bone surface of around 4–5 μm per hour [26]. The bone forming capacity of mature osteoblasts lasts about 100 days [21]. Afterwards, aged osteoblasts can undergo the following destinies: buried in the mineralized matrix as osteocytes (Chap. 1.1.2.2), rest on the bone surface as bone lining cells or undergo apoptosis. Bone lining cells are flat shaped aged osteoblasts that are found well organized on the bone surface where neither bone resorption nor bone formation are taking place. Thereby, they functionally represent the resting phase of bone remodeling. However, they seem to have a regulatory function in order to stimulate bone remodeling [27, 28].

1.1.2.2 Osteocytes

Osteocytes are star-shaped cells and are located within the mineralized bone matrix. They derive from mature osteoblasts. It is still unclear how the transition from mature aged osteoblasts to buried osteocytes takes place. In 2011, Dallas and Bonewald proposed a rather active then passive transition process [26]. Osteocytes becoming osteoblasts have to process dendrites, necessary for their viability and functionality which is an active process. It is probably that osteoblasts first has to arrest in cell mobility before getting embedded into the bone matrix and becoming an osteocyte. However, the elucidation of the exact mechanism of this transition process is still missing. Osteocytes are long living bone cells [29]. In earlier days it was thought that osteocytes are quiescent cells within the bone without specific function. Nowadays, it is already well accepted that osteocytes play an important role in regulating bone homeostasis through their function as mechanosensors [30]. They sense the mechanical stimuli and translate them into biochemical signals to cells on the bone surface through their canaliculi. Thereby, osteocytes regulate the activation of osteoblasts and osteoclasts (Chap. 1.1.2.3) during bone homeostasis and remodeling.

1.1.2.3 Osteoclasts

Osteoclasts present giant terminally differentiated multinucleated bone resorbing cells. They originate from mononuclear hematopoietic stem cells (HSCs) and develop under the stimulation by a variety of factors, of which the most important ones are macrophage colony-stimulating factor (M-CSF) and receptor activator of NF-κ B ligand (RANKL). RANKL binds to its receptor RANK on the surface of mononuclear pre-osteoclasts. M-CSF and RANKL are expressed by a variety of cells, like osteoblasts, osteocytes, stromal cells but also T cells as part of the adaptive immunity (Chap. 1.5). Another important factor in the process of osteoclast differentiation and activation is the soluble decoy receptor for RANKL: osteoprotegerin (OPG). Therefore, the RANK/RANKL/OPG axis is the regulator of osteoclast differentiation, activity and function [31]. After activation by RANKL binding, osteoclasts get polarized and a reorganization of their cytoskeleton occurs. Between the bone surface and the osteoclast, a ruffled border with a sealing zone is formed, representing a resorption pit named the Howship's lacunae. The basolateral secretory domains are not in contact with the bone surface [32, 33]. For bone resorption, lytic enzymes e. g. the collagenase Cathepsin K are secreted into the Howship's lacunae [34].

1.1.3 Development of the bone tissue

Bone tissue can develop via two different mechanisms: 1) through intramembranous ossification or 2) through endochondral ossification. In the process of intramembranous ossification, bone tissue develops directly out of MSCs that differentiated into osteoblasts before. During embryonic development, parts of the flat cranial bone are created via intramembranous ossification. During endochondral ossification, a cartilage template is first build that is then replaced by newly formed bone. This is how e. g. long bones are formed.

1.2 Fracture healing

Bone has the unique capacity to fully regenerate without scar formation after an injury. Under normal healing conditions, the regenerated bone possesses the same mechanical properties as the original bone before injury. Fracture healing is a highly complex process that involves different cells (e. g. MSCs, immune cells) and tissue types (e. g. bone, bone marrow, periosteum, endosteum, connective tissue, cartilage and the surrounding muscles). It has to be well organized for a successful healing outcome. Both, the bone healing process itself but also the outcome depend on the cellular and cytokine composition within the fracture area but also within the surrounding tissue serving as a rich source of migrating cells with different cytokine profiles.
A fracture can heal either directly via intramembranous ossification (primary or direct healing) or indirectly via endochondral ossification together with intramembranous bone formation (secondary or indirect healing) [35].The prerequisite for direct healing is a correct anatomical reduction of the fracture ends and a stable fixation [36]. Furthermore, it can occur as contact or gap healing, whereas the gap size is restricted to less than 800 μm to 1 mm [37]. In addition, no external callus is formed during this direct healing process. In contrast, indirect fracture healing benefits from micro-motions and weight-bearing. It occurs when the fracture ends have no direct contact and the gap size is too large for a direct healing. During secondary bone fracture healing, an external callus is formed in order to stabilize the fracture area during the healing process. Secondary bone fracture healing is the most common form of fracture healing and will be further illustrated in chapter 1.2.1.

1.2.1 Different phases of the fracture healing process

Bone fracture healing can be divided into four consecutive, but overlapping steps: 1) hematoma formation that is accompanied by an inflammation (divided into a pro- and an anti-inflammatory phase), 2) soft callus formation, 3) hard callus formation and finally 4) the remodeling phase (Fig. 1.2) [11]. A hematoma is formed in the injured area due to the blood influx after vessel disruption. This early fracture hematoma is an indispensable step for the whole healing cascade due to its highly angiogenetic and osteogenetic potential [38, 39, 10, 40]. Immune cells, including neutrophils, granulocytes and macrophages, are one of the first cells infiltrating the fracture area, already implicating their high impact for the initiation and progression of the healing cascade. In the initial phase, they are responsible for the clearance of the cell debris (macrophages) and for the recruitment of other cell types necessary for the regenerative healing cascade. The early fracture hematoma is characterized by hypoxia, an increase of lactate and the expression of the pro-inflammatory cytokines interleukin (IL)-1, IL-6 and TNFα [40, 18]. A timely well defined revascularization of the traumatized area is a prerequisite for a successful regenerated bone [41]. Low oxygen leads to the expression of the hypoxia-inducible factors (HIF)1α which further triggers the expression of pro-angiogenetic factors like vascular endothelial growth factor (VEGF) and the glucose transporter Glut1. In 2014, Schmidt-Bleek *et al.* could show in a study with a sheep osteotomy model that the two processes of inflammation and angiogenesis are interdependent on each other and have to be temporally finely regulated to enable regeneration [18]. After the occurrence of cells of the innate immunity, cells of the adaptive immune system and MSCs infiltrate the traumatized area. Both invade the fracture gap passively through the disrupted blood vessel but also by an active recruitment from the cells already present in the fracture gap from the bone marrow and from the surrounding tissue. After the initial inflammatory phase, granulation tissue refills the traumatized area that is further replaced by fibro-cartilage tissue [22], serving as a template for the formation of new bone. MSCs start to differentiate into cartilage producing chondrocytes that lead to the formation of fibro-cartilage and thus to a stabilization of the fracture area visible as an external soft callus. At the same time, intramembranous ossification happens periosteal at the fracture ends to further stabilize the soft callus. The cartilage tissue matures, becomes hypertrophic and starts to mineralize. Under the stimulation by e. g. TNFα, hypertrophic chondrocytes undergo apoptosis and are replaced by newly formed woven bone [42]. This step is the phase of hard callus formation. In the following remodeling phase, this woven bone is reorganized to lamellar bone according to the mechanical constrains that closely resembles the shape of the original bone. In humans, the remodeling phase can last up to several years depending on the age and general condition of the patient.

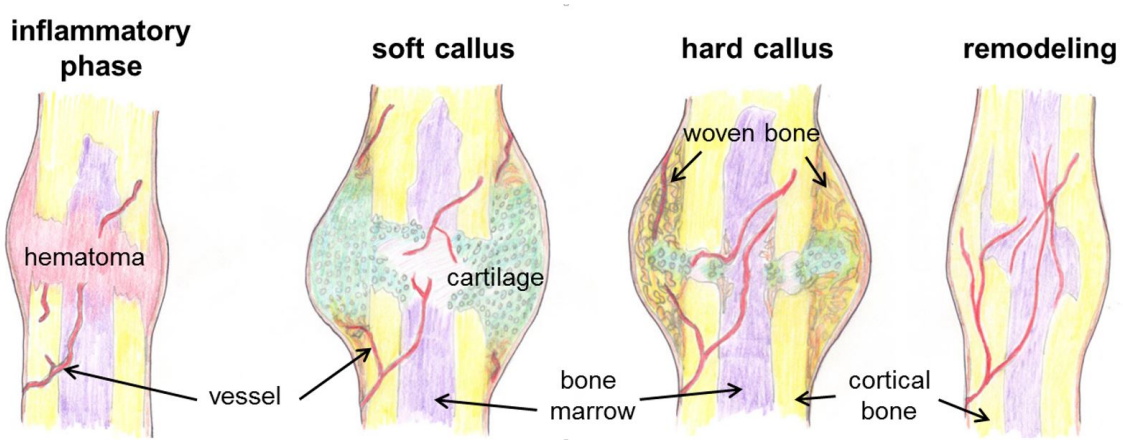

Figure 1.2: Schematic illustration of the different phases of the fracture healing process. The first phase is the hematoma formation with an accompanied pro- and anti-inflammatory reaction; this is followed by the soft callus formation, characterized by fibro-cartilage tissue in and around the fracture area; the following is the ossification of the fibro-cartilage the hard callus phase; and finally the remodeling phase; yellow = cortical bone, purple = bone marrow, red = blood vessels, green-blue = cartilage, brown = newly formed bone. Picture from [11].

1.2.2 Problems in bone fracture healing and current therapeutic approaches

Bone repair is a well regulated process involving several cell and tissue types that have to act together in consecutive but overlapping phases in order to enable the generation of a fully regenerated bone. Especially in the aging population, disturbances in fracture healing are a considerable problem for the patient itself but also for the socio-economic and health system. The causes for delayed or non-unions are various: among others age, autoimmune diseases (e. g. diabetes type 1), disturbed hormone homeostasis (estrogen decrease through menopause) or lifestyle (smoking) [43, 44, 45]. Different approaches exist to help impaired bone fracture healing. This includes the use of osteogenetic or osteoconductive materials, biophysical enhancement, growth factors, cell therapy or immunomodulation [46, 5]. For fractures of long bones with a critical size defect, the gold standard is still the transplantation of autologous spongiosa (aspirated from the iliac crest of the patient). Even though this is a successful treatment approach, a second surgery is necessary leading to further pain, possible co-morbidities and healing time for the patient. In addition, autologous spongiosa of a patient is not infinitely available. Another promising approach was the application of growth factors like BMPs, particular BMP-2 and BMP-7. Although both BMPs were approved by the U.S. Food and Drug Administration for e. g. clinical use of fresh open tibial fractures, they are still under debate due to possible unwanted side effects [47]. Other growth factors are currently under investigation: fibroblast growth factor (FGF), insulin-like growth factor (IGF), platelet-derived growth factor (PDGF) and transforming growth factor (TGF)α [11]. Postmenopausal women have a higher risk for osteoporosis due to a deficiency of estrogen that further leads to a disturbed mineral balance. Clinical studies already illustrated a promising effect of the administration of parathyroid hormone for this patient cohort [48]. MSCs are already well studied for their beneficial impact on bone healing. MSCs possess pro-angiogenetic and pro-osteogenetic properties as well as immunomodulatory functions [49]. First studies in humans already show the possible positive potential of MSCs in bone repair [50, 51]. A wide range of further clinical trials was initiated and partially already completed, however, the output is not published yet [52]. Modulation of the immune system is another approach that is more and more considered

for bone repair [12]. A negative impact of terminally differentiated CD8+ T cells (T_{EMRA}) was shown to correlate with delayed fracture healing in patients with a closed tibia-head fracture [4]. Therefore, a targeted immunotherapy could be a promising tool to treat patients suffering from impaired bone regeneration. Although the mentioned findings implicate a high impact of MSCs and immune cells in fracture healing, further knowledge and studies about the exact mechanisms of the interactions and interdependencies of both in the field of fracture healing are necessary. With this knowledge, new therapeutic treatment approaches could be developed in order to improve the healing outcome and thereby the lifestyle of patients with impaired bone repair.

1.3 Animal models for fracture repair

Patient material itself would reflect the best way the real healing situation in an injured bone. The disadvantages of human biopsies are that they are a limited source of material and that they just represent a snapshot in time (time point of surgery or harvest) of the healing process. Thus, it is not possible to make a statement about the healing process with its different phases. Furthermore, patient specific factors like age or diseases would influence the validity of the material. Animal models are a useful tool in research in general, but also for bone healing. In 2008, O'Loughlin published that rats are most often used as a model system in fracture repair (38 %) [53]. But also other animals are utilized in bone research: rabbit (19 %), mouse (15 %), sheep (11 %), dog (9 %), goat (4 %) and others (4 %). In the context of bone biomechanics, mammals like goat and sheep would mimic the human situation more effectively like rodents. However, these big animals have also disadvantages like higher costs in comparison to rodent animal models (purchasing and housing). Another important point for these animals is the fewer availability of research analyzing tools like specific antibodies. Especially in the field of immunological research questions, goats and sheep are less well explored due to their relative long breeding time, the impossibility to produce inbred strains, their size and their handling. In immunology, mouse is the best established animal model system. A high variety of different inbred strains useful for different research questions are characterized and available. In addition, a variety of knockout strains for components of the immune system are on the market. Furthermore, a high diversity of specific antibodies for the analyses or *in vivo* intervention approaches exists.

For the here presented study, the mouse strain C57BL/6N was used as a model system in bone repair which was combined with an immunological research question. This inbred strain was chosen because of its good fracture healing capacity and its strong immune competence [54, 55]. Although the healing process in mice won't completely reflect bone repair in humans, it is a useful tool to better understand basic processes taking place in the regenerating bone. Depending on the fracture type, a murine femur heals within 3–4 weeks after setting the fracture of a non-critical size defect. This allows the analysis of the complexity of the different healing phases in a relative short time span. The here presented study has next to its impact in the field of bone research also a high immunological aspect. Although translational capacity of findings from mice studies into the human situation is often under debate, we could already show that results from mice, especially from the C57BL/6N strain, reflect very well the human patient situation [4].

1.4 Osteoimmunology

The term osteoimmunology describes the interdisciplinary research field that combines the molecular and cellular interaction as well as interconnectivity of two research areas: The bone system and the immune system (Fig. 1.3, 1.4) [56]. The bone marrow is the place where HSCs reside. HSCs are the precursors for e. g. T and B lymphocytes. Already in 1994, Taichman *et al.* proposed a regulation of the HSC niche by cells of the bone system based on *in vitro* analyses with primary human osteoblasts [57]. A more up to date view of the HSC niche is given by Morrison and Scadden. They propose a so far not explainable important impact of the endosteal bone surface as well as close proximity to sinusoid blood vessels within the bone marrow on the localization and function of HSCs [58]. Next to harboring the precursor of T and B lymphocytes, the bone marrow is furthermore the place where B cells develop and memory T and B cell are stored [59, 60, 61]. This close spatial proximity of cells of the bone and of the immune system already strongly suggests that there has to be an active interaction between both systems. A regulation of cells of the skeletal system by cells of the immune system was for the first time described in the 1970s by the discovery that T cells, as component of the adaptive immunity, stimulate osteoclastogenesis by secreting osteoclast activating factors and thereby promote bone resorption [62, 63]. Arron and Choi introduced the term "osteoimmunology" to combine the interactions between the bone and the immune systems in 2000 after the detection that activated T cells express RANKL which binds to RANK on osteoclast precursors. This leads to the activation of the intrinsic signaling cascade and finally to osteoclastogenic differentiation [3]. Around the same time, a regulatory mechanism to avoid an uncontrolled bone resorption by activated T cells was shown by Takayanagi *et al.* [64]. Next to RANKL, activated T cells also secrete interferon (IFN)-γ which inhibits osteoclastic differentiation of osteoclast precursor cells after RANKL–RANK interaction.

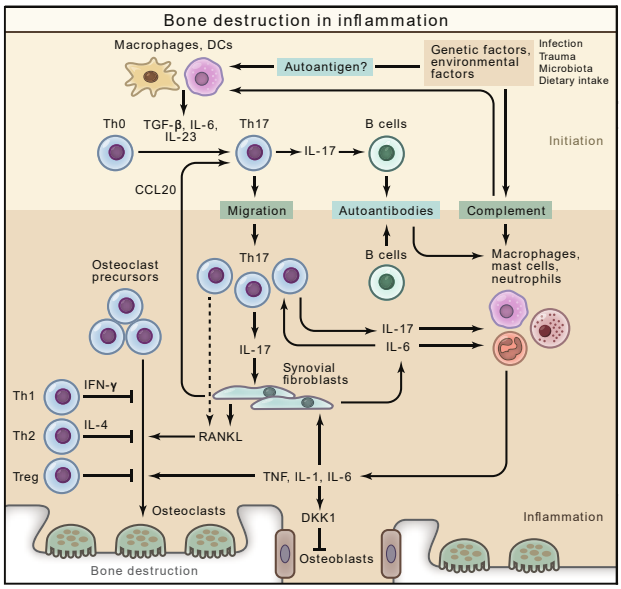

Figure 1.3: Illustration of the concept of bone destruction in the context of rheumatoid arthritis (RA). In short, in RA, in the synovium existing Th17 cells are responsible for an enhanced osteoclastogenesis and therefore for bone destruction under inflammatory conditions. They either produce RANKL by themselves, or induce the production of RANKL by synovial fibroblasts via IL-17. IL-17 further induces the production of pro-inflammatory cytokines like TNFa which further support osteoclastogenesis. Adapted from [56].

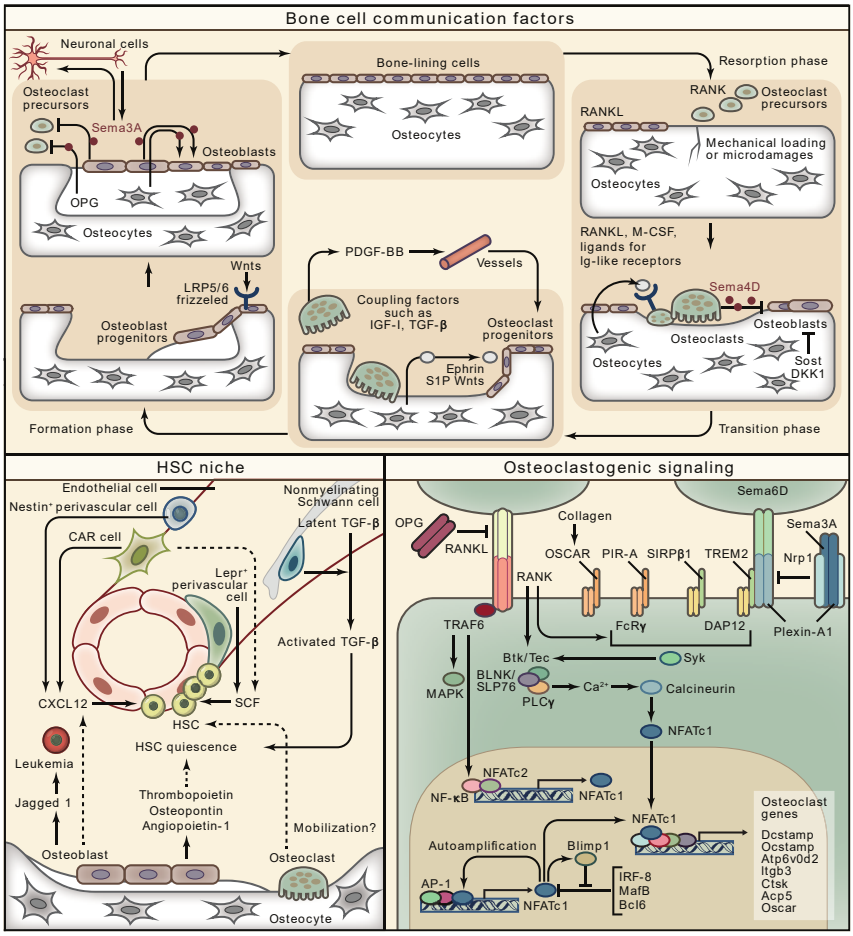

Figure 1.4: Schematic depiction of the complex and highly interwoven and connected interplay between the bone and the immune system on the cellular and molecular level. Upper picture: Osteoclasts and osteoblasts have to communicate in order to maintain the bony structure during normal bone homeostasis. This is realized e. g. via IGF-1 and TGF-β. Left lower picture: Besides CXCL12-abundant reticular (CAR) and Leptin receptor positive perivascular cells, osteoblasts and osteoclasts seem to interact in the maintenance of the HSC niche. Lower right picture: During osteoclastogenic differentiation, bone and immune cells share molecules, e. g. the RANK/RANKL axis. Adapted from [56].

Another important aspect underlying the strong interconnectivity between both systems is the changing bone phenotype in the context of (auto)-immune diseases or of mice deficient in distinct osteoimmunoregulatory molecules [65]. The strong and diverse interdependency between the bone and the immune system on the tissue, cellular and molecular level is further depicted in figure 1.3 and figure 1.4. In figure 1.3, the principle of the pathological mechanism leading to rheumatoid arthritis (RA) is illustrated. Evaluation of the pathological mechanism in RA was the beginning recognizing the interdependency between the immune and skeletal systems. In RA, Th17 cells are responsible for the characteristic bone destruction under inflammatory conditions [66]. In figure 1.4 illustrates the complex and highly interwoven and connected interplay between the bone and the immune system on the cellular and molecular level, including normal bone homeostasis (upper picture), the HSC niche (lower left picture) and shared molecules between the bone and the immune system exemplarily shown in the process of osteoclastogenesis (lower right picture). Both schemes clearly illustrate the complexity of the research field of osteoimmunology.

1.5 The immune system: Innate and adaptive immunity

Organisms are permanently exposed to pathogens. The immune system of an organism serves as a protection against theses potential disease agents.
In vertebrates, the immune system consists of two parts: the innate and the adaptive immunity which are highly interdependent on each other. For an effective functioning of the immune system, it has to be able to discriminate between self- and non-self-peptides. Both, the innate and the adaptive immunity are participating in this well-defined discrimination process. The discrimination between self- and non-self-peptides is a prerequisite for an effective fight against potential disease agents without fighting against self-peptides and thereby against the own body. The attack of body's own structures and thus an incorrect functional immunity is the cause for a variety of autoimmune diseases.
The innate immune system comprises the first line of defense via the pattern recognition receptors (PRRs), which include Toll-like or NOD-like receptors that recognize conserved molecular structures (like pathogen-associated molecular patterns (PAMPs)) on the surface of invading pathogens. It presents an evolutionarily ancient part of the immune system of vertebrates [67]. The following cell types belong to the innate immunity: mast cells, natural killer cells, monocytes, macrophages, dendritic cells (DCs) and granulocytes.
The adaptive (acquired) immunity is characterized by highly antigen-specific immune responses and the development of an immunological memory. The antigen-specificity is mediated by a huge variability of specific receptors expressed on the surface of lymphocytes: the T cell receptor (TCR) and the B cell receptor (BCR). T and B lymphocytes develop out of in the bone marrow lying HSCs, either in the thymus (T cells) or bone marrow (B cells). For both cell types, the specific antigen receptor consists of different gene segments (V, D and J) that have to be rearranged during development [68]. This process is called somatic recombination and enables the formation of the high variability of different T and B cell receptors. The recognition of the receptor specific antigen is mediated by the presentation of the antigen via specialized protein complexes on antigen presenting cells (APCs): the major histocompatibility complex (MHC).

The huge receptor diversity is a prerequisite for the great potential of the human body to recognize and react against a wide spectrum of different pathologic structures and peptides. B cells mediate the humoral (antibody mediated) immunity and T lymphocytes the cellular immunity.

1.5.1 T cells as part of the adaptive immunity

T cells are characterized by the expression of their antigen specific TCR that consists of two chains: α/β or γ/δ. The α/β T cells also express one of the co-receptors CD4 or CD8. Most of the T cells possess an α/β TCR and therefore the γ/δ T cells only present a minor proportion of the human T cell pool [69]. Naïve CD4+ and CD8+ T cells mature in the thymus. Functional single positive naïve T cells are released into the periphery after passing two consecutive processes within the thymus: 1) positive selection, T cells have to be able to recognize self-MHC molecules in a certain strength, and 2) negative selection, T cells are eliminated that recognize self-peptides (autoreactive T cells) [70]. After encountering their specific antigen due to an infection or immunization, naïve T cells get activated and start to differentiate and to clonally expand [71, 72]. CD4+ T cells can differentiate into the following effector subtypes, dependent on the type of pathogen and the time of antigen presence: Th1, Th2, Th17, induced T_{Reg} (Chap. 1.5.2) as well as follicular T cells and Th9 cells, each with a characteristic cytokine profile and specific effector function [73]. Besides

naïve CD4+ T cells, also so called natural T_{Reg} (nT_{Reg}) were released into the periphery from the thymus. These cells are characterized by the co-expression of CD25 (CD25++) and the transcription factor forkhead box (FOX) P3. After antigen clearance, most of the effector cells die but a small proportion resides as memory CD4+ or CD8+ T cells within the body. There exist different types of memory T cells: fast reacting effector memory T cells (T_{EFM}) and slower reacting central memory T cells (T_{CM}). The discrimination between T_{EFM} and T_{CM} was first done based on their functionality and on the expression of the homing receptor CC chemokine receptor (CCR) 7 [74]. CCR7- T_{EFM} display immediate effector function and migrate to inflamed tissue. In contrast, CCR7+ T_{CM} are able to home and enter into secondary lymphoid organs and display if any effector function. The existence of memory T cells enables the body to react faster to a certain antigen in case of a second challenge and provides long-term immunity against this pathogen. Naïve and memory T cells can be distinguished based on the expression of certain surface molecules. In humans, it is done on the basis of different isoforms of CD45, whereas naïve T cells express CD45RA and memory cells CD45RO. In mice, this is done be the expression of the memory marker CD44: naïve T cells are CD44- and memory T cells CD44+. The discrimination between T_{CM} and T_{EFM} is further realized as already mentioned by the expression of CCR7 or/and the cell adhesion molecule L-selectin (CD62L) for both, human and mouse (T_{CM}: CD62L+; T_{EFM}: CD62L-) [74, 75].

1.5.2 Regulatory T cells

T_{Reg} are a subpopulation of CD4+ T cells. They are highly specialized cells due to their immunosuppressive function and their importance in maintaining the immunological self-tolerance of an organism. T_{Reg} represent 5–10 % of the peripheral CD4+ T cells in human and in mice. They are characterized by the expression of the surface antigens CD4, CD25 (more precisely CD25high) and of the transcription factor FOX P3. FOX P3 is a member of the forkhead/winged-helix family of transcription factors and is the master transcription factor for the maintenance and function of T_{Reg} [76, 77]. These CD4+CD25highFOXP3+ T_{Reg} either develop directly in the thymus (indicated as natural T_{Reg}, nT_{Reg}) or can be induced in the periphery from naïve CD4+ T cells under different non-inflammatory and inflammatory conditions (indicated as induced T_{Reg}, iT_{Reg}) [78]. Both T_{Reg} subtypes are distinguishable by the methylation status of CpG islands in the promoter region within the foxp3 locus, the T_{Reg}-specific demethylated region, TSDR. In nT_{Reg}, this locus is demethylated and in iT_{Reg}, it is methylated. The demethylation correlates with a stable FOX P3 expression in these cells and thus with the suppressive capacity of these cells [79]. The existence of a thymic derived suppressive T cell population was first described by Sakaguchi *et al.* in 1982 [80]. In this *in vivo* study in mice, the development of an autoimmune disease after thymectomy of neonatal mice has been rescued by adoptive transfer of splenocytes or thymocytes from healthy syngeneic adult mice. They had been further characterized for the expression of the IL-2 receptor α chain (CD25) [81]. The knowledge that FOXP3 is indispensable for the maintenance and function of developed T_{Reg} was gained at the beginning of the 21^{th} century by several studies [76, 77]. One of the studies was related to the human disease immune dysregulation, polyendocrinopathy, enteropathy, X-linked (IPEX) syndrom, which is a rare lethal disorder of male humans with a dysregulated adaptive immunity. The mutant mouse model scurfy shares a wide range of phenotypical similarities with the human IPEX syndrome [82]. For both, human and mice, FOXP3 (and its protein scurfin) was identified as a new member of the forkhead/winged-helix family of transcription factors that is responsible for the development of the disorder by a dysregulated activity of activated

T cells due to the absence of FOXP3 [83, 84]. A wide range of analyses followed in order to elucidate the development and to understand the mode of action of T_{Reg} to suppress excess immune responses to self- and non-self-antigens by other immune cells (Chap. 1.5.3). nT_{Reg} develop directly in the thymus due to an intermediate interaction between the T cell receptor of single positive CD4+ T cells and self-peptides presented by MHC II molecules on thymic APCs in special niches in the thymic medulla. This intermediate recognition of self-antigens leads to an upregulation of CD25 and further to the expression of FOXP3 and other T_{Reg} -related surface molecules (like cytotoxic T lymphocyte-associated antigen (CTLA)-4 and the glucocorticoid-induced TNFR-related protein (GITR)) [85].

Besides the CD4+CD25highFOXP3+ T_{Reg}, there exist several other immunosuppressive, partially T_{Reg} -like cell types in the body: CD4+ Tr1 and Th3 cells, as well as CD8+ and CD8-CD4- suppressive T cells [86].

1.5.3 Mode of action of the suppressive capacity of regulatory T cells

T_{Reg} possess the capacity to suppress the proliferation and differentiation of CD4+ and CD8+ effector T cells *in vitro* and *in vivo*. Several mechanisms of T_{Reg} suppression are proposed so far: cell-cell contact dependent suppression, secretion of suppressive cytokines and modification of the function/killing of APCs. Bopp *et al.* showed that T_{Reg} can directly interact with activated T cells via gap junctions and can suppress their activity by the transfer of cyclic adenosine monophosphate (cAMP) via these gap junctions [87]. As a cell-cell contact independent pathway, T_{Reg} are able to produce adenosine via their surface molecules CD39 and CD73 (ectonucleotidases) from present extracellular nucleotides [88]. Adenosine was already shown to lead to lymphocyte depletion and immune deficiency by a T cell receptor triggered inhibition of T cell proliferation and upregulation of CD25. Furthermore, extracellular adenosine leads to an intracellular accumulation of cAMP in T cells [89]. Several *in vitro* studies carried out with human and murine T_{Reg} further implicated a cell-cell contact dependent suppressive mechanism via the perforin/granzyme pathway. In contrast, *in vivo* imaging studies rather revealed an indirect suppressive activity of T_{Reg} against several cell types (among others: CD4+ and CD8+ T cells, B cells, monocytes, DCs) via a direct interaction with APCs which further influence the activity of effector cells [90, 91, 92, 93, 94]. T_{Reg} can interact with DCs via the CTLA-4-–B7 axis and can thereby induce the expression of indoleamine 2,3-dioxygenase (IDO) of DCs which leads to an amino acid starvation for effector T cells [95, 96]. Besides the effect of T_{Reg} on cells of the immune system, they can further directly affect the function of non-immune tissue cells like visceral adipocytes and skeletal muscle cells [97, 98]. In the context of bone regeneration, Lei and colleagues proposed a model where T_{Reg} might promote tissue repair by a direct cell-cell contact with tissue resident osteoblasts or/and their precursors (MSCs) via the CD39-CD73 axis and thereby creating a pro-regenerative microenvironment [99].
Taken together, the above illustrated studies and findings illustrate just in part the wide spectrum of mechanisms applied by T_{Reg} in order to sustain the immunological balance in an organism and their differences in *in vitro* and *in vivo* settings. Additional investigations especially in *in vivo* conditions are needed to further enlighten the mode of action of T_{Reg} suppression. However, it does not seem to exist this one mechanism how T_{Reg} suppress the action of other (immune) cells. It is more likely to depend on the situation and circumstances which pathway T_{Reg} are using in order to inhibit or counter act unwanted immune reactions. This also enables their high flexibility to react to a variety of inflammatory and disease conditions within the body.

1.5.4 Impact of immune cells/ regulatory T cells in bone fracture healing

Several studies have already shown that immune cells play an essential role in tissue regeneration and especially in the process of bone fracture healing. In fracture repair, they are not only important in the early inflammatory but also in the later phases of the regeneration process [8, 5]. We could already show in a mouse osteotomy model that the lack of macrophages, a cell subpopulation of the innate immunity, disturbs bone fracture healing due to a delayed resorption of hypertrophic cartilage [5]. Macrophages are a heterogeneous cell population dependent on the microenvironment around them. Based on the Th1/Th2 nomenclature of T cells, they are also named M1 and M2 macrophages. M1 macrophages are the "classically activated" pro-inflammatory ones. In contrast, M2 are named "alternatively activated" macrophages. Based on their receptor and cytokine expression profile, they can exhibit different functions: anti-inflammatory (M2a), immune-regulatory (M2b) and pro-remodeling (M2c) [100]. Toben *et al.* showed in 2011 that in the absence of the adaptive immune system, bone formation is accelerated but also altered in a murine femur fracture model [101]. This finding indicates that the adaptive immune system could have at least in partial a negative impact on the regeneration process after bone injury. Indeed, a negative impact of CD8+ cytotoxic T cells was already shown by us in humans as well as in a murine osteotomy model [4]. T_{Reg} are one potential counterpart of negative acting cells in fracture repair and thereby represent a positively modulating cell population in bone healing. That T cells play a key role in tissue regeneration was already shown [6, 13]. Further studies implicate a positive effect of T_{Reg} on bone formation and regeneration. In an *in vitro* analysis, Zaiss *et al.* demonstrated a T_{Reg} mediated inhibition of osteoclastogenesis [14]. In *in vivo* follow up studies, a higher amount of T_{Reg} improved clinical signs of rheumatoid arthritis, led to more bone formation as well as inhibited bone loss under physiological and pathological conditions [15, 16]. Furthermore, T_{Reg} also led to advance bone healing in a murine calvarial defect model where they were applied in combination with autologous bone marrow MSCs [17]. A study realized in a sheep osteotomy model in which the early healing phase of a scar forming soft tissue hematoma was compared to a regenerating bone hematoma clearly demonstrated a higher amount of T_{Reg} in the bone hematoma in comparison to the soft tissue hematoma [18]. So far, the exact mechanism of T_{Reg} action on bone and other cells in fracture healing is not discovered (the question is: Is there just one mechanism?). However, the aforementioned results highlight the importance and the postulated positive impact of T_{Reg} in bone regeneration and bone disease related circumstances.
In the last few years, the pro-inflammatory Th17 cells, another subset of CD4+ T cells, was defined as one counterpart of T_{Reg} in immune homeostasis in general, but also in the context of bone related diseases. Th17 cells induce osteoclastogenesis either indirectly by inducing the expression of the pro-osteogenetic factor RANKL in MSCs or synovial fibroblasts or directly by producing high levels of the RANKL by themselves [102, 66]. Furthermore, Th17 cells are also promoting osteoblast differentiation, as shown in *in vitro* studies with human MSCs [103]. It is postulated that an imbalance of the ratio of Th17 and T_{Reg} cells is the cause for several bone disorders like RA, osteoporosis and periodontitis [104, 105].

1.6 Hypotheses and objectives of the project

Bone is the tissue where immune cells are formed, already implicating its impact on the immune system. But, how does the immune system affect or even control the bone system? Bone is a remarkable tissue due to its ability to fully self-repair after injury. Bone fracture healing is a very complex mechanism involving different cell types and the bone matrix. In the context of bone regeneration, so far, no study focused on a broader view on the tissue and cellular level, including a variety of cell types of the immune and bone system in order to better understand the underlying mechanism of the healing process.
Immunotherapy is a promising tool in order to improve the patient situation suffering from pathological diseases. CD4+CD25++FOXP3+ T_{Reg}, a subset of CD4+ T cells, are of special interest for immunotherapy due to their immunosuppressive function. They are furthermore characterized by their importance in maintaining the immunological self-tolerance of an organism. Their positive modulating effect in bone related diseases as well as in applications together with bone marrow MSCs was already shown.

Hypothesis 1: *Immune and bone cells interact during the specific bone healing phases. Specific healing phases show distinct distribution patterns of immune and bone cells.*

Hypothesis 2: *CD4+CD25++FOXP3+ T_{Reg} have a positive modulating effect in bone repair and improve the healing outcome after injury.*

Hypothesis 3: *The healing outcome after adoptive T_{Reg} transfer is dependent on the status of the adaptive immune system prior to osteotomy (SPF vs. semi-sterile (non-SPF) housing).*

In order to proof the hypotheses, the following objectives had to be addressed during my PhD thesis:

Objective 1: Analysis of the spatial and temporal distribution of distinct immune cell subsets in correlation towards tissue types over the healing process in a well-established mouse osteotomy model of a non-critical size defect.

Using a murine osteotomy model with a non-critical size defect of the left femur, the distribution of certain tissues within the fractured bone was analyzed via histology and micro-computed tomography (μCT). Furthermore, from the same animals, the local and temporal distribution of selected cellular components of the immune and bone system were investigated on consecutive bone sections via fluorescence-based immunohistochemistry. In addition, systemic changes of the immune cell composition during the healing process were investigated by flow cytometry.

Objective 2: Analysis of the ratios of selected cellular subsets of the adaptive immunity in mice without osteotomy housed under SPF and semi-sterile (non-SPF) conditions, respectively.

Objective 3: Analysis of the healing outcome of mice after adoptive transfer of T_{Reg} prior to osteotomy.

An immunomodulatory approach of adoptive transfer of murine T_{Reg} prior to osteotomy was chosen in order to analyze their impact in bone repair. This approach also included the status of the adaptive immune system of the osteotomized mice prior to surgery. In the here presented study, the healing outcome of the treated mice (adoptive transfer of T_{Reg}) was investigated via μCT and histology. An analysis of systemic changes was included and selected immune cell subsets were systemically analyzed via flow cytometry.

2 Materials

2.1 Chemicals

Chemical	Company
0.9 % Sodium Chloride	Fresenius Kabi Germany GmbH, Bad Homburg, Germany
Aceton	Sigma-Aldrich Chemie GmbH, München, Germany
ACK Lysing Buffer	Gibco-Life Technologies GmbH, Darmstadt, Germany
Alcian blue	Chroma GmbH & Co. KG, Münster, Germany
β-Mercaptoethanol	Sigma-Aldrich Chemie GmbH, München, Germany
Brilliant crocein acid fuchsin	Chroma GmbH & Co. KG, Münster, Germany
BSA, protease free	Sigma-Aldrich Chemie GmbH, München, Germany
Cell Proliferation Dye eF450	eBioscience, San Diego, CA, USA
EDTA	Carl Roth GmbH & Co. KG, Karlsruhe, Germany
FBS Superior	Biochrom AG, Berlin, Germany
Iron hematoxylin (after Weigert)	Chroma GmbH & Co. KG, Münster, Germany
n-hexane	Carl Roth GmbH & Co. KG, Karlsruhe, Germany
PBS (1x)	Gibco-Life Technologies GmbH, Darmstadt, Germany
PBS 10x, pH 7.2	Waldeck GmbH & Co. KG, Münster, Germany
Penicillin/Streptomycin (10.000 U Penicllin/ml, 10 mg Streptomycin/ml)	Sigma-Aldrich Chemie GmbH, München, Germany
Phosphotungstic acid	Chroma GmbH & Co. KG, Münster, Germany
RPMI 1640 with 2.0 g/l $NaHCO_3$, with stable Glutamine	Biochrom AG, Berlin, Germany
Saffron du Gâtinais	Chroma GmbH & Co. KG, Münster, Germany
Sodium Azide, extra pure	Merck KGaA, Darmstadt, Germany
Sodium Chloride	Merck KGaA, Darmstadt, Germany
Trizma Base	Sigma-Aldrich Chemie GmbH, München, Germany
Trizma Hydrochloride	Sigma-Aldrich Chemie GmbH, München, Germany
Tween-20	Merck KGaA, Darmstadt, Germany

2.2 General equipment

Product	Company
BD Vacutainer blood collection tube, EDTA coated	Becton Dickinson Bioscience, Heidelberg, Germany
cell strainer	Corning, Sigma-Aldrich, München, Germany
CellTrics filter, 30 µm	Sysmex Partec GmbH, Görlitz, Germany
culture dish (60 mm ⌀)	Corning, Sigma-Aldrich, München, Germany
15 ml Polypropolyne Conical Tube	Becton Dickinson Bioscience, Heidelberg, Germany
50 ml Polypropolyne Conical Tube	Becton Dickinson Bioscience, Heidelberg, Germany

Product	Company
5 ml Polystyrene Round-Bottom Tube	Becton Dickinson Bioscience, Heidelberg, Germany
Syringe Discardit II 2 ml	Becton Dickinson Bioscience, Heidelberg, Germany
Tissue Culture Plate, 96 Well, Flat Bottom	Becton Dickinson Bioscience, Heidelberg, Germany

2.3 Equipment for the isolation of regulatory T cells

Product	Company
CD4+CD25+ Regulatory T Cell Isolation Kit, mouse	Miltenyi Biotec GmbH, Bergisch Gladbach, Germany
LD Columns	Miltenyi Biotec GmbH, Bergisch Gladbach, Germany
MidiMACS Seperator	Miltenyi Biotec GmbH, Bergisch Gladbach, Germany
MiniMACS Seperator	Miltenyi Biotec GmbH, Bergisch Gladbach, Germany
MS Columns	Miltenyi Biotec GmbH, Bergisch Gladbach, Germany

2.4 Equipment for histology

Product	Company
Cryofilm 2C (10)	Section-Lab Co. Ltd., Hiroshima, Japan
Cryofilm 2C (9)	Section-Lab Co. Ltd., Hiroshima, Japan
Embedding Medium SCEM	Section-Lab Co. Ltd., Hiroshima, Japan
Microtome Blades SEC 35	Fisher Scientific, Schwerte, Germany
Object slide superfrost	Thermo Scientific Fisher, Waltham, MA, USA
Paraformaldehyde Solution 20 %, EM grade	Electron Microspcopy Sciences, Hatfield, PA, USA
Tissue Tek, OCT compound	Sakura Finetek Germany GmbH, Staufen, Germany

2.5 Media and buffer

Media/Buffer	Company
Cell culture medium complete (500 ml)	
RPMI 1640	450 ml
FBS	50 ml
Penicillin/Streptomycin	100 U/ml each
β-Mercaptoethanol	50 μM
Flow cytometry buffer PBS/BSA (500 ml)	
PBS (1x)	500 ml
BSA	5.0 g
Sodium Azide	0.5 g

Media/Buffer	Company
MACS buffer (500 ml)	
PBS (1x)	500 ml
BSA	2.5 g
EDTA	2 mM
Tris buffer (1 l)	
Trizma Hydrochloride	6.60 g
Trizma Base	0.90 g
Sodium Chloride	8.78 g

2.6 Medication and materials for the mouse osteotomy model

Product	Company
Bepanthen (+5 % Dexpanthenol)	Bayer Vital GmbH, Leverkusen, Germany
Buprenorphin	RB Pharmaceuticals Ltd, Berkshire, UK
Clindamycin	ratiopharm GmbH, Ulm, Germany
Fixator MouseExFix	RISystem AG, Davos, Switzerland
Gigli saw wire (0.66 mm)	RISystem AG, Davos, Switzerland
Inject® -F Tuberkulin-Spritze, 1 ml	B. Braun Melsungen AG, Melsungen, Germany
Isoflurane	FORENE, Abott GmbH & Co. KG, Wiesbaden, Germany
Ketamin	Actavis Switzerland AG, Regensdorf-Zürich, Switzerland
Medetomidine	Janssen-Cilag GmbH, Neuss, Germany
Sterican® Kanüle (size 18; 0.45 x 25 mm)	B. Braun Melsungen AG, Melsungen, Germany
Suture material Prolene 5.0	Ethicon, Norderstedt, Germany
Tramadol (100 mg/ml)	Gruenenthal, Brunn am Gebirge, Austria

2.7 Antibodies

2.7.1 Flow cytometry

Specificity/Antigen/Labeling	Company	Clone
α-mouse CCR7 Biotin	BioLegend, San Diego, CA, USA	4B12
α-mouse CD3ϵ PerCP	BioLegend, San Diego, CA, USA	145-2C11
α-mouse CD4 AF700	eBioscience, San Diego, CA, USA	RM4-5
α-mouse CD8a eF450	eBioscience, San Diego, CA, USA	53-6.7
α-mouse CD16/CD32 Purified	eBioscience, San Diego, CA, USA	93
α-mouse CD25 APC	BioLegend, San Diego, CA, USA	PC61
α-mouse CD25 APC-Cy7	BioLegend, San Diego, CA, USA	PC61
α-mouse CD44 APC-Cy7	Becton Dickinson Bioscience, Heidelberg, Germany	IM7

Specificity/Antigen/Labeling	Company	Clone
α-mouse CD44 PE-Cy7	Becton Dickinson Bioscience, Heidelberg, Germany	IM7
α-mouse CD62L APC	BioLegend, San Diego, CA, USA	MEL-14
α-mouse CD127 PE-Cy7	BioLegend, San Diego, CA, USA	A7R34
α-mouse/ rat FOXP3 FITC	eBioscience, San Diego, CA, USA	FJK-16s
α-mouse/ human Helios PE	BioLegend, San Diego, CA, USA	22F6
α-mouse NK-1.1 FITC	BioLegend, San Diego, CA, USA	PK136
α-mouse TCRβ chain PE	BioLegend, San Diego, CA, USA	H57-597
LIVE/DEAD Fixable Aqua Dead Cell Stain Kit (excitation: 405 nm)	Thermo Fisher Scientific, Waltham, MA, USA	-
Streptavidin PE-Texas Red	Becton Dickinson Bioscience, Heidelberg, Germany	-

2.7.2 Immunofluorescence histology

Specificity/Antigen/Labeling	Company	Clone
α-mouse B220 PE	Deutsches Rheumaforschungzentrum, Berlin, Germany	RA3.6B2
α-mouse CD4 AF594	Deutsches Rheumaforschungzentrum, Berlin, Germany	GK1.5
α-mouse CD8 PE	Abcam, Cambridge, United Kingdom	53-6.7
α-mouse CD68 FITC	AbD Serotec, Kidlington, United Kingdom	FA-11
α-mouse CD80 AF647	BioLegend, San Diego, CA, USA	16-10A1
α-mouse CD105	eBioscience, San Diego, CA, USA	MJ7/18
α-mouse CD206 PE	BioLegend, San Diego, CA, USA	C068C2
α-mouse Osteocalcin	Enzo Life Sciences, Lörrach, Germany	
α-rabbit AF647	Invitrogen, Karlsruhe, Germany	
α-rat AF954	Invitrogen, Karlsruhe, Germany	
α-CathepsinK	Abcam, Cambridge, United Kingdom	
α-Hif1α	Novus Biologicals LLC, Littleton, CO, USA	

2.7.3 Treg suppression assay — T cell receptor stimulating antibodies

Specificity/Antigen/Labeling	Company	Clone
α-mouse CD28 purified 0.5 mg/ml	eBioscience, San Diego, CA, USA	37.51
α-mouse CD3e purified 0.5 mg/ml	eBioscience, San Diego, CA, USA	145-2C11

2.7.4 CD25+ T cell depletion

Specificity/Antigen/Labeling	Company	Clone
α-mouse CD25, *in vivo* mab	Bio X Cell, Lebanon, NH, USA	PC-61.5.3

2.8 Recombinant protein

Product	Company
Recombinant Mouse IL-2, CF	R&D Systems, Minneapolis, MN, USA

2.9 Technical devices

Technical device	Company
Computed tomography scanner µCT Viva 40	SCANCO Medical AG, Brüttisellen, Switzerland
Confocal laser scanning microscope LSM 710	Carl Zeiss, Jena, Germany
Cryotome	Leica Biosystems, Nussloch, Germany
Flow cytometer LSR II	Becton Dickinson Bioscience, Heidelberg, Germany
Light microscope	Carl Zeiss, Jena, Germany

2.10 Software and analyzing programs

Software	Function	Company
Axiovision	Imaging and processing (Movat Pentachrome)	Carl Zeiss, Jena, Germany
FACS DIVA 6.1.3	Measurement software for flow cytometry	Becton Dickinson Bioscience, Heidelberg, Germany
FlowJo 9.6.4	Evaluation of flow cytometry data	Tree Star, Ashland, OR, USA
ImageJ 1.45s	Processing of images/histomorphometry	Open Source
MicroCT evaluation program 6.5-3	µCT evaluation	SCANCO Medical AG, Brüttisellen, Switzerland
PRISM 5.0	Graphics and statistics	GraphPad, La Jolla, CA, USA
SPSS 22	Statistics	IBM Deutschland GmbH, Ehningen, Germany
Zen 2011	Processing of images (IHC)	Carl Zeiss, Jena, Germany

3 Methods

3.1 Animal model

3.1.1 Mouse strain

For the *in vivo* analyses in this study, the mouse strain C57BL/6N (Charles River Laboratories, Wilmington, MA, United States of America) was used. C57BL/6N mice were selected based on their good fracture healing capacity and their strong immune competence [55, 54]. All experiments were done with female mice. Earlier studies already revealed differences in the healing capacity between male and female animals [106, 107]. In addition, in future studies, the question of the influence of the hormone status might become an important question. All animal experiments were carried out with ethical permission according to the policies and principles established by the Animal Welfare Act, the National Institutes of Health Guide for Care and Use of Laboratory Animals, and the National Animal Welfare Guidelines and were approved by the local legal representative animal rights protection authorities (Landesamt für Gesundheit und Soziales Berlin: G0008/12; T0119/14; T0249/11).

3.1.2 Mouse housing

Mice were housed in small groups in the Charité animal facility (Forschungseinrichtung für experimentelle Medizin) on the Campus Virchow-Klinikum. They were kept under SPF or semi-sterile (area in the animal facility without an additional barrier and without filtered air supply for the mice cages) housing conditions, respectively. The temperature was controlled ($20 \pm 2\,^{\circ}C$), a 12 h light/dark circle was present and food and water were available ad libitum. For the *in vivo* analyses, mice of an age of 12 weeks were used. The peak bone mass and the material properties are almost achieved and reached at this age [108]. For mice kept under SPF conditions, they were imported into our animal facility at least 1 week before usage in order to allow the animals to acclimatize. Mice that were housed in the semi-sterile part of the animal facility were imported at least 4 weeks before the experiment started. The housing in the semi-sterile environment as well as the import of 4 weeks prior to use were chosen to allow a moderate activation of the adaptive immune system of the animals.

3.1.3 Surgery: Setting of an osteotomy

In order to analyze the fracture healing process in our animal model, mice were narcotised by the inhalation of the anaesthetic Isoflurane. Before starting the surgery, mice already received an intraperitoneal injection of the analgesic Buprenorphin (Temgesic) (0.03 mg/kg) and of the antibiotic Clindamycin (45 mg/kg). In addition, mice got an eye ointment for the duration of the surgery (Bepanthene). Before opening the skin by a lateral longitudinal cut (along an imaginary line from the knee to the hip), the operation area of the left femur was shaved and disinfected. After the skin was opened (Fig. 3.1 A), the femur was exposed by a blunt preparation of the surrounding muscles *Musculus vastus lateralis* and *Musculus biceps femoris* without creating an additional muscle injury and without injuring the *Nervicus ischiadicus* (peripheral nerve of the lower limbs) (Fig. 3.1 B). Before setting an osteotomy in the middle of the left femur, the external fixator was mounted on the lateral side of the bone for stabilization after surgery. Therefore, the first of the four pins was installed near the knee, already with the bar of the external fixator attached to the pin, so that the bar of the external fixator was in parallel to the bone (Fig. 3.1 C, D). The second pin was installed near the hip and pin 3 and 4 were placed in between pin 1 and 2 (Fig. 3.1 E). Subsequently, the osteotomy gap was created with a Gigli wire saw (size: 0.66 mm) between the two middle

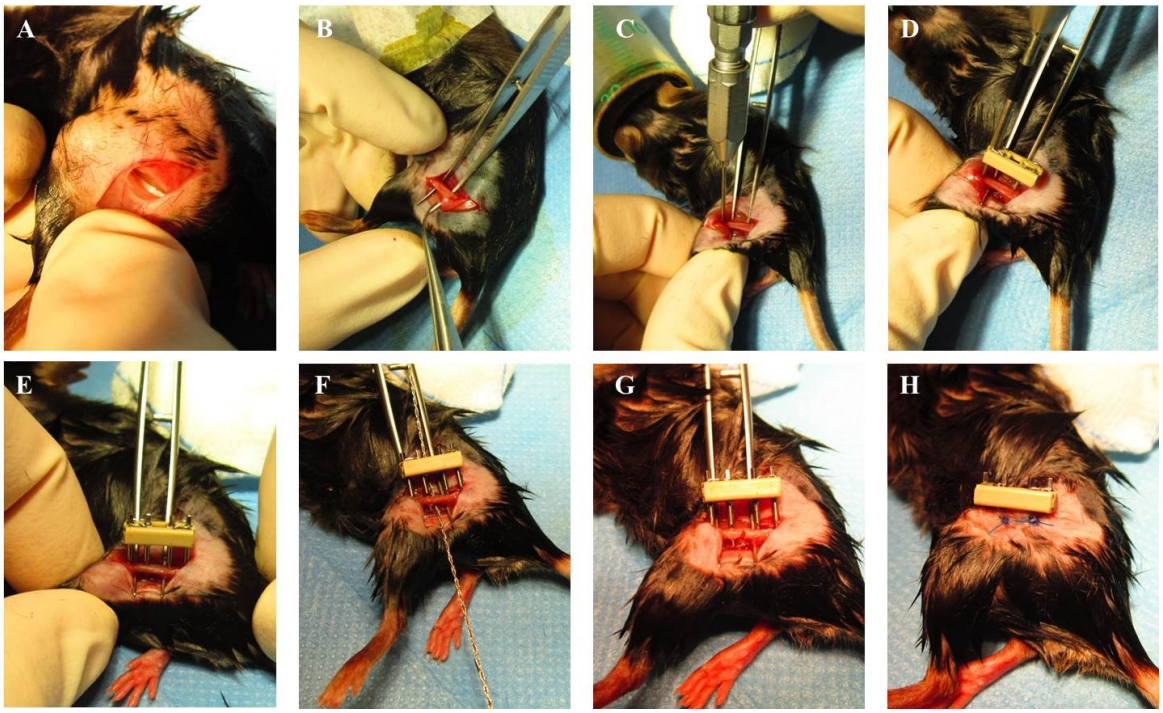

Figure 3.1: Illustration of the steps of the surgery in our mouse osteotomy model. Skin opening (A); Exposure of the left femur (B); Drilling the hole for the first pin (C); Insertion of the first pin (D); External fixator already fixed with four pins (E); Positioning of the Gigli wire saw (F); Osteotomy gap between the two middle pins (G); Sutured skin after osteotomy (H)

pins, resulting in a gap size of 0.7 mm (Fig. 3.1 F, G). Afterwards, the wound was sutured (Fig. 3.1 H), followed by the application of spray dressing. After surgery, mice were brought back into a cage and closely observed until they were fully mobile again. Tramadol hydrochloride was added to the drinking water (25 mg/l) as postoperative analgesia for 3 days post-surgery.

3.1.4 Euthanasia of mice

To euthanize the mice, a mixture of the muscle relaxant Ketamine (60 mg/kg) and the sedative Medetomidine (0.3 mg/kg) was intraperitoneally injected in order to induce deep narcosis. After confirming that the mice showed no reflex anymore (pedal withdrawal reflex), a cervical dislocation was done in order to ensure the death of the animal. For samples collected for flow cytometry, histology and μCT (Chap. 3.2.1), full blood was taken out of the heart prior to the cervical dislocation.

3.1.5 Experimental design

Table 3.1: Experimental design of the mice used, organized by the treatment, including the number of used animals, analyzed time points and the usage of the fractured bones

Group	Time points	Mice	Fractured femur for histology	Fractured femur for µCT
WT	1 d	n= 6	yes	no
	2 d	n= 6	yes	no
	3 d	n= 6	yes	no
	7 d	n= 6	yes	no
	14 d	n= 6	yes	no
	21 d	n= 6	yes	yes
SPF T_{Reg} +	21 d	n= 6	no	yes
semi-sterile T_{Reg} +	21 d	n= 8	yes	yes
CD25-	21 d	n= 6	yes	yes
POC T_{Reg} +	21 d	n= 7	no	yes

3.2 Sample collection

3.2.1 Sample collection for flow cytometry, histology and µCT

Mice were euthanized by an intraperitoneal injection of a mixture of Ketamine and Medetomidine (Chap. 3.1.4). As soon as the mice showed no reflex anymore (pedal withdrawal reflex of the hind paw), blood was drawn directly out of the heart and kept in an ethylenediaminetetraacetic acid (EDTA) coated blood collection tube. Afterwards, a cervical dislocation of the mice was performed to ensure the death of the animal. The skin of the abdomen was opened by a longitudinal cut with a scalpel and the spleen was taken out. Around three quarters of the spleen were immediately put into a falcon tube filled with phosphate buffered saline (PBS) and placed on ice (flow cytometry). The fourth quarter was put into a falcon filled with a freshly prepared solution of 4 % paraformaldehyde (PFA) (histology) (also placed on ice). Subsequently, the fractured left femur still stabilized by the external fixator was taken out of the mouse, the most part of the surrounding muscles was carefully removed and the bone was put into the falcon filled with 4 % PFA. The complete contralateral leg and both humeri were taken for bone marrow analysis by flow cytometry (in PBS placed on ice).

3.2.2 Sample collection for the isolation of regulatory T cells

Regulatory T cells were isolated out of the spleen and the following lymph nodes from C57BL/6N mice: inguinal nodes, axillary nodes, brachial nodes and mesenteric nodes. After confirming that the narcotised mouse did not show any reflex anymore (pedal withdrawal reflex), a cervical dislocation was performed to ensure the death of the animal. The skin was removed to enable access to the underlying lymph nodes. Inguinal, axillary and brachial lymph nodes were carefully detached from the mice with the help of fine forceps and put into a falcon tube filled with PBS (placed on ice). Afterwards, the abdominal muscles including the peritoneum were opened and the spleen was taken out and put in PBS. Finally, the

mesenteric lymph nodes were removed from the mouse and put into the same falcon with the other lymph nodes.

3.3 Flow cytometry

The flow cytometry method allows the measurement of the biological properties (e. g. size, granulation, expression of surface and intracellular markers) of a single cell in suspension. The basic principle is the highly specific antigen-antibody interaction that is visualized by fluorescence labeled antibodies. The measurement of the biological properties is realized via a packed laser beam. Every single cell is passing the laser beam due to their organization like on a bead chain and is thereby analyzed [109].

3.3.1 Sample preparation

Prior to staining for flow cytometry analyses, a single cell suspension of the organs was prepared. For the evaluation of the systemic cell distribution in the osteotomized mice post-osteotomy, the following tissues were analyzed: spleen, bone marrow (tibia and femur of the contralateral leg, both humeri) and full blood.
Spleen: The spleen was cut into small pieces with a scalpel und was carefully pressed through a cell strainer (size: 40 µm) with the plunger of a syringe. The isolated cells were collected in a culture dish. The cell strainer was washed with PBS for several times in order to obtain all of the isolated splenocytes. Bone marrow: The ends of the bones were carefully cut off to open the medullary canal. Further, the bone marrow was flushed out with a syringe. Afterwards, the bone marrow was carefully pressed through a cell strainer (size: 40 µm) with the plunger of a syringe. The isolated cells were collected in a culture dish. The cell strainer was washed with PBS for several times in order to obtain all of the isolated bone marrow cells.
The full blood was centrifuged (10 min at 500x g) and the obtained supernatant was removed. The cellular part of the full blood was resuspended in erythrocyte lysis (EL) buffer and incubated for 10 min at room temperature (RT). For the bone marrow and the spleen, the prepared single cell suspension was centrifuged for 10 min at 500x g at 4 °C. The supernatant was removed and the cell pellet was resuspend in EL buffer and incubated for 8 min at RT. Afterwards, all tissue samples were centrifuged (10 min at 500x g at 4 °C) and washed twice with PBS. The following preparation and centrifugation steps were done on ice and with the already mentioned parameters, besides otherwise indicated. After the second washing step, the cell number from the prepared organs was determined by using a hemocytometer. The cell suspensions of the organs were resuspend in PBS in the following concentration: $1x10^6$ cells in 100 µl.

3.3.2 Antibody staining for flow cytometry

From each organ, 2 different antibody panels were stained (Tab. 3.2). For panel 1 which only included surface staining antibodies, 100 µl of the cell suspension was transferred to a fluorescence-activated cell sorting (FACS) tube. Due to the fact that panel 2 included an intranuclear staining and thus more washing steps, 200 µl of the cell suspension was transferred to a second FACS tube. For both panels, a negative control was taken composed of a mixture of spleen and bone marrow cells.

Table 3.2: Overview of the antibodies used including their specificity, clone and dilution for the flow cytometry analysis of panel 1 and 2.

Antibody	Dilution
Panel 1	
α-mouse CCR7 Biotin	1:100
α-mouse CD3ε PerCP	1:20
α-mouse CD4 AF700	1:100
α-mouse CD8a eF450	1:100
α-mouse CD25 APC-Cy7	1:25
α-mouse CD44 PE-Cy7	1:200
α-mouse CD62L APC	1:200
α-mouse CD127 PE-Cy7	1:100
α-mouse NK-1.1 FITC	1:50
α-mouse TCRβ chain PE	1:50
Streptavidin PE-Texas Red	1:50
LIVE/DEAD Fixable Aqua Dead Cell Stain Kit (405 nm)	1:50
Panel 2	
α-mouse CD3ε PerCP	1:20
α-mouse CD4 AF700	1:100
α-mouse CD8a eF450	1:100
α-mouse CD16/ CD32 Purified	1:100
α-mouse CD25 APC	1:100
α-mouse CD44 APC-Cy7	1:100
α-mouse CD127 PE-Cy7	1:50
α-mouse/ human Helios PE	1:50
α-mouse/ rat FOXP3 FITC	1:50
LIVE/DEAD Fixable Aqua Dead Cell Stain Kit (405 nm)	1:50

First, the dead cells were stained by the application of a LIVE/DEAD dye for 30 min on ice. After the washing step (FACS tube was filled up with PBS, centrifuged for 10 min at 500x g at 4 °C, the supernatant was decanted), all further washing and staining steps were performed in a PBS based buffer: 1x PBS with 1 % BSA and 0.1 % sodium azide (PBS/ BSA). For panel 1, cells were washed, the pellet resuspended and stained for 15 min at 37 °C for the surface marker CCR7 (biotin coupled α-mouse CCR7). Cells were washed in PBS/ BSA, resuspended and a mixture of all other surface marker antibodies was applied to the cell suspension and incubated for 20 min on ice: α-mouse CD3ε, α-mouse CD4, α-mouse CD8, α-mouse CD25, α-mouse CD62L, α-mouse CD127/ α-mouse CD44, α-mouse NK1.1, α-mouse TCRαβ and streptavidin (Tab. 3.2). After the following washing step in PBS/ BSA, the cell pellet was resuspended in a 2 % formaldehyde solution and fixed for 20 min at RT in the dark. Finally, the cells were washed in PBS/ BSA, resuspended and measured with the flow cytometer LSR II from Beckman Coulter.
For panel 2, after washing off the LIVE/DEAD dye, the cells were resuspended. Immediately afterwards, a mixture of all surface marker antibodies was added to the cells and incubated for 20 min on ice: α-mouse CD3ε, α-mouse CD4, α-mouse CD8, α-mouse CD25, α-mouse CD44 and α-mouse CD127 (Tab. 3.2). Cells were washed in PBS/ BSA, resuspended and incubated with 250 µl of a fixation/permeabilization buffer for 1 h on ice. Cells were washed twice with 2 ml each of a permeabilization buffer, resuspended, and stained for 30 min

on ice with α-Foxp3 and α-Helios. Cells were washed in PBS/BSA, resuspended and filtered through a CellTrics filter, in order to get rid of deoxyribonucleic acid (DNA) protein complexes formed due to the permeabilization process. After filtration, cells were washed again in PBS/BSA, resuspended and measured with the flow cytometer LSR II.

3.3.3 Performed quality controls for flow cytometry

For flow cytometry analysis, different indispensable quality controls were performed prior to the experimental measurement. For the used antibodies, the correct dilution was determined. Therefore, different dilutions of each antibody were prepared, stained on murine cells and analyzed with the flow cytometer LSR II. The optimal dilution was defined as the best signal to background staining. In addition, isotype controls were tested in order to exclude an unspecific binding of their immunoglobulin backbone and thus to ensure the specific binding of the used antibodies. Before the flow cytometry analysis of the experimental samples could be performed, the used antibody panels (Tab. 3.2) had to be compensated at the flow cytometer. The panels comprised multiple antibodies coupled with different fluorochromes. Each fluorochrome is characterized by a specific excitation and emission wavelength. The emission signal of each fluorochrome will be measured in a different filter of the flow cytometer. However, the emission signals often do not emit light in only one special wavelength but in a spectrum of wavelength. This spectrum of emission light can also be detected in the filter of another fluorochrome. The false positive signal has to be subtracted from the true emission light of the respective fluorochrome. This is done via a compensation measurement. In parallel to the compensation analysis, a single staining of every used antibody was also done as well as fluorescence minus one (FMO) staining (Fig. 3.2, 3.3). Both, the single and FMO-stainings are necessary especially for the data analysis following the flow cytometry measurement (Chap. 3.3.4). In addition, a FC block (α-CD16/CD32) was used for the stainings in order to exclude an unspecific binding of the used antibodies.

3.3.4 Flow cytometry data analysis with the analyzing software FlowJo

The analysis of the measured data was realized with the FlowJo analyzing software. The measured data were visualized by the software via dot plot diagrams or histograms. First, the analyzed cell suspension was depicted in a dot plot diagram, in dependence of the following cellular properties: the size and the granulation. This type of dot plot is known as the forward scatter (FSC) (size) vs. sideward scatter (SSC) (granulation) (Fig. 3.2, 3.3, upper row, left dot plot). After gating the lymphocyte cell population, identified by their size and granularity within the FCS/SSC dot plot , singlets were gated to get rid of doublets and triplets which falsify the obtained data. By using a live dead fluorescent dye (LIVE/DEAD, LD), dead cells were then excluded from further analysis. Data of populations of interest were either taken as the percentage of the prior gated cell population (frequency of parent) or calculated on the basis of CD3+TCRαβ+ or CD3+CD4+ or CD3+CD8+ T cell populations. An exemplary gating of panel 1 and panel 2 with FlowJo and the corresponding FMO stainings are depicted in figure 3.2 and 3.3.

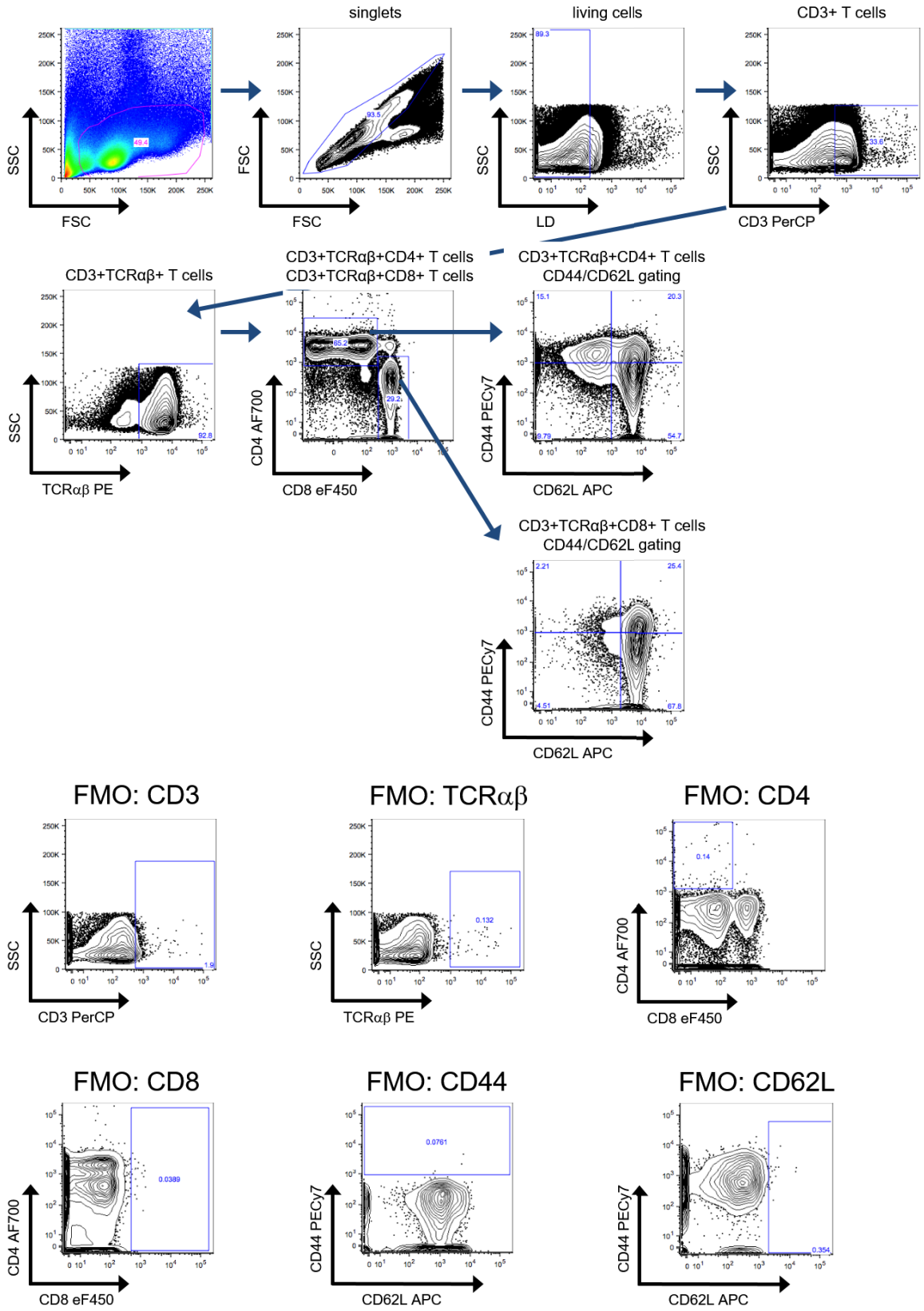

Figure 3.2: Representative flow cytometry scheme of panel 1. Illustrated is the gating strategy from the lymphocyte population, over the singlets, living cells, CD3+ T cells, CD3+TCRαβ+ T cells, CD3+TCRαβ+CD4+ and CD3+TCRαβ+CD8+ T cells and the respective CD44/CD62L T cell subsets; on the bottom, the corresponding gates of the fluorescence minus one (FMO) staining are presented.

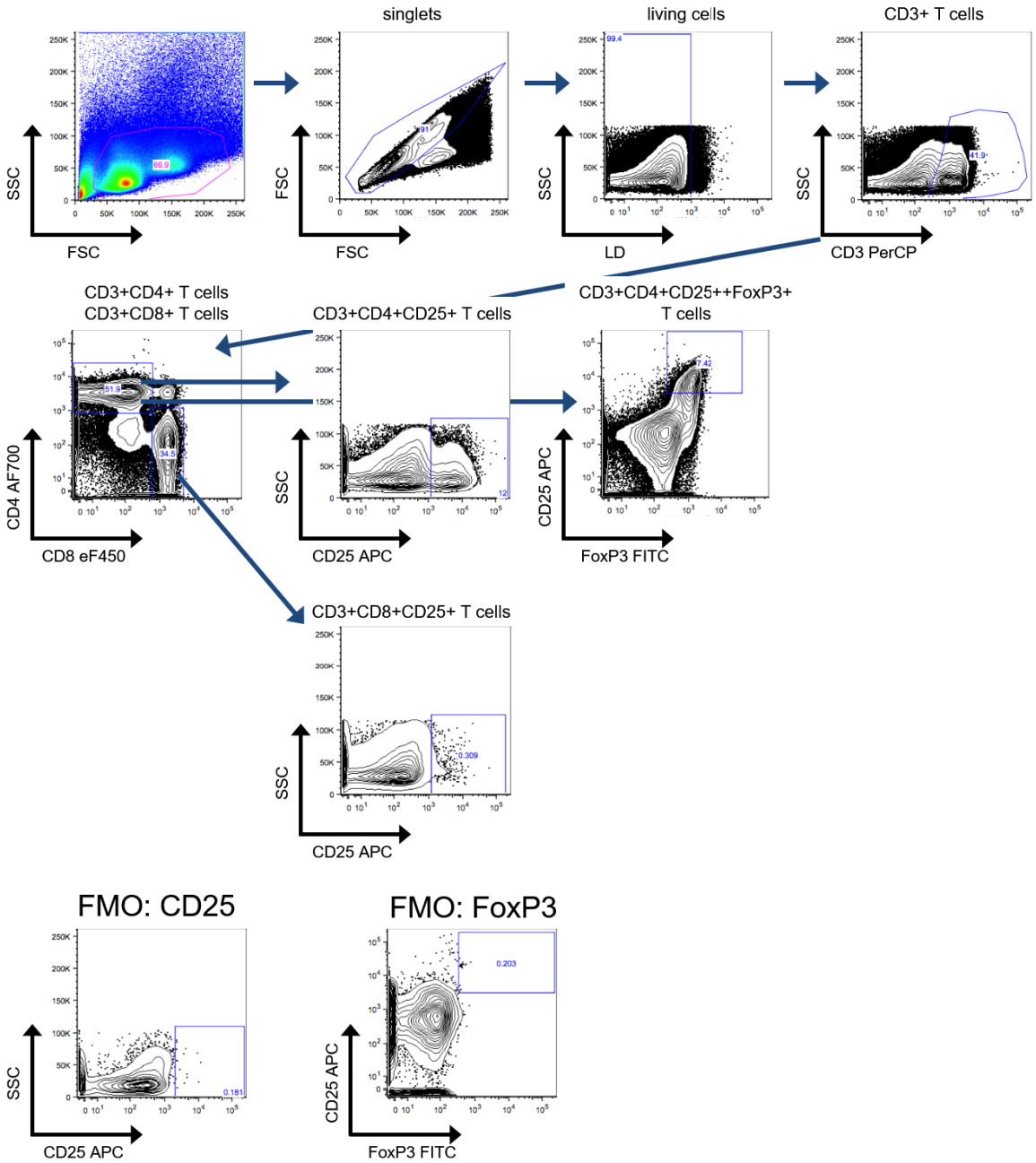

Figure 3.3: Representative flow cytometry scheme of panel 2. Illustrated is the gating strategy from the lymphocyte population, over the singlets, living cells, CD3+ T cells, CD3+CD4+ and CD3+CD8+ T cells, the respective CD25+ T cell subsets as well as CD25++FOXP3+ T cells; on the bottom, the corresponding gates of the fluorescence minus one (FMO) staining are presented (FMO: CD3, FMO: CD4 and FMO: CD8 are already presented in figure 3.2).

3.4 Therapeutic intervention in our mouse osteotomy model

3.4.1 Adoptive transfer of regulatory T cells

3.4.1.1 Magnetic activated cell sorting technology

Magnetic activated cell sorting (MACS) is a powerful tool for a microbead-based separation of specific cell populations from a cell suspension [110]. The microbeads are superparamagnetic particles of a size of 50 nm that are bound to antibodies specific for an antigen on the cell surface. For the separation procedure, the labeled cell suspension is placed in a high-gradient magnetic-field in a column filled with ferromagnetic stainless steel wool. Positive labeled cells are kept in the column as along as it stays in the magnetic field. The unlabeled cells (the negative fraction) run through the column and remain untouched. To separate the positive fraction from the column, the column just has to be taken out of the high-gradient magnetic-field and the positive fraction can be further collected in a collection tube. Therefore, the MACS technology enables the collection of the unlabeled and labeled cells in a relative fast and harmless procedure to receive a pure cell substrate.

3.4.1.2 Mouse housing for the therapeutic intervention approach

For the enrichment of T_{Reg} prior to surgery, two approaches were used: 1) T_{Reg} isolated from SPF housed donor mice were adoptively transferred into SPF housed recipient animals; 2) T_{Reg} isolated from semi-sterile housed mice were transferred into semi-sterile housed recipient mice. With the first approach (SPF housed conditions), the therapeutic potential of T_{Reg} was tested. In the second approach, a more experienced immune system in the experimental mice was included in the experimental design, bringing our mouse model closer to the patient situation. By this approach, the validity of the therapeutic potential of T_{Reg} was analyzed in a clinically more relevant model.

3.4.1.3 Sample collection

Murine T_{Reg} were isolated from spleen and the following lymph nodes: inguinal nodes, axillary nodes, brachial nodes and mesenteric nodes. The used buffer for the preparation of the single cell suspension and the following MACS (Chap. 3.4.1.4) separation was 1x PBS including 0.5 % bovine serum albumin (BSA) and 2 mM EDTA. This MACS buffer was sterile filtered before usage and kept at 4 °C. All the separation steps were done under a clean bench and on ice or in the fridge at 4 °C, besides otherwise indicated. To get a single cell suspension, the spleen was cut into small pieces and was carefully pressed through a cell strainer (size: 100 µm) with the plunger of a syringe. Afterwards, the erythrocytes were lysed by ammonium-chloride-potassium (ACK) lysis buffer for 4 min at RT. The lymph nodes were directly carefully pressed through a cell strainer (100 µm). After the lysis of the erythrocytes, the cells from the lymph nodes and the remaining splenocytes were combined and the cell number was determined with a hemocytometer.

3.4.1.4 Regulatory T cell isolation

For the isolation of murine T_{Reg}, a combined separation procedure of a first negative depletion of all CD4+ T cells and a following positive selection by an α-CD25 labeling, was used. The isolation itself was done accordingly to the protocol of the CD4+CD25+ Regulatory T Cell Isolation Kit. After determination of the total amount of isolated cells,

cells were resuspended in a concentration of 1x10^7 cells in 40 µl MACS buffer. In a first step, all non-CD4+ cells were marked by a biotin-labeled antibody mix for 10 min at 4 °C. Further, bead-conjugated anti-biotin antibodies and an α-CD25 PE-labeled antibody were added to the cell suspension for 15 min at 4 °C. After a washing and centrifugation step (8 min at 1 500 rpm at 4 °C), cells were resuspended in MACS buffer to a final concentration of up to 1.25x10^8 cells/500 µl. An LD MACS column was equilibrated by rinsing it with 2 ml MACS buffer. Afterwards, the column was placed in the magnetic field of the separator. The labeled cell suspension was added to the column and the negative fraction (CD4+ T cells) was collected in a falcon tube. The column was washed twice with 1 ml MACS buffer. In order to elute the non-CD4+ T cells too, the column was removed from the magnetic field, 1 ml MACS buffer was immediately added to the column and the cells were flushed out by pushing a plunger into the column. The CD4+ fraction was centrifuged (8 min at 1 500 rpm at 4 °C) and resuspended in 90 µl MACS buffer for 1x10^7 cells. In addition, a microbead-conjugated α-PE antibody was added to the cell suspension for 15 min at 4 °C. Cells were washed, centrifuged (8 min at 1 500 rpm at 4 °C) and resuspended in 500 µl MACS buffer for up to 1x10^8 cells. An MS MACS column was equilibrated by rinsing it with 500 µl MACS buffer. After equilibration, the column was placed in the magnetic field of the separator and the cell suspension was added to the column. The negative fraction (CD4+CD25- T cells) passed through the column and was collected in a falcon tube. The positive labeled cells were retained in the column and were washed three times with 500 µl MACS buffer. Afterwards, the column was removed from the magnetic field, 1 ml of MACS buffer was added to it and the cells were flushed out by pushing the plunger into the column. The cell number of the isolated CD4+CD25+ T_{Reg} fraction was counted in a hemocytometer.

3.4.1.5 Flow cytometry for the evaluation of the purity of MACS isolated regulatory T cells

In order to confirm the successful purification of T_{Reg}, a flow cytometry analysis was done following the MACS isolation. Therefore, two samples of the cell suspension prior to the MACS separation were taken for a negative and positive control, respectively, of the original cell population. In addition, samples from the CD4- fraction, as well as from the negative fraction of the second purification step (CD4+CD25- T cells) and from the isolated T_{Reg} fraction were taken. All 5 samples were washed with PBS and stained for 30 min on ice with a LIVE/DEAD staining dye. Afterwards, cells were washed, centrifuged (10 min at 500x g at 4 °C) and resuspended in PBS/BSA. A mixture of surface antibodies (Tab. 3.3) was added to the samples and incubated for 20 min on ice. After a following washing step, cells were resuspended and incubated with 250 µl of fixation/permeabilization buffer for 1 h on ice. Cells were washed twice with 2 ml each of a permeabilization buffer, resuspended, and stained for 30 min on ice with α-FoxP3. Following, cells were washed in PBS/BSA, resuspended and filtered through a CellTrics filter (30 µm). After filtration, cells were washed again in PBS/BSA, resuspended and measured with the flow cytometer LSR II.

3.4.1.6 Pre-activation of isolated regulatory T cells

Pre-activation of freshly isolated T_{Reg} was realized by an α-CD3/α-CD28 T cell receptor stimulation in addition with the supply of murine recombinant IL-2. Wells of a 96 well plate were pre-coated with α-CD3/α-CD28 antibodies (each 5 µg/ml), diluted in PBS. The pre-coating was done by an incubation of 200 µl of the antibody-PBS-solution per well for 3 h in the incubator (37 °C, 5 % CO_2) or overnight in the fridge at 4 °C. Subsequently, wells were

rinsed two times with PBS. 3x10^5 freshly isolated T_{Reg} were transferred to the pre-coated wells in a volume of 200 µl. The used medium was RPMI 1640 including 10 % FBS superior, 50 µM β-Mercaptoethanol and 1 % Penicillin/Streptomycin. Two different concentrations of IL-2 were tested for the pre-activation: 50 ng/ml and 360 ng/ml. Pre-activated T_{Reg} were harvested after 12 h, 24 h, 48 h and 72 h. The pre-activation was analyzed via flow cytometry using the following antibodies: α-mouse CD3ε, α-mouse CD4, α-mouse CD25, α-mouse FoxP3 and α-mouse CD69. In addition, a LIVE/DEAD staining was included in order to exclude the dead cells from the analysis. The marker CD69 was used to evaluate the activation status of the T_{Reg}. An activation of T_{Reg} corresponds to an upregulation of the expression of CD69. Flow cytometry analyses were done at the moment of setting up the pre-activation culture (prior to pre-activation) and at the corresponding time points of the harvest. The staining for flow cytometry was done equivalent to chapter 3.4.1.5.

3.4.1.7 Regulatory T cell suppression assay

In order to analyze the suppressive capacity of MACS separated murine T_{Reg} and thereby their functionality, a T_{Reg} suppression assay was performed. Therefore, isolated T_{Reg} were *in vitro* co-cultured in different ratios with CD4+CD25- responder T cells (T_{Resp}) [111], adapted from [112]. The basic principle of this suppression assay is to evaluate the proliferation of the T_{Resp}. The proliferation should be suppressed dependent on the amount of co-cultured T_{Reg} if T_{Reg} are functional (the more T_{Reg}, the more suppression).
T_{Resp} were isolated by MACS as described before (Chap. 3.4.1.4). After determining the isolated cell number using a hemocytometer, 1x10^7 T_{Resp} were stained with a cell proliferation dye eFluor 450 as described in the protocol. In short: Isolated T_{Resp} were washed twice with PBS (centrifugation step: 8 min at 1 500 rpm at RT) to get rid of the serum of the MACS buffer. Afterwards, cells were resuspended in pre-warmed PBS to a concentration double as high as the final concentration. For a final concentration of 10x10^6 cells/ml, 10x10^6 T_{Resp} were resuspended in 500 µl of pre-warmed PBS (2x cell suspension). 500 µl of a 10 µM eFluor 450 Cell Proliferation Dye solution was added to the 2x cell suspension while vortexing. Stained cells were incubated for 20 min in the dark at RT. The staining was stopped by adding 10 ml of ice cold complete cell culture medium (RPMI 1640 including 10 % FBS superior, 50 µM β-Mercaptoethanol and 1 % Penicillin/Streptomycin). After 5 min incubation on ice, cells were washed three times with pre-warmed complete cell culture media. The cell number was determined by hemocytometer. For the setup of the suppression assay, 0.75x10^5 labeled T_{Resp} were co-cultured with the following amounts of freshly isolated or pre-activated T_{Reg}: 1.5x10^5 (1 to 2; T_{Resp} to T_{Reg}) and 0.15x10^5 (1 to 0.2), respectively. As internal controls, labeled T_{Resp} were also cultured either alone or in co-culture with unlabeled T_{Resp}. In order to stimulate the proliferation of the T_{Resp}, the co-culture was realized in flat bottom 96 well plates that were pre-coated with α-CD3e (5 µg/ml) and α-CD28 (5 µg/ml) antibodies diluted in PBS. As negative controls, labeled and unlabeled T_{Resp} were also cultured in wells without antibody coating. From every co-culture sample, two wells of a 96-well plate were filled. The setup for the suppression assay is exemplary shown in figure 3.4. The suppression assay was done in complete cell culture media as described above. The suppression assay was examined every day by a microscopic control and the assay was harvested after 2–3 days, dependent on the velocity of the proliferation of the T_{Resp}. The percentage of suppression was calculated based on the proliferation of labeled T_{Resp} that were cultured alone. The proliferation of labeled T_{Resp} was set to 100 and the proliferation of the co-culture setups was calculated relative to the T_{Resp}. The percentage of the suppression of proliferation was further calculated as follows: 100 minus the relative value of the proliferation.

stimulation	α-CD3/α-CD28	α-CD3/α-CD28	α-CD3/α-CD28	α-CD3/α-CD28	-	-
co-culture setup	T_{Resp} to T_{Reg} 1 to 2	T_{Resp} to T_{Reg} 1 to 0.2	T_{Resp} eF450	T_{Resp} eF450 to T_{Resp} 1 to 1	T_{Resp} eF450	T_{Resp}
applied cell number; cultured as duplicates	$0{,}75x10^5$ to $1{,}5x10^5$	$0{,}75x10^5$ to $0{,}15x10^5$	$0{,}75x10^5$	$0{,}75x10^5$ to $0{,}75x10^5$	$0{,}75x10^5$	$0{,}75x10^5$
	$0{,}75x10^5$ to $1{,}5x10^5$	$0{,}75x10^5$ to $0{,}15x10^5$	$0{,}75x10^5$	$0{,}75x10^5$ to $0{,}75x10^5$	$0{,}75x10^5$	$0{,}75x10^5$

Figure 3.4: Overview of the pipette scheme and applied cell number of cell proliferation dye labeled T_{Resp} (T_{Resp} eF450), freshly isolated or pre-activated T_{Reg} and unlabeled T_{Resp} for the T_{Reg} suppression assay; α-CD3/α-CD28 indicates that the wells were stimulated in this column.

3.4.1.8 Flow cytometry for the evaluation of the regulatory T cell suppression assay

The suppressive capacity of freshly isolated murine T_{Reg} was evaluated by flow cytometry. From every co-culture sample, a small aliquot was taken at the moment of co-culture setup (t= 0) for flow cytometry analysis in order to confirm the labeling of the T_{Resp} and the right ratio between T_{Reg} and T_{Resp}. The samples prior to the suppression assay and the harvested cells after the end of the assay were first washed with PBS and stained for 30 min with LIVE/DEAD (Tab. 3.3). After washing with PBS/BSA (Chap. 3.3.2), cells were stained for the surface marker α-CD3, α-CD4 and α-CD25 for 20 min on ice (antibody were diluted in PBS/BSA). Cells were washed in PBS/BSA, resuspended and fixed for 20 min (in the dark, at RT) with a 2 % formaldehyde solution. After a final washing step with PBS/BSA, cells were resuspended and analyzed with the LSR II.

3.4.1.9 Adoptive transfer of regulatory T cells

For the adoptive transfer of T_{Reg}, isolated cells were washed in a sterile solution of 0.9 % sodium chloride following the MACS separation. Washed cells were resuspended in 0.9 % sodium chloride and filled in a volume of 150–200 µl in a syringe. After confirming the purity of the isolated T_{Reg} via flow cytometry, 5–8x10^5 T_{Reg} were directly adoptively transferred into the tail vein of recipient mice. Furthermore, the mice directly underwent the osteotomy. During the time needed to confirm the purity, isolated T_{Reg} were kept at 4°C.

3.4.2 Depletion of CD25+ T cells

3.4.2.1 Depletion of CD25+ T cells - Procedure

CD25+ T cells were depleted prior to surgery. For the depletion, an α-CD25 antibody was applied to the animals by four consecutive intraperitoneal injections of 200 µg diluted in 0.9 % sodium chloride, starting three days prior to surgery. The depletion of the CD25+ T cells was confirmed via flow cytometry at the day of surgery. The healing outcome of CD25+ depleted animals was evaluated after 21 d by µCT and histological analysis.

3.4.2.2 Flow cytometry analysis to confirm CD25+ T cell depletion

In order to confirm the depletion of CD25+ T cells prior to surgery, flow cytometry analysis were done at the day of surgery. 1–2 drops of peripheral blood were taken from the *Vena facialis* (in the cheek of the animal) of the depleted animals and directly lysed in erythrocytes lysis buffer for 5 min at RT. After washing with PBS/BSA (centrifugation: 10 min at 500x g at 4 °C), the samples were resuspended in an in PBS/BSA diluted antibody mix (α-CD3, α-CD4 and α-CD25 (Tab. 3.3)) and incubated for 20 min on ice. Afterwards, the samples were washed and analyzed with the LSR II as described previously.

Table 3.3: Overview of the antibodies used including their specificity, clone and dilution for the flow cytometry analysis of the MACS check, the T_{Reg} suppression assay and the confirmation of the CD25+ T cell depletion.

Antibody	Dilution
MACS check	
α-mouse CD3εPerCP	1:20
α-mouse CD4 AF700	1:400
α-mouse CD8a eF450	1:100
α-mouse CD25 APC	1:100
α-mouse/ rat FOXP3 FITC	1:50
LIVE/DEAD Fixable Aqua Dead Cell Stain Kit (405 nm)	1:50
T_{Reg} suppression assay	
α-mouse CD3ε PerCP	1:20
α-mouse CD4 AF700	1:400
α-mouse CD8a eF450	1:100
α-mouse CD25 APC	1:100
LIVE/DEAD Fixable Aqua Dead Cell Stain Kit (405 nm)	1:50
CD25+ T cell depletion	
α-mouse CD3εPerCP	1:20
α-mouse CD4 AF700	1:400
α-mouse CD25 APC	1:100

3.5 Histology

The term histology derives from the Greek words *histos* and *logia* which means "tissue" and "science", respectively. It studies the microscopic anatomy of cells and tissues of plants and animals.
In the framework of my PhD thesis, histological methods were used in order to analyze the healing outcome and distribution of different tissue types within the healing bone. The immunohistochemical staining methods were used to evaluate the spatial and temporal localization of selected immune cell types in the healing mouse femur.

3.5.1 Collection of bone samples

Fractured murine bones were taken out of the animal at the indicated time points (Chap. 3.1.5). They were directly placed in 4 % PFA fixation solution for 4 h at 4 °C. Afterwards, the 4 % PFA was removed and replaced by a freshly prepared 10 % sucrose solution and kept for 24 h at 4 °C. The sucrose solution was exchanged by a 20 % and 30 % one, respectively, each after 24 h incubation at 4 °C. The bones from the 21 d animals were now prepared for the micro–computed tomography (μCT) analysis (Chap. 3.7). Subsequently, all bones were cryo-embedded (Chap. 3.5.2).

3.5.2 Embedding of bone samples

Cryo-embedding is a useful method in order to keep the tissue architecture intact during the embedding process. Another big advantage for the histological analysis of cryo-embedded bone tissue is that it does not have to be decalcified in order to be cut. A decalcification procedure can alter the tissue structure and thereby can cause a loss of biological information of the treated tissue. For the process of tissue cryo-embedding and further cutting, the method modified and optimized by Prof. Tadafumi Kawamoto (Section-Lab Co. Ltd., Hiroshima, Japan) was used [113, 114]. The basic principle of this method is to freeze the calcified fixed bone tissue sample in ice cold n-hexane and to further cut it in a cryotome with the help of a special adhesive film on the cutting plane (Chap. 3.5.3).
For the embedding procedure, a dewar vessel was half filled with acetone and dry ice. A beaker filled with n-hexane was placed into the acetone dry ice mixture and was allowed to cool down for 10-15 min. The bone sample was placed in a metallic embedding form (Fig. 3.5 A) and embedding media (SCEM media, Section-Lab Co. Ltd., Hiroshima, Japan) was filled into the form. For the bone samples in which the external fixator was still in (time points 1–14 d), the embedding media was just filled into the embedding form till the lower part of the bone was covered with media. Now, the embedding form with the bone sample in it was placed into n-hexane, till the media got frozen. The form was taken out off the n-hexane and the external fixator was swiftly but carefully removed from the bone with a respective instrument. The embedding form was filled up with embedding media till the bone was completely covered, was put back into n-hexane and completely frozen (Fig. 3.5 C). For the samples that went into μCT analysis before and which therefore had no external fixator anymore, the embedding form with the bone samples was directly completely filled with embedding media (Fig. 3.5 B) and placed into n-hexane till it was completely frozen (Fig. 3.5 C). The bone sample was placed in the embedding form having the pin holes perpendicular aligned to the cutting plane (Chap. 3.5.3). Afterwards, the frozen sample block was removed from the embedding form and stored at -80 °C till further use.

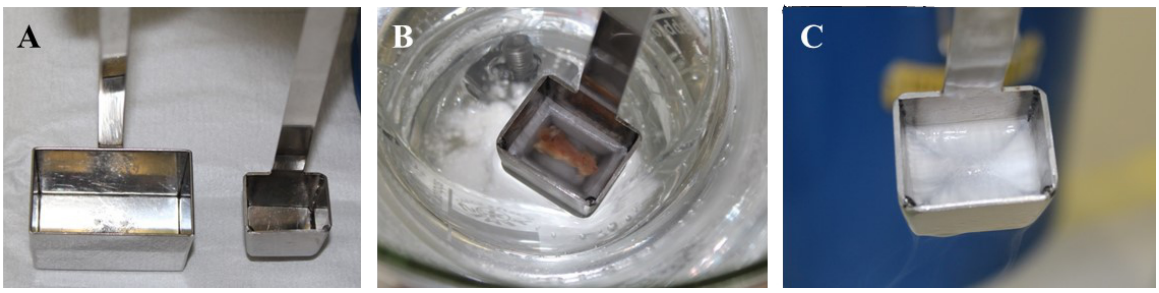

Figure 3.5: Illustration of the embedding procedure of murine femora by cryo-embedding. Metallic embedding form of different sizes (A); Embedding form, filled with embedding media (SCEM) and murine femur, placed into a beaker filled with n-hexane; the embedding media is already frozen at the edges of the embedding form (B); Cryo-embedded bone sample (frozen cryo tissue block) (C)

3.5.3 Cutting of bone samples

Embedded and frozen bone samples were cut in a cryotome (LEICA CM3050S). Before starting the cutting procedure, the frozen bone samples and the knife were placed into the cryotome in order to allow them to acclimatize to the temperature of the cryotome (around -23 °C). The frozen bone was glued on a pre-cold sample holder with embedding media (Tissue Tek). The sample holder was installed in the cryotome. The knife was carefully placed into the knife holder of the cryotome. After trimming the sample block till the bone became visible, the plane of the cut surface was adjusted to be planar so that the whole bone was cut along the longitudinal axis. As soon as the whole medullary canal was opened, sections of 7 µm thickness were taken. In order to enable the cutting of the calcified bone, a piece of cryofilm was glued onto the surface of the bone and the section was taken. From each bone, serial sections were taken in order to enable histological and immunohistological stainings (Chap. 3.5.4; 3.6) on consecutive slices. The cryofilm with the bone section was fixed with adhesive tape on an object slide. Object slides were stored at -80 °C till further use.

3.5.4 Histological staining: Movat Pentachrome

Movat Pentachrome is a histological staining method for bony tissue that allows the differentiation of the following tissue types due to the different staining solutions used: calcified bone/collagen and mineralized cartilage (Saffron du gatinais; yellow), hyaline cartilage (Alcian blue; green-blue), connective tissue (Alcian blue; blue-grey), cytoplasm (Brilliant crocein acid fuchsine; reddish) and cell nuclei (Iron hematoxylin (after Weigert); blue-black) [115]. The surrounding muscles are colored in reddish (Brilliant crocein acid fuchsine). Movat Pentachrome gives a good overview about the tissues presented within the bone and especially within the fracture area and about their distribution. The staining protocol including all the solutions and incubation times is presented in table 3.4.

Table 3.4: Staining protocol of the histological Movat Pentachrome staining.

Step	Incubation time
Thawing of the frozen sections	1 h at RT
Rehydration of the sections in 1x PBS	20 min
3 % Acetic acid	3 min
Alcian blue (1 % solution)in 3 % acetic acid (pH 2.5)	30 min
3 % Acetic acid	rinsing
Aqua dest.	rinsing
Ethyl alcohol	1h
Tap water	10 min
Iron hematoxylin (after Weigert)	10 min
Tap water	10 min
Brilliant crocein acid fuchsine	15 min
0.5 % Acetic acid	rinsing
5 % Phosphotungstic acid	20 min
0.5 % Acetic acid	1 min
96 % Alcohol	3x 2 min
Saffron du gâtinais	1 h
96 % Alcohol	3x 2 min
Xylol	2x 5 min

3.5.5 Histomorphometric analysis of the Movat Pentachrome staining

Based on the Movat Pentachrome staining, histomorphometrical analyses were done in order to elucidate the proportional distribution of the different tissue types within a defined region of interest (ROI) including the fracture gap. The ROI was defined as twice the size of the osteotomy gap, going from the center of the fracture area 0.7 mm to the left and to the right side (ROI= 1.4 mm). In the image processing program ImageJ, a MACRO tool especially written for these animals was used in order to determine the following parameter and tissue types: total callus area, cortical bone, new mineralized bone, cartilage, connective tissue and bone marrow. In figure 3.6, a scheme of the histomorphometrical evaluation of the MACRO is shown, representing the ROI as well as the different tissue types, indicated by the different colors (cortical bone = light yellow, new mineralized bone = yellow, bone marrow = violet and void area = white). The MACRO itself worked with a taken picture of the Movat Pentochrome stained bone section. The picture was taken with a light microscope in a 2.5x magnification and the program Axiovision. In order to ensure a correct identification and determination of the different tissue types, a microscopic view of the respective stained bone slice was done by me in parallel to the MACRO evaluation. The proportion of the tissues of interest (cortical bone, new mineralized bone, cartilage, connective tissue and bone marrow) were calculated as percentages based on the total callus area.

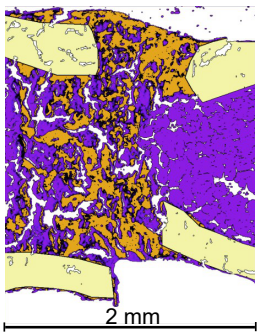

Figure 3.6: A scheme of the histomorphometrical MACRO evaluation is presented. Depicted is the region of interest, including the different analyzed tissue types, indicated by distinct colors: cortical bone = light yellow, new mineralized bone = yellow, bone marrow = violet and void area = white

3.6 Immunohistochemical staining with fluorescence-coupled antibodies

The basic principle of immunohistochemistry (IHC) stainings is the specific antigen-antibody interaction between a structure of interest in tissue sections and a specific antibody recognizing and binding to it. To visualize these interactions, the antibodies are either enzyme-, fluorescence- or ion-linked [116]. Albert Coons is one of the pioneers in IHC. After having published his first paper in the 1950s about the detection of cellular antigens by fluorescence labeled antibodies as a histochemical staining method, he quickly went on to further improve this technique [117, 118]. There are two different ways how the detection method of IHC stainings can be realized: it can be either direct (the used antibody is directly labeled with a reporter molecule) or indirect (the primary antibody is not directly labeled with a reporter molecule; therefore a labeled secondary antibody is needed for the signal visualization). The IHC staining used in this work were all done with fluorescence-coupled antibodies, either directly or indirectly. The advantage of using fluorescence-labeled antibodies is that multiple structures of interest can be simultaneously analyzed on one tissue section. This is based on the usage of antibodies labeled with different fluorochromes. In table 3.5, a general staining protocol is presented. Individual modifications are listed in the protocols for the specific stainings (Tab. 3.6). All steps were done at RT. From the blocking step on, all further steps were done in the dark (in a metallic section staining box). Finally, the stained tissue sections were embedded with mounting media (DAKO, Hamburg, Germany) and stored in the dark at 4°C till analysis.

Table 3.5: Basic protocol for the staining of bone sections with fluorescence-coupled antibodies (IHC).

Step	Incubation time
warming up the tissue section to RT	1 h
rehydration of the tissue section in 1x PBS	20 min
blocking of the tissue section	1 h
staining with the primary antibody	1 h
washing of the tissue section	3x 10 min
if necessary: staining with the secondary antibody	1 h
washing of the tissue section	3x 10 min
cell nuclei staining with DAPI	5 min
washing with 1x PBS	2x 15 min

3.6.1 Staining of macrophage subsets

The macrophage subsets M1 and M2 were stained using the following antibodies: CD68, CD80 and CD206. CD68 was used as a pan macrophage marker. Cells co-stained for CD68 and CD80 were identified as M1 macrophages, and a co-staining for CD68 and CD206 as M2 macrophages. After thawing and rehydration of the tissue sections as described in table 3.5, tissue sections were blocked for 1 h at RT with 1x tris-buffered saline (TBS) (pH 7.6) + 5 % fetal bovine serum (FBS) + 10 % rat serum and 0.1 % Tween. Afterwards, the tissue sections were stained with an antibody cocktail containing all three antibodies (Tab. 3.6) diluted in 1x TBS (pH 7.6) + 5 % FBS + 0.1 % Tween (this was also used as washing buffer) and the staining followed the given protocol (washing, 4',6-diamidino-2-phenylindole (DAPI) staining, washing, embedding). Due to the direct labeling of all three antibodies, no step for staining of a secondary antibody was necessary. The stained tissue sections were analyzed with a confocal laser scanning microscope 710 (LSM 710).

3.6.2 Staining of CD4+ T cells, CD8+ T cells and osteoblasts

CD4+ and CD8+ T cells, as well as osteoblasts were stained simultaneously on one tissue section. After thawing and rehydration (Tab. 3.5), tissue samples were blocked in 1x TBS + 10 % FBS and 0.2 % Tween. Then, tissue sections were stained for osteocalcin, as a marker for osteoblasts, in 1x TBS + 5 % FBS and 0.2 % Tween (Tab. 3.6). All the following washing and staining steps were realized in this buffer. After washing, a secondary antibody α-rabbit was applied to the section. After the next washing step, the staining of CD4 followed. The staining signal of CD4+ T cells was improved by the application of a secondary α-rat antibody after washing. Tissue samples were washed, stained for CD8 and finally for DAPI and embedded. The stained tissue sections were analyzed with a confocal laser scanning microscope 710 (LSM 710).

3.6.3 Staining of B cells and osteoclasts

B cells and osteoclasts were also stained together on one tissue slide. After thawing and rehydration (Tab. 3.5), sections were blocked in 1x PBS + 10 % FBS + 10 % rat serum and 0.1 % Tween. An antibody cocktail containing α-B220 (B cell marker) and α-cathepsinK (marker for osteoclasts) (Tab. 3.6) diluted in 1x PBS + 10 % FBS and 0.1 % Tween was applied to the sections. The staining buffer was also used as the following washing buffer. After the washing, an α–rabbit antibody was applied to the tissue sample to visualize the staining for osteoclasts. The following steps of the staining corresponded to the above described general staining protocol (washing, DAPI staining, washing). The embedded tissue sections were analyzed with a confocal laser scanning microscope 710 (LSM 710).

3.6.4 Staining of hypoxic areas and newly formed vessels

Hypoxic areas were identified by the staining of the transcription factor Hif1α and newly formed vessels by the surface marker CD105 (Tab. 3.6). Both targets of interest were stained subsequently on one tissue slide. After washing and rehydration (Tab. 3.5), the blocking step with 1x TBS (pH 7.6) + 0.2 % Tween-20 followed. This buffer was also used for the following staining and washing steps. First, new vessels were stained. After washing, a secondary staining step with an α-rat antibody followed in order to visualize the staining for CD105. Subsequently, hypoxic areas were stained and further visualized by an α-rabbit

antibody. Tissue samples were washed, stained for DAPI and embedded. The stained tissue sections were analyzed with a confocal laser scanning microscope 710 (LSM 710).

Table 3.6: Overview of the antibodies used including their specificity, clone and dilution for the immunofluorescence staining of frozen bone sections

Antibody	Dilution
IHC	
α-mouse B220 PE	1:100
CathepsinK	1:200
CD4 AF594	1:25
α-mouse CD8 PE	1:100
CD68 FITC	1:100
α-mouse CD80 AF647	1:50
α-mouse CD105	1:100
α-mouse CD206 PE	1:100
DAPI	1:1 000
Hif1a	1:100
α-mouse Osteocalcin	1:400
α-rabbit AF647	1:1 000
α-rat AF594	1:1 000

3.6.5 Performed quality controls for immunofluorescence stained bone sections

For the IHC staining, the following quality controls were performed prior to the staining of the experimental bone sections. First, the correct dilution of the used antibodies was determined. The used antibodies were tested in different dilutions on bone test slices. The best antibody dilution was defined as the best signal to background staining. Furthermore, in the case of an indirectly staining (the first antibody was not directly coupled to a fluorochrome), a staining just containing the primary or the secondary antibody, respectively, was done in parallel to a full stain (primary and secondary antibody together on one slide). This was the case for the staining of osteoblasts (osteocalcin), osteclasts (cathepsinK), hypoxic areas (Hif1α) and newly formed vessels (CD105). In addition, for all used staining panels, single staining were done in parallel to the full stain in order to exclude an unspecific binding of one antibody to another one in the full stain antibody solution.

3.6.6 Imaging of immunofluorescence stained bone sections

Immunofluorescence stained tissue sections were imaged with a confocal laser scanning microscope from Carl Zeiss (LSM 710). The scan area was defined as the area including the osteotomy gap and the ends of the four cortical bones, corresponding to the ROI of the histomorphometric analysis (Fig. 3.6). By using the microscope software ZEN, the scan area was determined in the X and Y axis. If necessary, Z stacks were taken in order to take into account non-flatness of the tissue section. The acquisition of the determined scan area was done using the following parameters: frame size: 2 400 x 2 400, averaging number: 2. Afterwards, first, the imaged Z stacks were combined and then the imaged tile scans.

The final image was also further processed and analyzed with the ZEN software for the appearance and distribution of the stained targets of interest (Chap. 3.6.7).

3.6.7 Processing of taken images

Taken immunofluorescence images were further processed and analyzed with the microscope software ZEN (Version 11). In a first step, the intensity of the individual laser was readjusted in order to obtain a strong signal for the respective fluorochrome, without increasing the background signal too. In a second step, each target of interest was evaluated integrating the localization within the scan area (periosteal, endosteal, within the osteotomy gap, within the bone marrow). Consecutive sections were stained for different targets of interest. This allowed the subsequently interpretation of possible co-localization not only for targets stained on the same section, but also for ones on the adjacent sections.

3.7 Micro-Computed tomography

The µCT is a high-resolution imaging technique in order to visualize the 3D microarchitecture and morphology of cortical and trabecular bone by X-rays. The basic principle of X-ray measurement is the tissue specific absorption of X-rays based on its density. A tissue with a higher density like mineralized bone is less transparent for X-rays and will be represented by a lighter color in the visualized depiction. Therefore, tissues of different densities can be non-invasively visualized and evaluated by µCT analysis. For the first time introduced by Feldkamp *et al.*, µCT analyses are nowadays the "gold standard" in research for *in vivo* and *ex vivo* analyses of bony structures, especially in rodents and small animals [119, 120].

3.7.1 Ex vivo measurement of murine femora by µCT

The µCT measurement of the murine left femur of the 21 d animals was done *ex vivo* in a 30 % sucrose solution in a Viva µCT 40. In the Viva µCT 40, the sample is fixed within the device and the X-ray images are taken from different angles around the sample. Concerning the scan resolution, the highest possible resolution of 10.5 µm voxel size was chosen for the analysis. In order to also highly visualize fine structures of newly formed (woven) bone, an energy peak voltage of 55 keV_P was applied to the sample. Based on the chosen energy, a current of 145 µA was applied to the sample. For the scan, a region of around 2 mm around the center of the osteotomy gap was taken, corresponding to the area between the two middle pins of the external fixator. In order to be able to distinguish between mineralized and non-mineralized bone, a grey value threshold for mineralization has to be defined in the analyzing software. The threshold in order to segment the data sets into background and mineralized bone was determined on the distribution of grey values of data sets of µCT analysis of different mice [120]. For this study, female C57BL/6N mice of an age of 12 weeks were used to determine the grey value threshold. This result was confirmed using a mathematical grey value evaluation [121]. The threshold was set to 242, corresponding to a mineralization of 369.9 mg hydroxyapatite per cm^2.

3.7.2 Reconstruction and analysis of the µCT measurement

The reconstruction and analysis of the measured 2D slices (X-rays) were realized by using the evaluation software "µCT Evaluation Program v6.5-3". The automatically reconstructed X-rays (Feldkamp algorithm) were loaded into the program and the volume of interest (VOI) for the evaluation was determined, which correspond for this analysis to 190 slices à 10.5 µm. Therefore, the center of the (former) fracture gap was defined. The final VOI included 95 slices in the direction of the femur head and 95 slices in the direction of the knee. The total callus was encircled on each X-ray as the region of interest and the proportion of mineralized bone within the total bone callus was calculated by using the defined threshold of 242. Afterwards, a 3D reconstruction of the µCT scan was obtained by the encircled X-rays and the used mineralization threshold. This 3D image was the basis to define a bone as bridged or non-bridged. The following also obtained parameters were used for the quantification of the µCT results and therefore the healing outcome: total callus volume (TV), bone volume (BV), ratio of BV and TV (BV/TV) and bone mineral density (BMD). BMD is equal to the mean of TV.

3.8 Statistics

For the statistical evaluation of the obtained data, the statistic program SPSS was used. Data were presented as box plots, including the median (50 % quartile) and the 25 % and 75 % quartiles. All three quartiles are combined in the box of the box plot. This box is bounded by two “T” lines, the Whisker, on the top and on the bottom of the box. The Whisker includes all the values outside of the box, besides the outlier and extreme values. Outliers are depicted as circles, extreme values as arrows.
For all statistical analysis, the Mann-Whitney U test was utilized. Due to the small sample sizes used in this study, a normal distribution of the data was not assumed. If more than just one data pair was compared in one analysis, the Bonferroni correction was also included and indicated in the respective figure. Data were statistically significant if $p \leq 0.05$. Using the Bonferroni correction, the significance level p had to be adapted as follows: $p \leq 0.05/n$, n= number of comparing samples. If, for example, three samples were compared, the lowest significance value had to be $p \leq 0.05/3 = 0.017$ in order to be statistically significant. In the respective graphs, statistical significances were indicated by * above a line. A trend was defined if p was between 0.051–0.1, indicated by # above a line. For the Bonferroni corrected data sets, a trend was defined if p was above the calculated significance niveau and ≤ 0.1.

4 Results

Bone fracture healing is a highly complex process consisting of different but overlapping phases in which different cell and tissue types have to work together in order to enable a complete regeneration of the injured bone. Under normal healing conditions, a fractured bone regenerates completely without scar tissue formation, possessing in the end the same biomechanical properties as before. Between the bone and the immune system, there is a tight interplay and interconnectivity. Therefore, the bone healing process is highly influenced by the immune system.
In order to characterize the occurrence and composition of immune cells of an unaltered healing process during the healing cascade, a non-critical size defect osteotomy model in mice was used. By immunohistology, the immune cell composition was analyzed locally within the osteotomized bone. For the sake of convenience, the osteotomized bone will be further also termed as fractured bone. Simultaneously, the immune cell composition was also investigated systemically, both in the spleen and in the bone marrow (the lymphoid organs), as well as in the peripheral blood. After analyzing the impact of the immune system on the bone regeneration process under normal healing conditions, a possible therapeutical approach to improve the healing outcome via immunomodulation was investigated. Therefore, an adoptive transfer of T_{Reg} prior to surgery was done. In the frame work of this approach, the impact of the environment was also analyzed (SPF vs. semi-sterile (non-SPF) housing) as to consider the status of the adaptive immune system prior to surgery. Under SPF housing conditions, the adaptive immune system is less experienced than in a semi-sterile environment. In this respect, we could already show that the housing of mice influences the outcome of an unaltered healing process [4]. At the end of the project, a potential identified biomarker could be confirmed in a proof of concept study. The validity of this possible biomarker in a human setup will be further investigated in following clinical research studies.

4.1 Analysis of an unaltered healing process in a mouse osteotomy model

The here presented study is the first attempt to link the appearance of immune cells, bone cells, vascularization and hypoxic areas within the specific bone healing phases in a mouse model. The different phases of bone regeneration during an unaltered healing process after injury were analyzed and characterized, within the fractured bone itself but also systemically. This analysis included the evaluation of the spatial and temporal distribution of different tissue and cell types during the consecutive healing phases within the osteotomy gap as well as within the injured organism. The outcome of this part of my thesis is a clearer picture and a deeper understanding of the interconnectivity of the different tissue and cellular components within the regenerating bone during a normal healing process, focusing on components of the adaptive immunity. The analyzed wild type (WT) mice also worked as controls for the immunomodulatory approach to enhance bone healing (Chap. 4.2, 4.3).

4.1.1 Characterization of the different phases of the fracture healing process

The harvested bones of the 21 d mice underwent µCT analysis. µCT measurements are used in order to reconstruct the shape of the healed bone in a certain volume of interest in a 3D image and to determine the amount of newly formed mineralized tissue.
In figure 4.1, a representative image of such a reconstruction of one of the 21 d WT bones is shown.

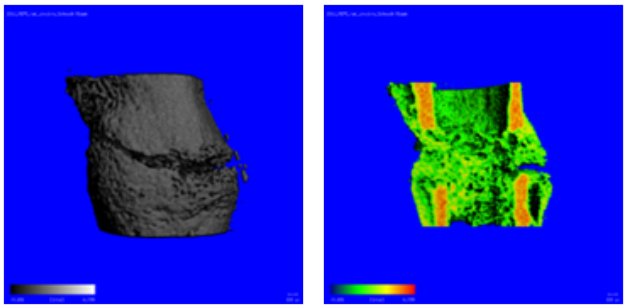

Figure 4.1: µCT evaluation of the healing outcome of WT mice revealed no complete bridging after 21 d. Shown is a representative image of one of the 21 d bones. There was no complete bridging after 21 d. In the right picture, the 3D image of the healing bone is cut sagittally/ frontally to demonstrate the progress of the remodeling process. The color code indicates the mineralization state, with an increasing mineralization from black to white (left) and from blue to red (right), respectively.

After 21 d, the WT bones are not completely bridged. Since the used model is an osteotomy model of a non-critical size defect, the bones would completely heal after a certain time. The 21 d time point was chosen as the last time point of analyzing the healing process in order to be still able to evaluate an improved healing outcome after therapeutic intervention in the immune system of the experimental mice (Chap. 4.2, 4.3).
In general, the bones were harvested and cryo embedded. Serial sections were cut for further histological and immunohistological analysis. The different tissues of the regenerating bone were analyzed based on Movat Pentachrome (MP) stainings. The MP coloration is a useful histological method in order to visualize different tissue components in one staining. Representative pictures of all six investigated time points are displayed in figure 4.2. In addition, magnifications of the fracture area of the later phases of the healing process are presented in order to depict more clearly the predominant tissues present at the respective time points. Following the MP staining, a histomorphometrical evaluation of the fracture gap, including also a defined area around it, was performed (Fig. 4.3).
The different phases of a classical secondary bone healing process were recapitulated in the mouse model: after the early hematoma formation, the fracture gap was filled with connective tissue and further fibrocartilage that was then replaced by maturing cartilage tissue and finally newly formed mineralized bone. In order to evaluate the progression of the healing process by histomorphometry, the following parameters were considered: total callus area, cortical bone, newly mineralized bone, cartilage, bone marrow and connective tissue. The total callus area increased from day 1, showed a peak at day 3 and 7 and decreased again till day 21 (Fig. 4.3). At day 1–3 (hematoma phase), connective tissue and bone marrow cells were dominant in the fracture area. In particular, the relative amount of bone marrow increased from day 1 to day 3, whereas a simultaneously decreasing proportion of mature granulation tissue (evaluated as connective tissue) was seen. At day 7, small isles of cartilage appeared in the investigated area embedded in mature granulation tissue. This represents the phase of fibrocartilage tissue formation, also termed soft callus phase. This soft callus is then replaced by hard callus, consisting of newly formed woven bone (Fig. 4.2, 21 d, bottom). This phase began after 14–21 d. Between day 7 and 14, the whole fracture area was filled with cartilage tissue that became hypertrophic and finally mineralized (Fig. 4.2, MP picture 14 d, bottom). In the hard callus phase that is followed by the remodeling of the newly formed woven bone, the relative amount of newly mineralized bone increased. Furthermore, the area filled with bone marrow also increased, showing the rebuilding of the former medullary canal. In contrast, the percentage of connective tissue as well as cartilage decreased again from day 14 to day 21.

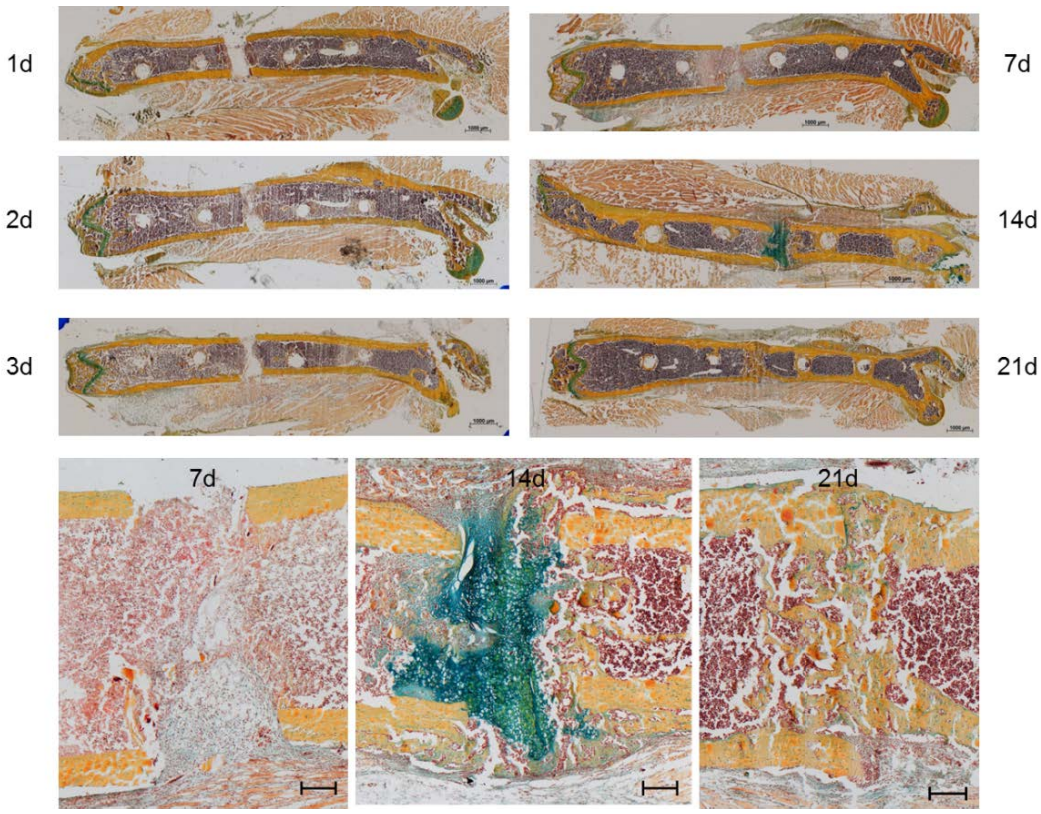

Figure 4.2: The different phases of a classical secondary healing process were recapitulated in the fractured femora. Representative Movat Pentachrome images of the different time points of healing are shown: 1 d post-surgery, 2 d, 3 d, 7 d, 14 d and 21 d. At the bottom, enlarged pictures of the fracture area from the time points 7 d, 14 d and 21 d are depicted, enlighten the predominant tissues present at the respective phases of the healing process: 7 d mature granulation tissue; 14 d cartilage/soft callus; 21 d woven bone. Coloration of the following tissues: mineralized bone and cartilage = yellow, cartilage = blue/green, connective tissue = bluish, bone marrow = purple and cell nuclei = black. Scale bar (bottom): 200 µm

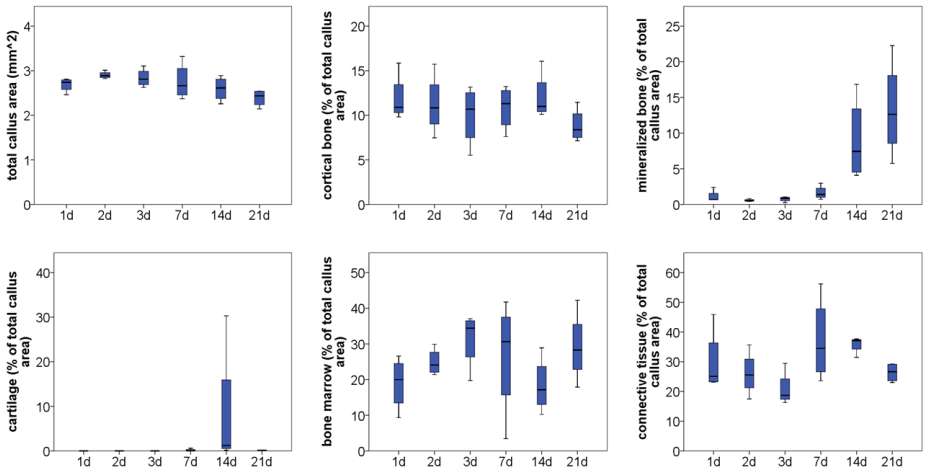

Figure 4.3: Histomorphometrical evaluation of the Movat Pentachrome stainings confirmed the cha-racteristic tissue distribution of the different healing phases. Displayed are the total callus area and the calculated proportions of the investigated tissues types (in and around the fracture gap) at the different healing phases of the osteotomyzed bones: 1 day (d) post-surgery, 2 d, 3 d, 7 d, 14 d and 21 d. n= 4

In addition to the analysis of the different tissue types present in the fractured bone over the healing process, certain populations of cellular subsets of the innate and adaptive immune system, osteoblasts, osteoclasts, as well as hypoxic areas and newly formed vessels were investigated by immunohistological stainings using fluorescence-coupled antibodies (Chap. 4.1.2).

4.1.2 Spatial and temporal distribution of distinct immune cell subsets in the healing mouse femur

This is for the first time that the interplay of both, immune and bone cells, and their context during all bone healing phases are shown. The spatial and temporal distribution of distinct immune cell subsets was investigated by IHC stainings of the tissue sections. The results are presented in the figures 4.4–4.10. A scheme of the investigated fracture area is depicted in the figures. In figure 4.4, the corresponding area of the schemes is depicted in a representative MP staining of a murine fractured femur.
Macrophages expressed different polarization states during healing: MΦ (CD68+, visualized by a green fluorescence signal), M1 (CD68+ and CD80+, light blue) and M2 (CD68+ and CD206+, red). The macrophages changed over the healing process from a first pro-inflammatory (Fig. 4.4, 4.5, indicated by an arrow; hematoma phase) to an anti-inflammatory phenotype (Fig. 4.6, 4.7, indicated by an arrow). M2 macrophages started to appear 3–7 d post-surgery, at the transition from the ending inflammatory/ hematoma to the fibrocartilage phase. They also seemed to enter the fracture side from the surrounding muscle tissue (Fig. 4.7). During the cartilage and hard callus/remodeling phases, predominantly CD68 single positive macrophages were detectable within the osteotomy area (Fig. 4.8, 4.9, indicated by an arrow).
Concerning the distribution of the T cell subsets, they seemed to disappear in the investigated area after day 1/day 2 but directly started to reappear in the bone marrow around the fracture zone (Fig. 4.4–4.7, indicated by an arrow; CD4+ T cells: red; CD8+ T cells: green).

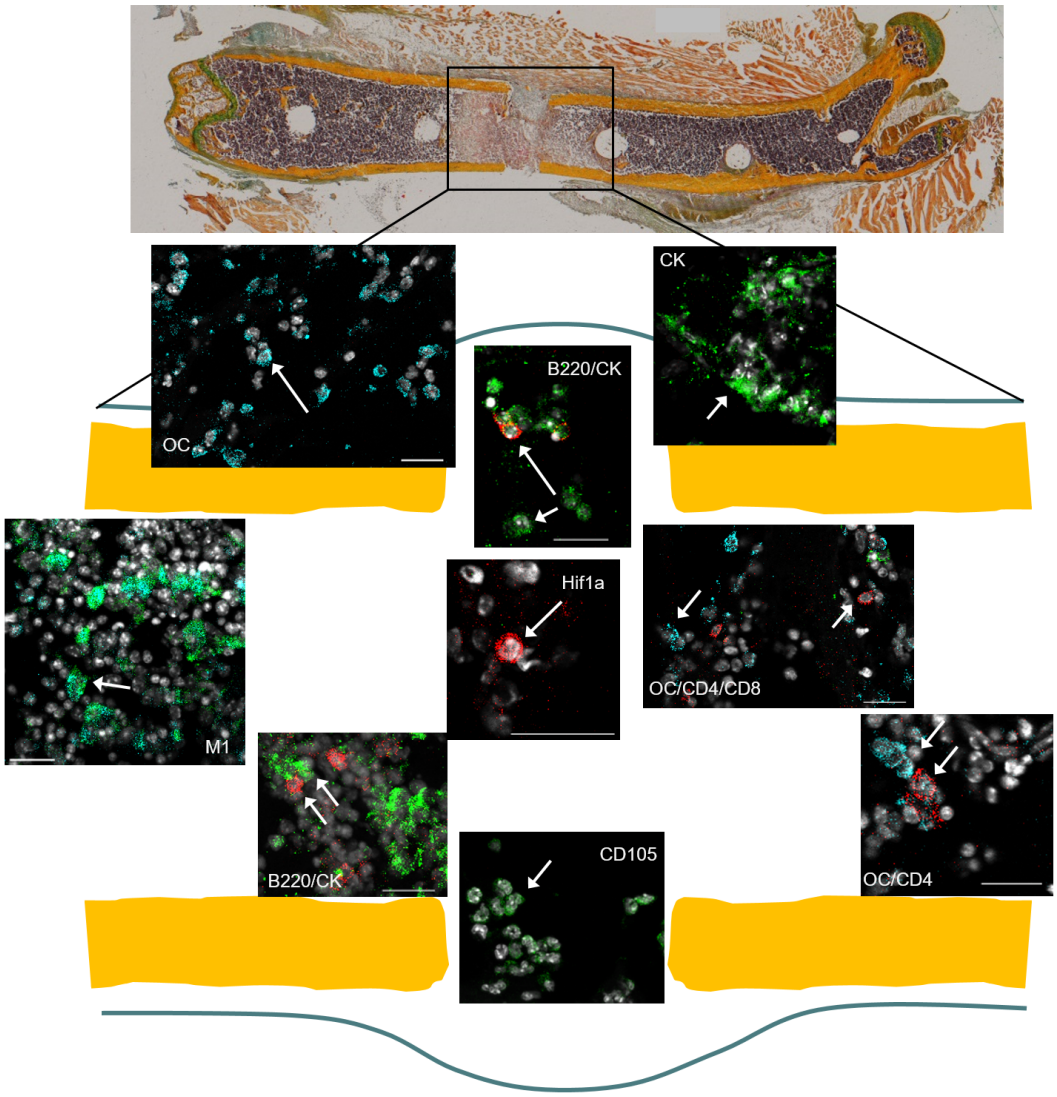

Figure 4.4: Hypoxia induced the expression of Hif1α in the fracture gap. Immunohistological staining within a murine fractured femur 1 day post-surgery. Depicted is a scheme of the analyzed area after osteotomy. On top, a MP stained murine femur and the corresponding area of the scheme are shown (indicated by a black rectangle). The following cellular targets were stained: osteoblasts (osteocalcin, OC, light blue), osteoclasts (cathepsin k, CK, green), CD4+ T cells, (CD4, red), CD8+ T cells (CD8, green), B cells (B220, red), macrophages at different polarization states (MΦ, green; M1, light blue; M2, red), Hif1α as an indicator of hypoxia (Hif1α, red) and newly formed vessels (CD105, green). Stainings were done on consecutive bone sections, also including co-stainings on one slice. Arrows indicate the stained target shown in the respective image. Coloration of the MP picture: mineralized bone and cartilage = yellow, cartilage = blue/green, connective tissue = bluish, bone marrow = purple and cell nuclei = black. Color code of the scheme: cortices = yellow, periosteal callus = blue/green. Scale bar = 20 μm.

In this early healing phase, a direct spatial co-localization of CD4+ T cells and osteoblasts (osteoblasts identified by osteocalcin (OC) staining, visualized by a light blue fluorescence signal) and CD8+ T cells and osteoblasts, respectively, could be visualized. However, both T cell subsets did not seem to directly co-localize. During the later phases of the healing process, CD4+ and CD8+ T cells were consistently present in the bone marrow around the fracture gap.

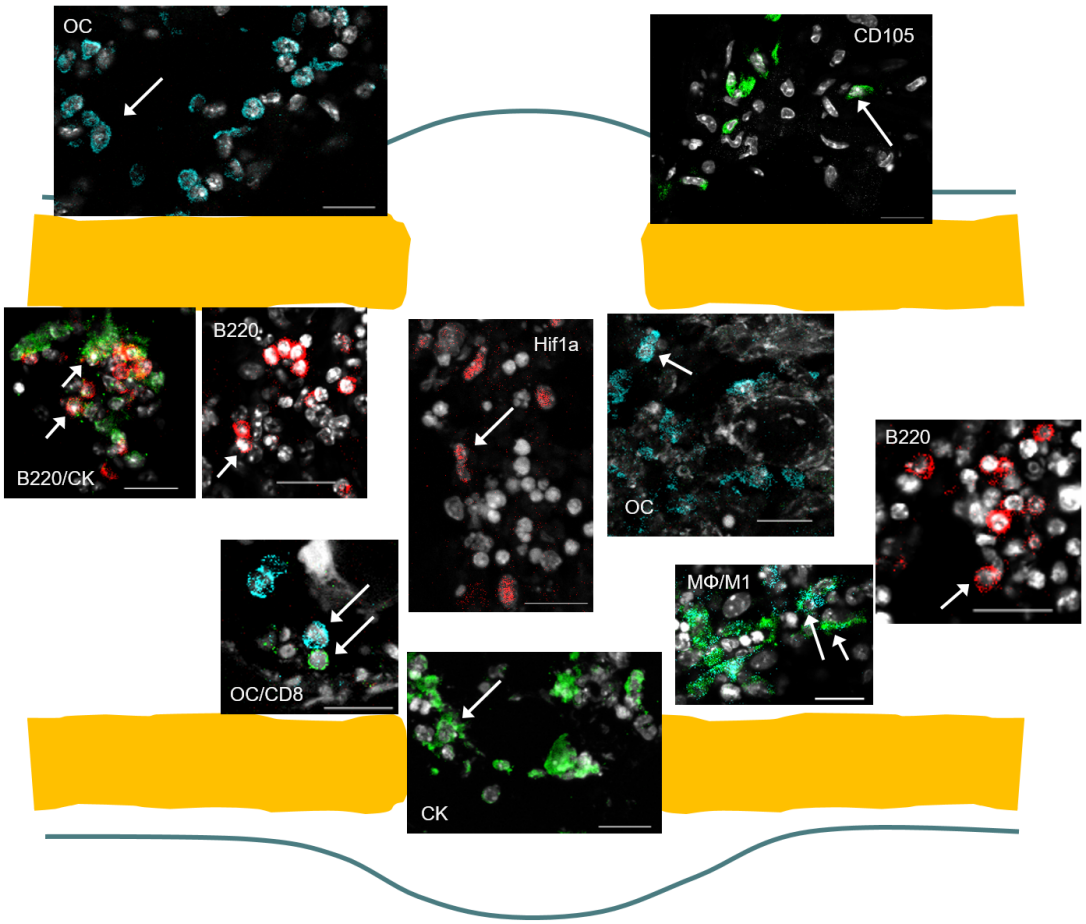

Figure 4.5: T cells seemed to evade from the fracture area. Immunohistological staining within a murine fractured femur 2 days post-surgery. Depicted is a scheme of the analyzed area after osteotomy. The following cellular targets were stained: osteoblasts (osteocalcin, OC, light blue), osteoclasts (cathepsin k, CK, green), CD4+ T cells, (CD4, red), CD8+ T cells (CD8, green), B cells (B220, red), macrophages at different polarization states (MΦ, green; M1, light blue; M2, red), Hif1α as an indicator of hypoxia (Hif1α, red) and newly formed vessels (CD105, green). Stainings were done on consecutive bone sections, also including co-stainings on one slice. Arrows indicate the stained target shown in the respective image. Color code of the scheme: cortices = yellow, periosteal callus = blue/green. Scale bar = 20 μm

The B cell subset (B220, red) was present over the whole healing cascade within the analyzed area. Often, they could be detected in a direct co-localization with cathepsin k+ osteoclasts (Fig. 4.4, 4.5, 4.7–4.9, indicated by an arrow; osteoclasts: CK, green). Osteoclasts, the bone resorbing cells, were first predominantly found at the endosteum and periosteum. Thus, B cells were also often found at the endosteum. As soon as areas of newly formed woven bone appeared in the osteotomy area, osteoclasts were also found around those isles (during the hard callus/remodeling phases). In contrast, the bone forming osteoblasts were more prominent at the periosteum and directly within the fracture gap during the early healing phase (Fig. 4.4–4.6, indicated by an arrow). Later, they were also found at the endosteal site of the cortices and around woven bone isles (Fig. 4.7, 4.8, indicated by an arrow). Hypoxic cells indicated by expressing the hypoxia induced transcription factor Hif1α were detectable in the fracture gap directly after injury (Fig. 4.4, 4.5, indicated by an arrow; red signal).

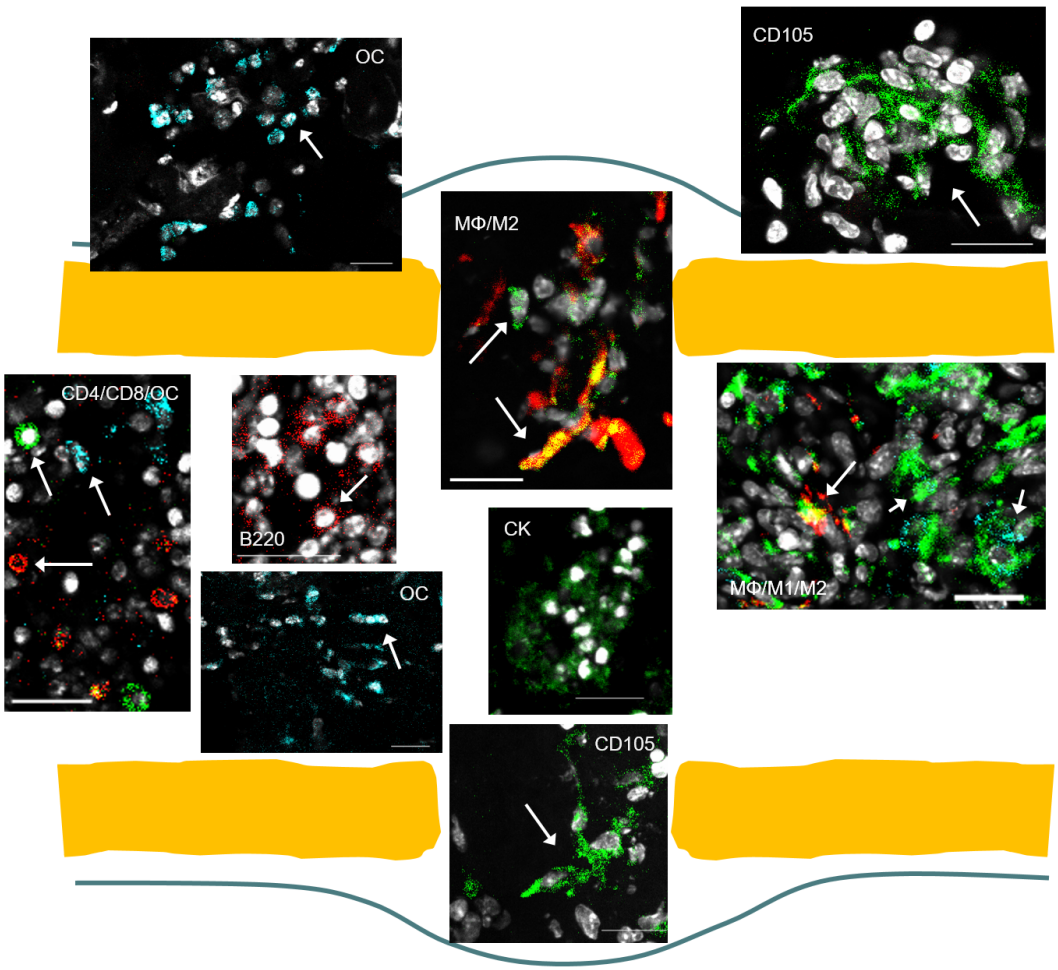

Figure 4.6: Vessel-like structures started to develop in the surrounding tissue. Immunohistological staining within a murine fractured femur 3 days post-surgery. Depicted is a scheme of the analyzed area after osteotomy. The following cellular targets were stained: osteoblasts (osteocalcin, OC, light blue), osteoclasts (cathepsin k, CK, green), CD4+ T cells, (CD4, red), CD8+ T cells (CD8, green), B cells (B220, red), macrophages at different polarization states (MΦ, green; M1, light blue; M2, red), Hif1α as an indicator of hypoxia (Hif1α, red) and newly formed vessels (CD105, green). Stainings were done on consecutive bone sections, also including co-stainings on one slice. Arrows indicate the stained target shown in the respective image. Color code of the scheme: cortices = yellow, periosteal callus = blue/green. Scale bar = 20 μm

Although no Hif1α positive cells could be detected 3 days after surgery, strong signals were again visible 7 d post-surgery (Fig. 4.6, indicated by an arrow). In the later healing phases, no Hif1α signal was measurable in the regenerating bones.
The appearance of newly formed vessels and the necessary CD105+ precursor cells started directly after osteotomy (CD105, green signal). The progenitor cells seemed to enter the fracture area from the surrounding environment (Fig. 4.4–4.6). First, they were present as single cells, later organized as vessel like structures (Fig. 4.7–4.9). In figure 4.10, a schematic summary of the immunohistological findings is displayed, showing the characteristic distribution of the analyzed targets over the healing cascade.

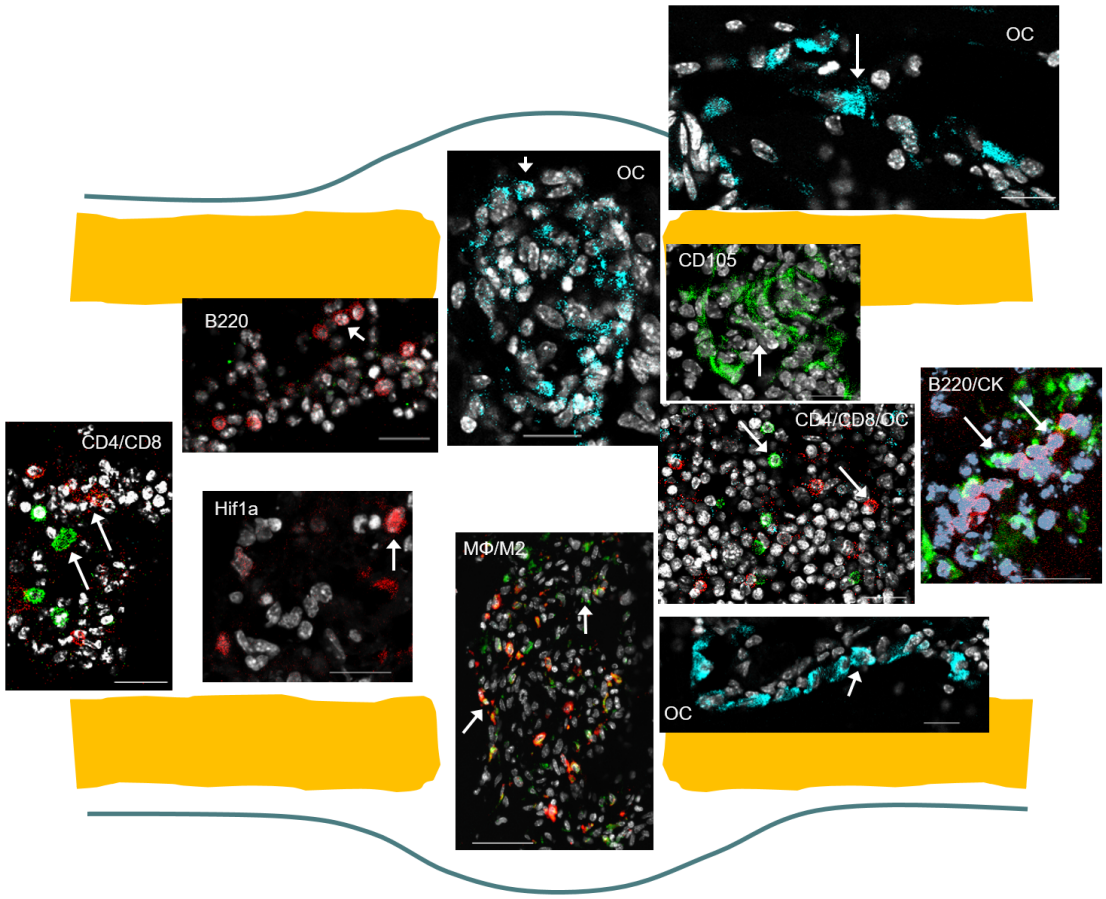

Figure 4.7: M2 Macrophages infiltrated the fracture gap from the surrounding tissue. Immunohistological staining within a murine fractured femur 7 days post-surgery. Depicted is a scheme of the analyzed area after osteotomy. The following cellular targets were stained: osteoblasts (osteocalcin, OC, light blue), osteoclasts (cathepsin k, CK, green), CD4+ T cells, (CD4, red), CD8+ T cells (CD8, green), B cells (B220, red), macrophages at different polarization states (MΦ, green; M1, light blue; M2, red), Hif1α as an indicator of hypoxia (Hif1α, red) and newly formed vessels (CD105, green). Stainings were done on consecutive bone sections, also including co-stainings on one slice. Arrows indicate the stained target shown in the respective image. Color code of the scheme: cortices = yellow, periosteal callus = blue/green. Scale bar = 20 μm

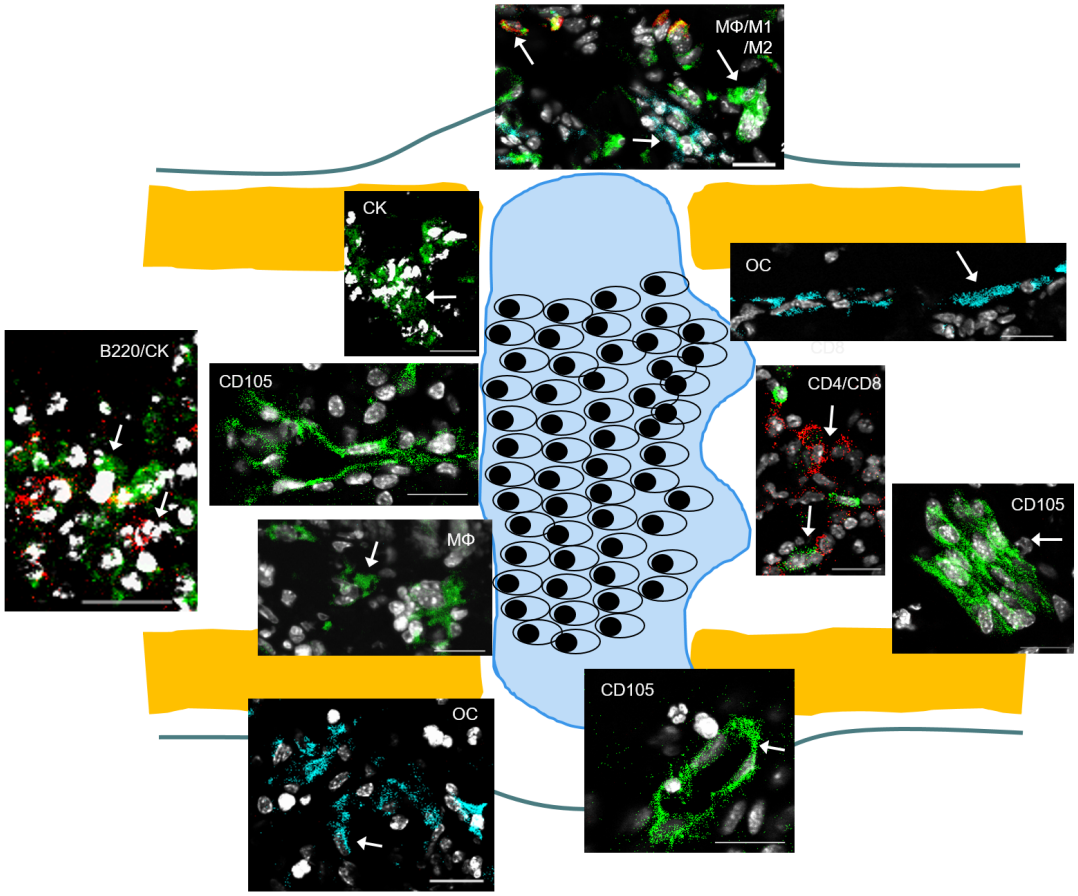

Figure 4.8: Cartilage was the predominant tissue within the fracture gap. Immunohistological staining within a murine fractured femur 14 days post-surgery. Depicted is a scheme of the analyzed area after osteotomy. The following cellular targets were stained: osteoblasts (osteocalcin, OC, light blue), osteoclasts (cathepsin k, CK, green), CD4+ T cells, (CD4, red), CD8+ T cells (CD8, green), B cells (B220, red), macrophages at different polarization states (MΦ, green; M1, light blue; M2, red), Hif1α as an indicator of hypoxia (Hif1α, red) and newly formed vessels (CD105, green). Stainings were done on consecutive bone sections, also including co-stainings on one slice. Arrows indicate the stained target shown in the respective image. Color code of the scheme: cortices = yellow, periosteal callus = blue/green, cartilage with hypertrophic chondrocytes = light blue area in the fracture gap. Scale bar = 20 μm

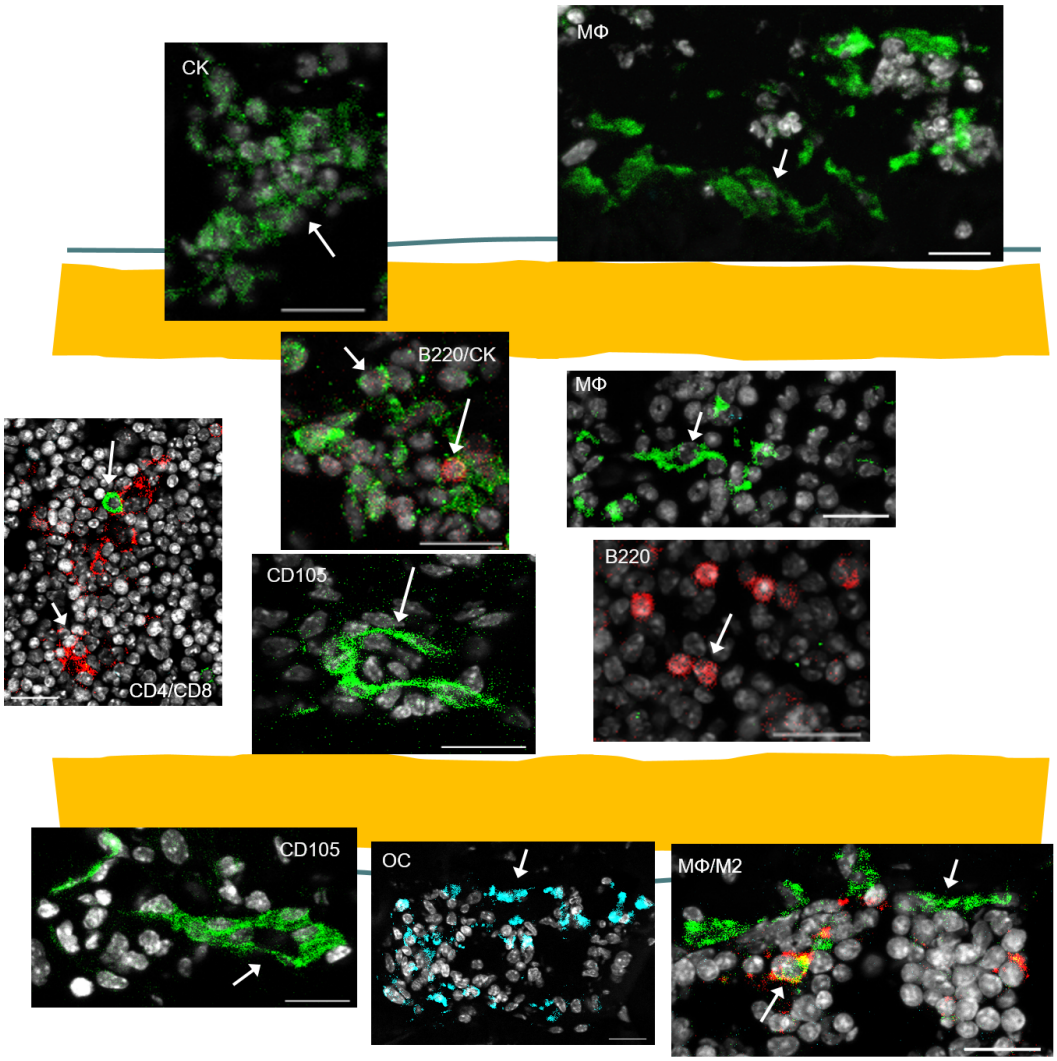

Figure 4.9: The former cellular structure of the medullary cavity was almost reestablished. Immunohistological staining within a murine fractured femur 21 days post-surgery. Depicted is a scheme of the analyzed area after osteotomy. The following cellular targets were stained: osteoblasts (osteocalcin, OC, light blue), osteoclasts (cathepsin k, CK, green), CD4+ T cells, (CD4, red), CD8+ T cells (CD8, green), B cells (B220, red), macrophages at different polarization states (MΦ, green; M1, light blue; M2, red), Hif1α as an indicator of hypoxia (Hif1α, red) and newly formed vessels (CD105, green). Stainings were done on consecutive bone sections, also including co-stainings on one slice. Arrows indicate the stained target shown in the respective image. Color code of the scheme: cortices = yellow, periosteal callus = blue/green. Scale bar = 20 μm

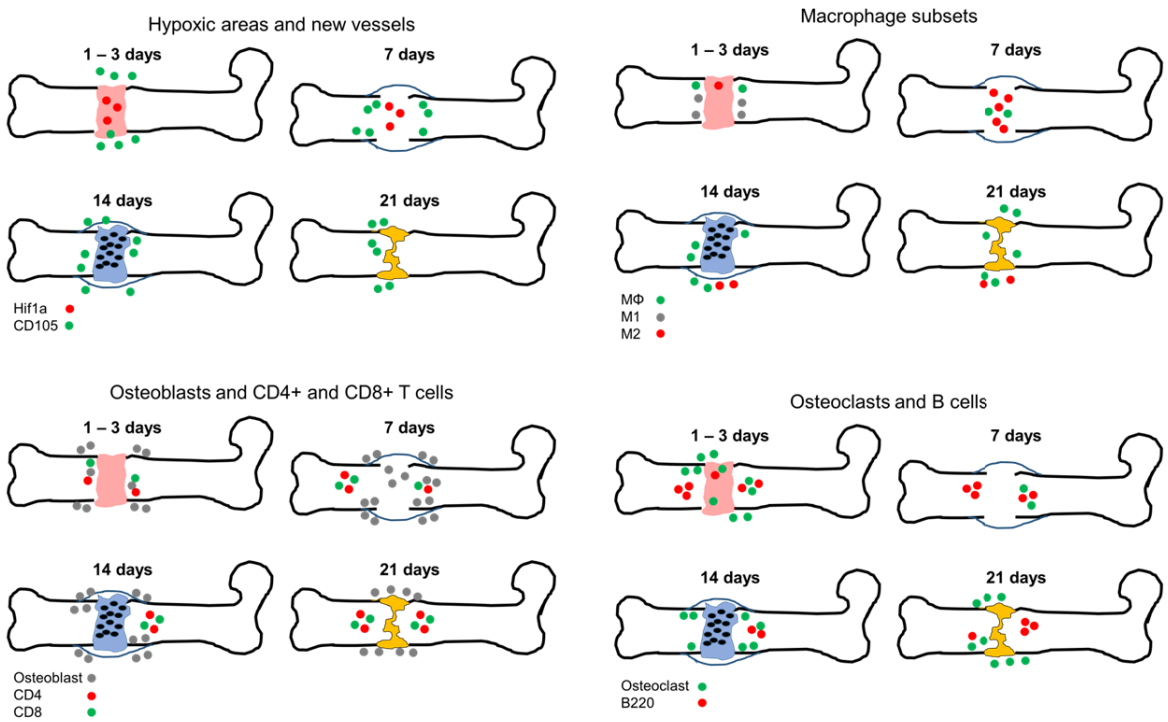

Figure 4.10: Schematic summary of the immunohistological findings. Displayed is the distribution of the analyzed cell types over the healing cascade: 1-3 days (hematoma phase), 7 days (fibrocartilage phase), 14 days (cartilage phase) and 21d (woven bone/remodeling phase). The different cell types are displayed by the indicated color code which is defined in the respective scheme of the different bone healing phases. Colors in the bone scheme: cortices = black, hematoma = rose, callus = blue, cartilage with chondrocytes = light blue with black dots, and newly formed bone = yellow.

4.1.3 Systemic distribution of specific immune cell subsets over the healing process

In addition to the tissue and cellular distribution within the fractured bone itself, possible systemic changes in the organism over the healing process were also of interest for the study. Therefore, the composition of distinct cellular subsets of the adaptive immune system was analyzed by flow cytometry. The study focused on the population of CD4+ and CD8+ T cells. The T cells were analyzed in total as well as the population of activated ones. Furthermore, effector and memory T cell subsets and the subpopulation of CD4+ T_{Reg} were evaluated. In addition, possible changes in the interplay of T_{Reg} and effector T cells were one of the main interests during the evaluation of the therapeutic intervention approach of this study (Chap. 4.2, 4.3). In order to analyze changes in the cellular distribution of the above mentioned cell populations, the following tissues were analyzed: spleen and bone marrow as parts of the lymphoid system as well as the peripheral blood. The bone marrow is the place where most of the memory T cells, but also T_{Reg} reside. A main proportion of T_{Reg} is further located within the spleen, one of the main tissues of the lymphatic system. The peripheral blood was also chosen for these analyses because it is directly interconnected to the vascular system of the fractured bone. Thereby, cellular processes actually taking place, like the recruitment of certain cell subsets as e. g. effector T cells, could be visualized in the organism over the healing cascade.

The proportion of the population of total CD4+ and CD8+ T cells within the pool of CD3+TCR$\alpha\beta$+ T cells clearly decreased directly after surgery in all three tissues (Fig. 4.11

A). This decrease could also be detected in the bone marrow for CD4+CD25+ T cells, and in all three organs for the subset of CD8+CD25+ T cells (Fig. 4.11 B). This clearly illustrates the homogeneous impact of the surgery on the systemic cellular distribution. The percentage of CD4+ T cells instantly increased in the early fracture healing phase, afterwards a constant decrease was visible in all three tissues over the later healing phases. Nevertheless, the total population of CD4+ T cells was not different in the three analyzed tissues during the healing process. In contrast, the proportion of the CD8+ T cell population increased from day 1/2 in the blood and spleen over the healing cascade. This increase was more distinct in the blood regarding the pre-surgery value. In the bone marrow, in contrast, the percentage of CD8+ T cells decreased over the healing period.
The compartment of CD4+CD25+ and CD8+CD25+ T cells (including activated T cells and T_{Reg}) stayed relatively stable over the healing time in the blood and the spleen (Fig. 4.11 B). A different picture was detected for these cells in the bone marrow. The percentage of CD4+CD25+ T cells first increased at 3 d and further strongly decreased again in the granulation/fibrocartilage/cartilage phases. This was followed by an increase again till day 21, reaching almost the pre-osteotomy value (Fig. 4.11 B left). For the CD8+CD25+ T cells, approximately the same picture was also seen; just to a higher extend (Fig. 4.11 B right).
The following T cell subpopulations of both T cell compartments were also investigated: effector T cells, effector memory T cells and central memory T cells. For CD8+ T effector cells, a negative impact in bone repair was already shown in human and mice samples [4]. The three cell subpopulations were gated as follows: effector T cells (T_{EF}): CD4+ or CD8+/CD62L-CCR7-CD25+; effector memory T cells (T_{EFM}): CD4+ or CD8+/CD62L-CCR7-CD25- and central memory T cells (T_{CM}): CD4+ or CD8+/CD62L+CCR7+.

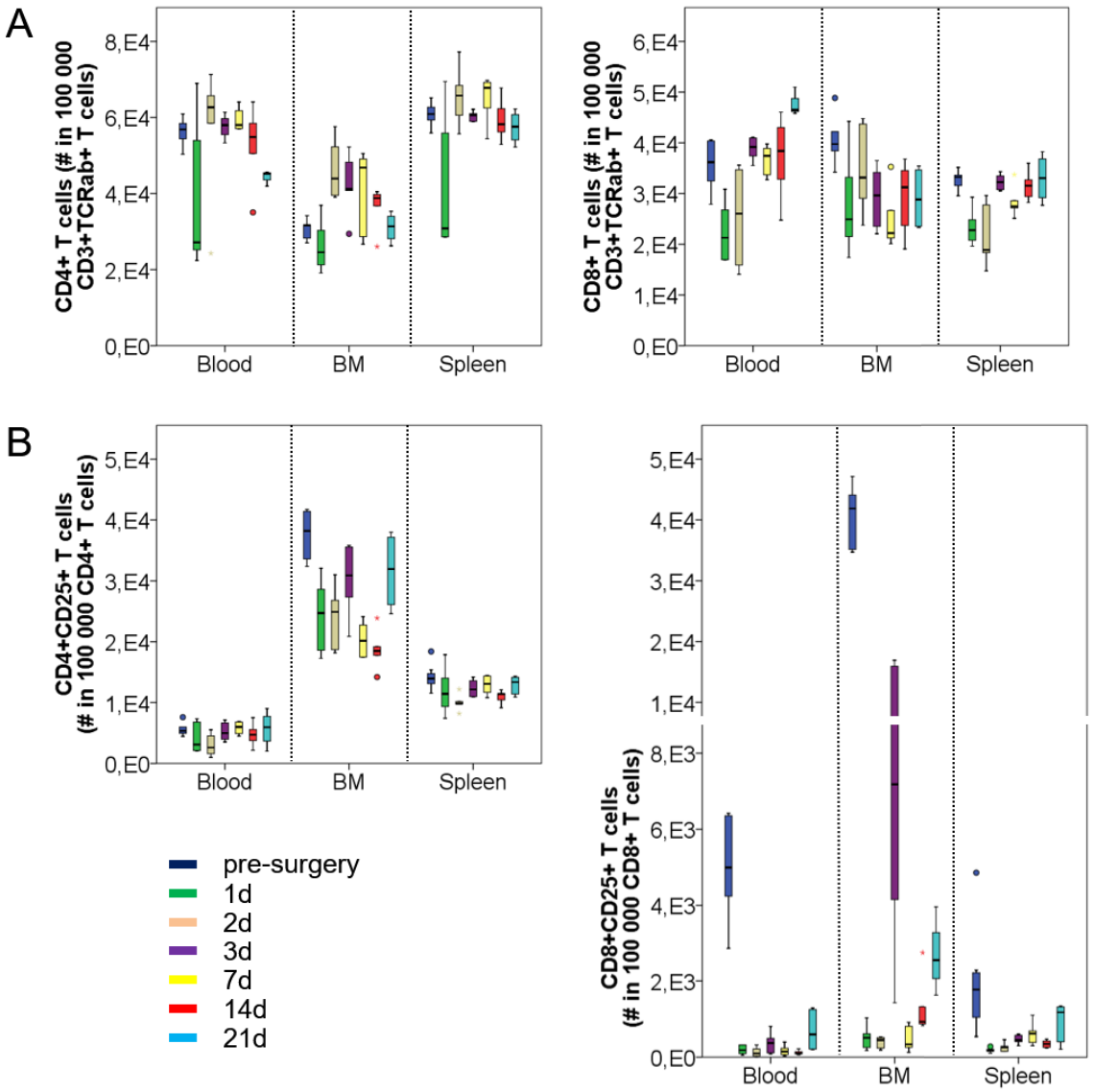

Figure 4.11: CD4+ and CD8+ T cells, as well as their CD25+ subsets showed different expression pattern over the healing cascade of an unaltered bone repair process. Percentage of CD4+ and CD8+ T cells in blood, bone marrow and spleen (A), percentage of CD4+CD25+ and CD8+ CD25+ T cells (activated T cells and T_{Reg}) in all three tissues (B). CD4+ and CD8+ T cells were calculated on the basis of gated CD3+/TCRαβ+ T cells and CD25+ T cells on the basis of gated CD4+ and CD8+ T cells. Blue: pre-surgery, green: 1 day post-surgery, beige: 2 d, purple: 3 d, yellow: 7 d, red: 14 d, light blue: 21 d. n=5–6

For the CD4+ and CD8+ T_{EF}, their proportions decreased in the hematoma phase (Fig. 4.12 A, 4.13 A, T_{EF}). Afterwards, the percentages increased again, for the bone marrow and the spleen even higher as the pre-surgery value. For all three tissues, the value of the pre-osteotomy state was somewhere in between the values detected at the different harvesting time points. The CD4+ and CD8+ T_{EFM} subpopulation showed higher percentages directly after surgery in all three tissues. This illustrates again the consistent impact of the surgery on these cellular subsets (Fig. 4.12 A, 4.13 A, T_{EFM}). Concerning their behavior over the healing period, they stayed relative constant in all three tissue types.

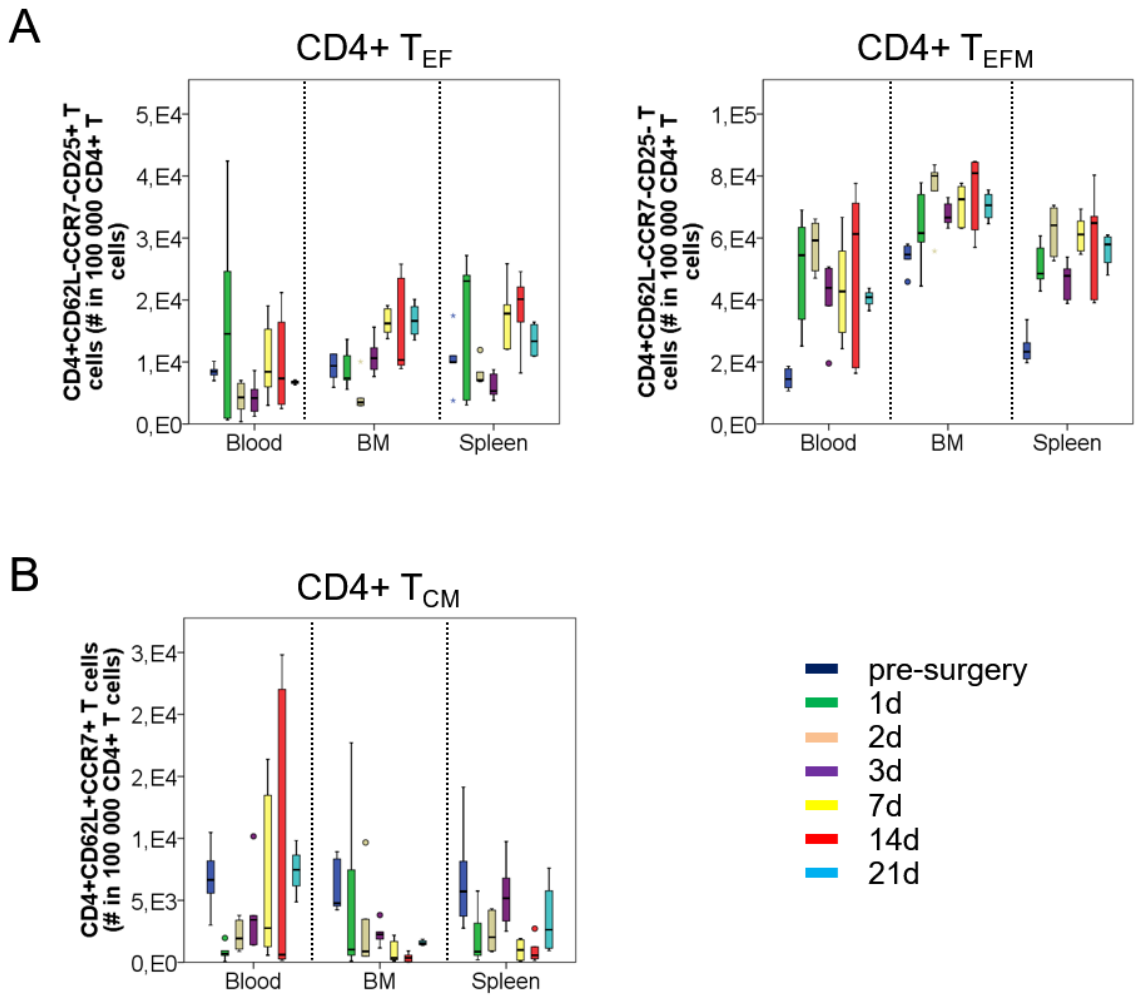

Figure 4.12: CD4+ effector T cells were upregulated during the regeneration of an unaltered bone repair process. CD4+ T_{EF}, T_{EFM} and T_{CM} distribution over the healing cascade of an unaltered bone repair process. Flow cytometry analysis of the percentage of CD4+ T_{EF} and T_{EFM} (A), percentage of CD4+ T_{CM} (B) in blood, bone marrow and spleen. Cells were calculated on the basis of gated CD3+/TCRαβ+/CD4+ T cells. Blue: pre-surgery, green: 1 day (d) post-surgery, beige: 2 d, purple: 3 d, yellow: 7 d, red: 14 d, light blue: 21 d. n=5–6

However, they slightly in- and decreased between the early and late healing phase in the distinct organs. For all, the pre-surgery value was the lowest with regard to the one of the other healing time points. This demonstrates a consistent tissue independent increase. The subpopulation of T_{CM} of the CD4+ and CD8+ compartments displayed a decrease due to the surgery. This was followed by a further constant decrease in the bone marrow and spleen (Fig. 4.12 B, 4.13 B, T_{CM}). In contrast, in the blood, the percentage of T_{CM} slightly increased over the healing cascade, reaching the pre-surgery value after 21 d. The pre-surgery values were almost equal in all three tissues. CD4+ T_{Reg} were identified by the marker set of CD4, CD25 and FOXP3 (Fig. 4.14). In the bone marrow, their proportion constantly increased over the healing process. This was not seen in the peripheral blood and spleen. In these two organs, the percentage of T_{Reg} stayed relative constant during the regeneration process. These findings clearly illustrate the different behavior of the three analyzed tissues regarding the proportion of T_{Reg} during bone regeneration.

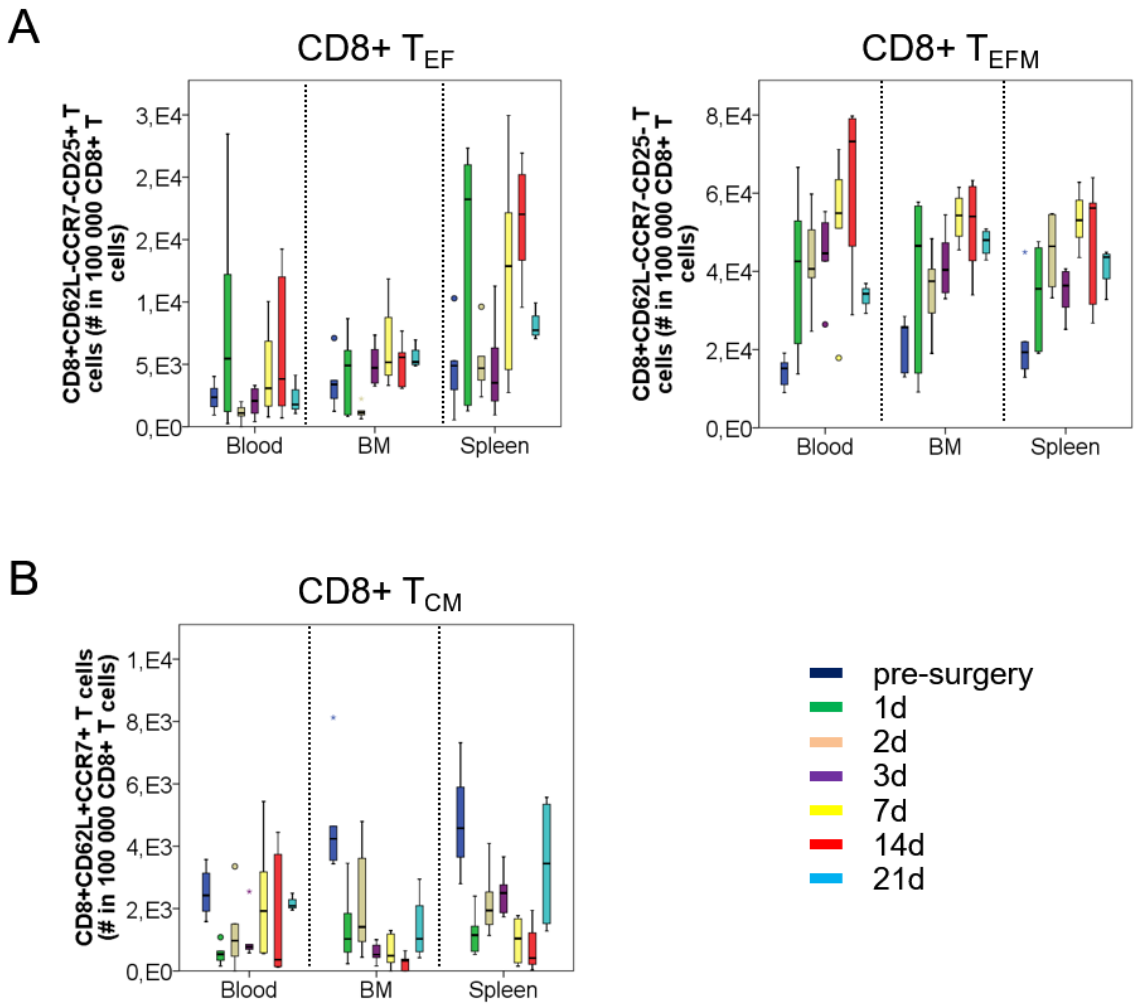

Figure 4.13: CD8+ effector T cells were upregulated during the regeneration of an unaltered bone repair process. CD8+ T_{EF}, T_{EFM} and T_{CM} distribution over the healing cascade of an unaltered bone repair process. Flow cytometry analysis of the percentage of CD8+ T_{EF} and T_{EFM} (A), percentage of CD8+ T_{CM} (B) in blood, bone marrow and spleen. Cells were calculated on the basis of gated CD3+/TCRαβ+/CD8+ T cells. Blue: pre-surgery, green: 1 day (d) post-surgery, beige: 2 d, purple: 3 d, yellow: 7 d, red: 14 d, light blue: 21 d. n=5–6

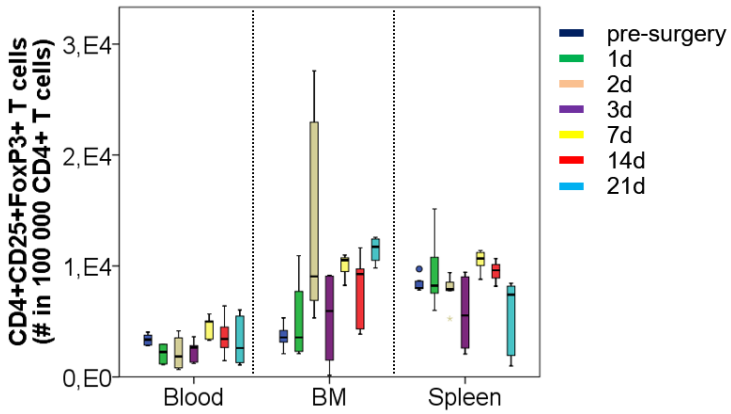

Figure 4.14: CD4+ T_{Reg} showed different expression pattern over the healing cascade of an unaltered bone healing process. Percentage of CD4+ T_{Reg} in blood, bone marrow and spleen. CD4+ T_{Reg} were calculated on the basis of gated CD3+/CD4+ T cells. Blue: pre-surgery, green: 1 day (d) post-surgery, beige: 2 d, purple: 3 d, yellow: 7 d, red: 14 d, light blue: 21 d. n= 6

4.2 Therapeutic intervention in a mouse osteotomy model

In the here presented part of my thesis, I focused on the potential positive impact of T_{Reg} in an unaltered fracture healing process. I also focused on the systemic distribution of T_{EF} and memory cells of CD4+ and CD8+ T cells in order to include their interaction in the healing cascade as potential "bad guys" into my analyses. CD8+ T_{EMRA} were already identified as an unfavorable cell population for a successful healing outcome [4]. This was shown in blood samples from human fracture patients with a delayed healing outcome as well as in the also for this study used mouse osteotomy model.

4.2.1 Therapeutic intervention: Adoptive transfer of murine regulatory T cells prior to surgery

4.2.1.1 Characterization of freshly isolated and pre-activated murine regulatory T cells

The population of T_{Reg} consists of two main subpopulations: thymus-derived nT_{Reg} and in the periphery induced iT_{Reg}. In addition, iT_{Reg} can also be induced *in vitro* out of CD4+FOXP3-T cells, under T cell receptor (TCR) stimulation and a simultaneous presence of TGF-β and rmIL-2. Although the phenotypical and functional discrimination between nT_{Reg} and iT_{Reg} is still under debate, iT_{Reg} are described to be more involved in foreign antigen driven immune reactions, chronic inflammatory conditions and tolerance of mucosal surfaces. In contrast, nT_{Reg} exhibit more involvement in auto-antigen related circumstances balancing the immune homeostasis [122, 123]. For the here presented study, murine T_{Reg} isolated from spleen and lymph nodes of donor mice by MACS were used, representing the pool of nT_{Reg}. After MACS, the purity of isolated T_{Reg} was validated by flow cytometry.

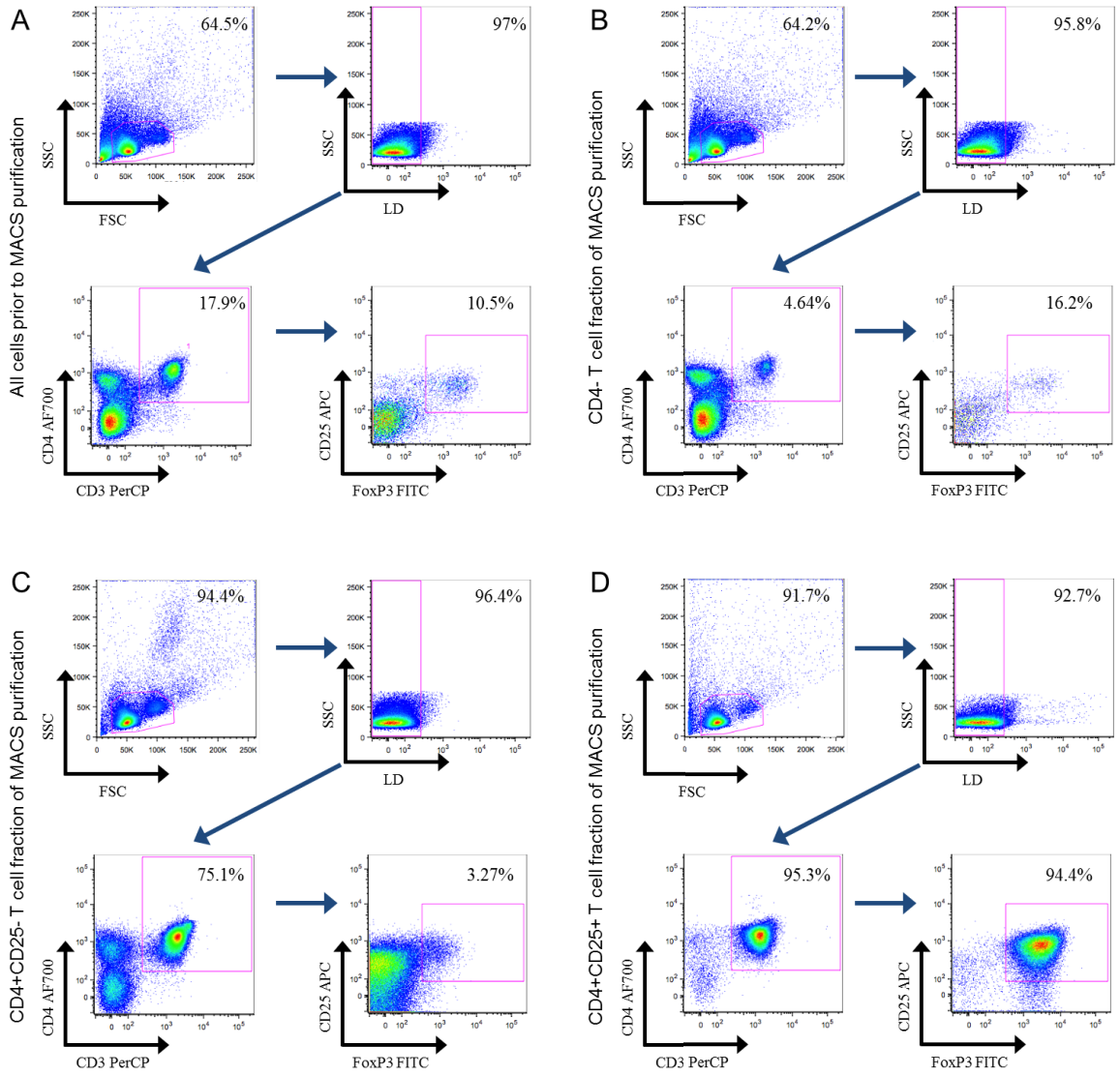

Figure 4.15: MACS technique is a useful method to isolate murine CD4+ T_{Reg}. Representative flow cytometry scheme of a MACS purification. Shown are the different cell fractions of the MACS procedure: cells prior to isolation (A), CD4- T cell fraction (B), CD4+CD25- T cell fraction (C) and the isolated T_{Reg} (D). The gating scheme was as follows: FCS/SSC → living cells (LD-) → CD3+CD4+ → CD25+FOXP3+. Percentages of the gated cells are indicated in the respective dotplots and represent the proportion of cells based on the former gated cell population (frequency of parent).

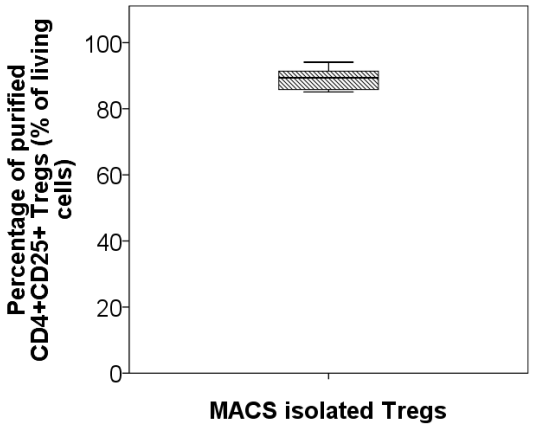

Figure 4.16: Murine CD4+ T_{Reg} were isolated with a high purity by MACS purification. The percentage of purified murine T_{Reg} was based on the population of living cells. n= 12.

An exemplary flow cytometry analysis of one T_{Reg} isolation is presented in figure 4.15. Depicted are the different fractions taken during the MACS purification procedure (sample prior to purification; CD4- fraction; CD4+CD25- fraction and purified T_{Reg} (CD4+CD25+) (Fig. 4.15 A–D). T_{Reg} were isolated with a purity of ≥ 85 % based on the living cells (Fig. 4.16).
After confirming the high purity of MACS isolated murine T_{Reg}, their functionality also had to be evaluated prior to transfer into recipient mice. In human approaches of immunotherapy where T_{Reg} are used, T_{Reg} are isolated from the peripheral blood of the patient, taken in culture, expanded and transferred back to the patient [124, 125, 126]. Thus, T_{Reg} become pre-activated prior to their use in the patient. Based on this procedure, the question arises whether murine T_{Reg} also have to be pre-activated before adoptive transfer in my study. Therefore, before testing their functionality, I established a pre-activation culture of freshly isolated murine T_{Reg} using α-CD3/α-CD28 antibodies for the TCR stimulation and two different concentrations of the interleukin rmIL-2: 50 ng/ml and 360 ng/ml, respectively. Cultured cells were harvested at different time points: 12 h, 24 h, 48 h and 72 h. Already after a cultivation of 12 h, the percentage of living cells decreased for both concentrations of rmIL-2. This was even more clearly seen at the later cultivation time points. Furthermore, the percentage of CD3+CD4+ T cells in the population of living cells decreased from 12 h to 72 h by half from around 80 % to 40 % (also for both concentrations of rmIL-2) (Tab. 4.1). The percentage of CD25+FOXP3+ T_{Reg} cells within the CD3+CD4+ population stayed relative stable over the different pre-activation periods (~50–60 %). The surface marker CD69 was included into the flow cytometry analysis after T_{Reg} cultivation in order to evaluate the activation of cultured T_{Reg}. The expression of CD69 was only evaluated from the CD25highFOXP3+ T_{Reg} (Fig. 4.17 B). An increase of the expression of CD69 was seen as an indication of an activation of T_{Reg} due to the cultivation. For both concentrations of rmIL-2, the expression of CD69 decreased from 12 h to 48 h (~50 % to ~20 %), followed by an increase to 72 h (~70 %).

Table 4.1: Pre-activation of freshly isolated murine T_{Reg}. Two different concentrations of murine recombinant IL-2 (mrIL-2) were used. Illustrated are the percentages of the different cell populations after flow cytometry analysis as frequency of parent at the respective time points of harvest.

Approach	Time	CD3+CD4+ [%]	CD25+FOXP3+ [%]	CD25high [%]	CD69+ [%]
rmIL-2	12 h	86.0	87.0	60.1	51.8
50 ng/ml	24 h	63.8	86.1	51.9	33.1
	48 h	48.5	85.5	49.5	29.0
	72 h	42.1	82.9	51.8	70.6
rmIL-2	12 h	86.6	86.9	64.5	55.6
360 ng/ml	24 h	62.5	84.8	56.9	24.0
	48 h	52.4	84.0	42.7	24.9
	72 h	43.3	85.3	59.0	70.7

Although there was a higher expression of CD69 after a pre-activation culture of 72 h, I decided to test the functionality of pre-activated murine T_{Reg} after a cultivation of 12 h and with the higher amount of rmIL-2 (360 ng/ml). The reason therefore was the rapid decrease of living cells and of the proportion of the CD3+CD4+ cell population within an ongoing cultivation. The rationale for the higher amount of rmIL-2 was that the CD25highFOXP3+ T_{Reg} showed a slightly higher percentage in the culture with the higher rmIL-2 (64.5 % vs. 60.1 %) as well as a slightly higher expression of CD69 compared to the culture with 50 ng/ml rmIL-2 (55.6 % vs. 51.8 %) (Tab. 4.1). An exemplary flow cytometry analysis is shown in figure 4.17, illustrating the gating for the freshly isolated (A) and further for the pre-activated T_{Reg} (360 ng/ml) (B). Figure 4.17 C represents an overlay of the histogram for the CD69 expression of CD25highFOXP3+ T_{Reg} of freshly and pre-activated ones, showing clearly the shift of the expression after pre-activation culture.
For the functionality test, the suppressive capacity of freshly isolated and pre-activated T_{Reg} was evaluated in a T_{Reg} suppression assay. The basic principle of this suppression assay is a co-culture setup of CD4+CD25- responder T cells (T_{Resp}) and T_{Reg}. If functional, T_{Reg} suppress the proliferation of the T_{Resp} in a concentration dependent manner.
In figure 4.18, a gating scheme of a flow cytometry analysis of the 1 to 2 setup (T_{Resp} to T_{Reg}) is exemplary illustrated. The proliferation of the T_{Resp} was visualized by a cell proliferation dye (CPD eF450). After a culture of 2 days, the fluorescence signal of CPD eF450 shifts to the left, indicating the proliferation of the labeled T_{Resp} cells (Fig. 4.18 E). To a lesser extent, this shift was also seen when twice as much T_{Reg} as T_{Resp} were co-cultured in one well (Fig. 4.18 A–D). This illustrates the suppressive effect of freshly isolated T_{Reg}. In figure 4.18 B, the different generations of the proliferating T_{Resp} cells are depicted in the CD25 APC/ CPD eF450 gate. Pre-activated T_{Reg} did not show this concentration dependent suppressive effect on the proliferation of T_{Resp} cells anymore (Fig. 4.19 A–D).

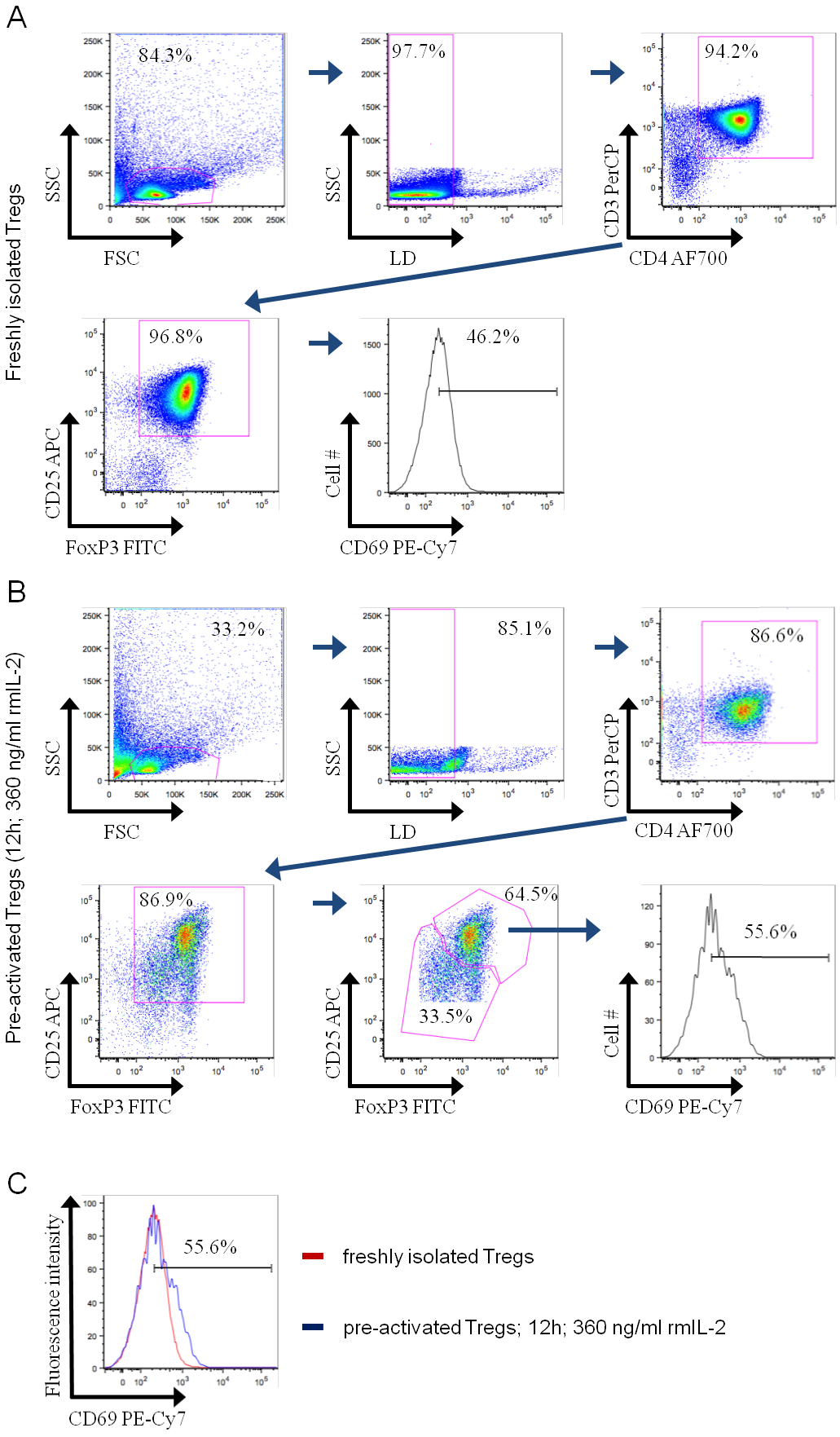

Figure 4.17: Pre-activation of freshly isolated murine CD4+ T_{Reg} led to an upregulation of CD69. Flow cytometry analysis of the pre-activation of freshly isolated murine T_{Reg}. Illustrated are the freshly isolated T_{Reg} (A), the pre-actived ones (B) and an overlay of the histograms of the expression of the surface marker CD69 of both (C).

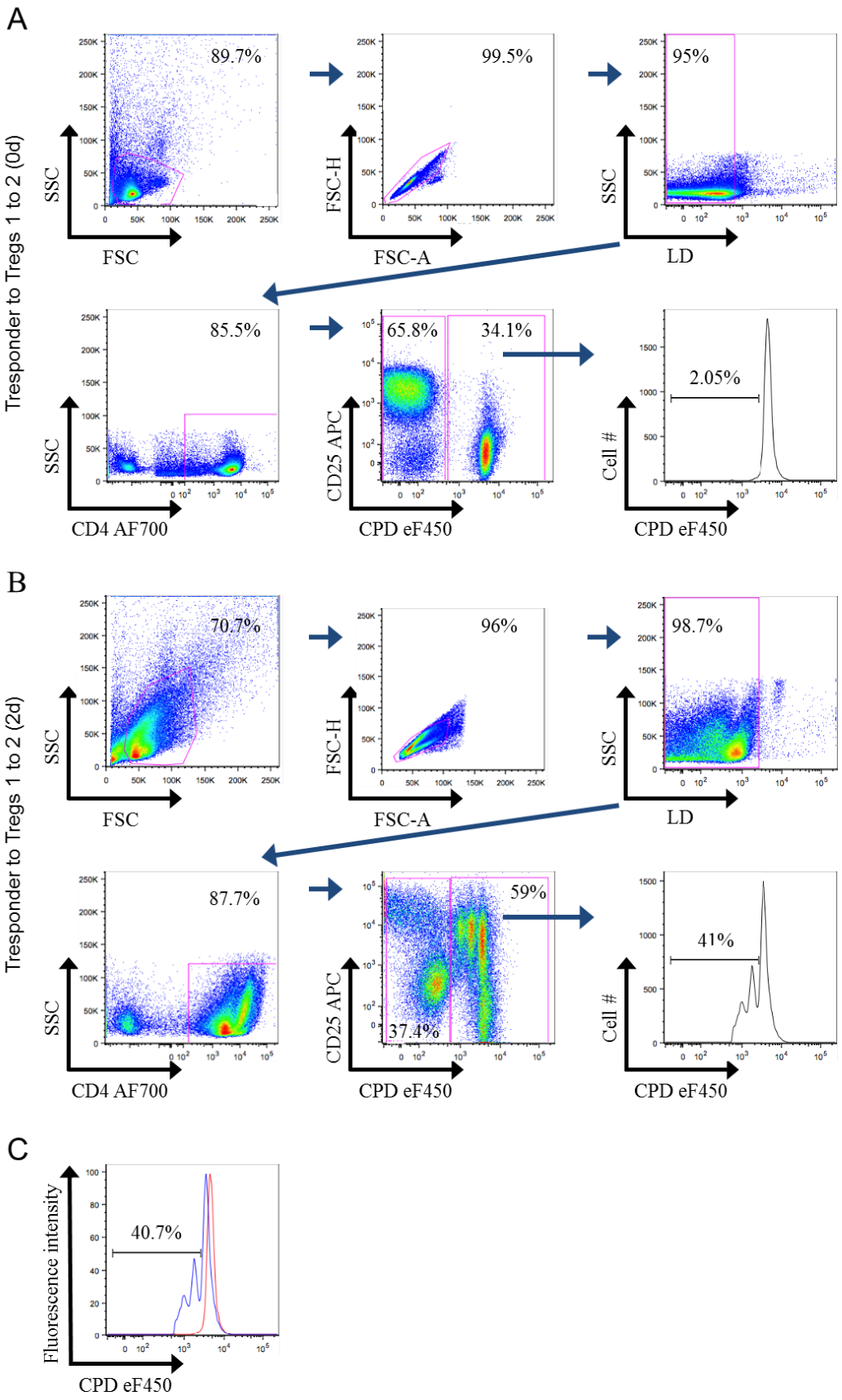
A
Tresponder to Tregs 1 to 2 (0d)
89.7%
SSC
FSC
99.5%
FSC-H
FSC-A
95%
SSC
LD
85.5%
SSC
CD4 AF700
65.8%
34.1%
CD25 APC
CPD eF450
2.05%
Cell #
CPD eF450
B
Tresponder to Tregs 1 to 2 (2d)
70.7%
SSC
FSC
96%
FSC-H
FSC-A
98.7%
SSC
LD
87.7%
SSC
CD4 AF700
59%
37.4%
CD25 APC
CPD eF450
41%
Cell #
CPD eF450
C
40.7%
Fluorescence intensity
CPD eF450

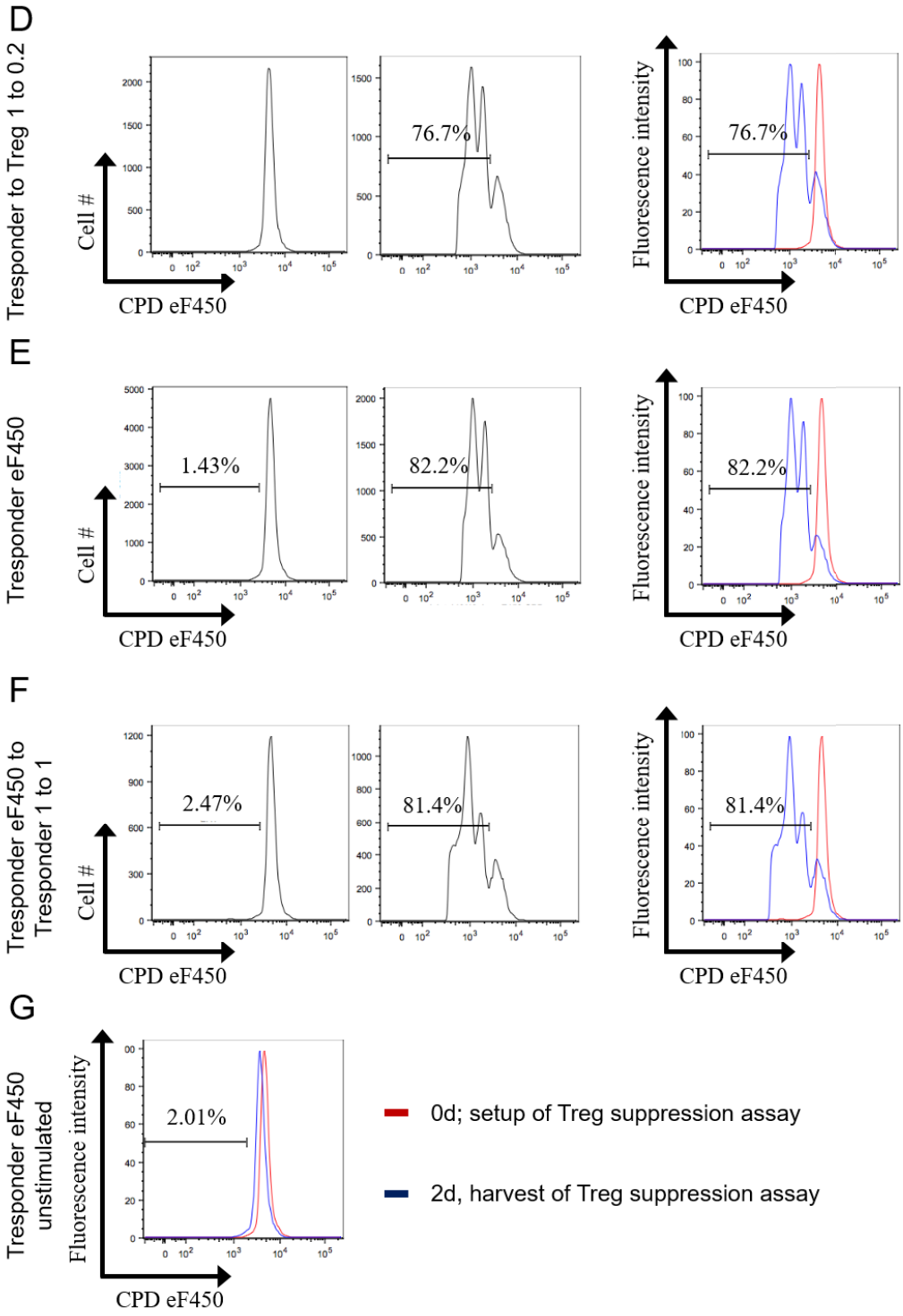

Figure 4.18: Freshly isolated CD4+ murine T_{Reg} suppressed the proliferation of co-cultured CD4+CD25- responder T cells. Illustrated is the flow cytometry evaluation of the suppression assay. A–C shows the gating scheme of the co-culture setup of CD4+CD25- T_{Resp} cells to T_{Reg} 1 to 2, at 0 d (A), at the time point of harvest after 2 d (B) and the overlay of the cell proliferation dye eF450 signal (C). The co-culture setup of 1 to 0.2 is depicted by the respective histograms of the CPD eF450 signal (D). E–G represents internal assay controls: proliferation of T_{Resp} alone (E); labeled T_{Resp} to unlabeled T_{Resp} 1 to 1 (F) and unstimulated T_{Resp} (G). Arrangement of histograms: left: 0 d, middle: 2 d, right: overlay of both time points. Color code of the overlay histograms: red = CPD eF450 signal at 0 d; blue = CPD eF450 signal at the day of harvest (2 d).

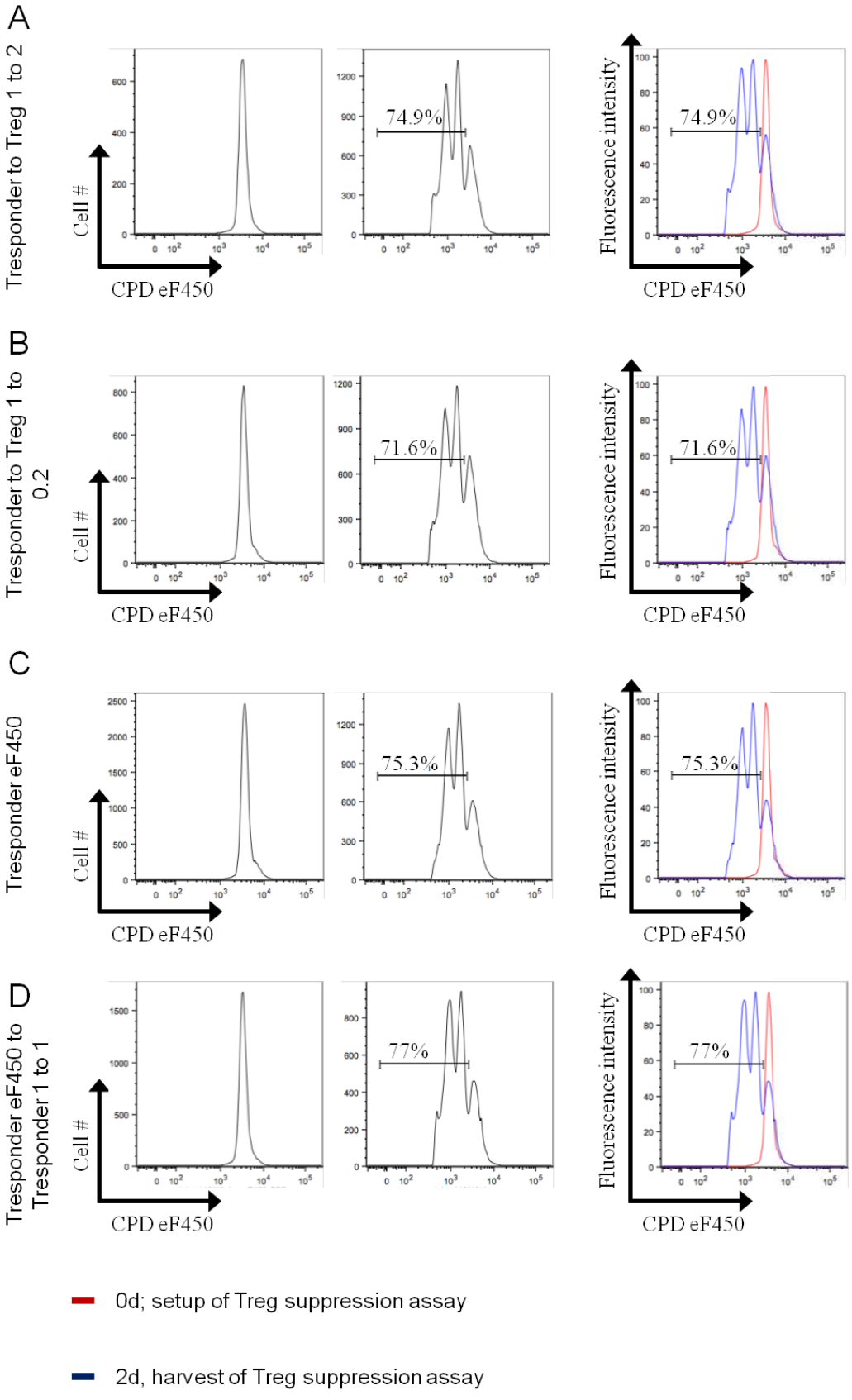

Figure 4.19: Pre-activated murine CD4+ T_{Reg} failed to suppress the proliferation of co-cultured CD4+CD25- responder T cells. Illustrated are the histograms of the CPD eF450 signal of the different culture setups. CD4+CD25- T_{Resp} cells to T_{Reg} 1 to 2 (A), CD4+CD25- T_{Resp} cells to T_{Reg} 1 to 0.2 (B), proliferation of T_{Resp} alone (C) and labeled T_{Resp} to unlabeled T_{Resp} 1 to 1 (D). Arrangement of histograms: left: 0 d, middle: 2 d, right: overlay of both time points. Color code of the overlay histograms: red = CPD eF450 signal at 0 d; blue = CPD eF450 signal at the day of harvest (2 d).

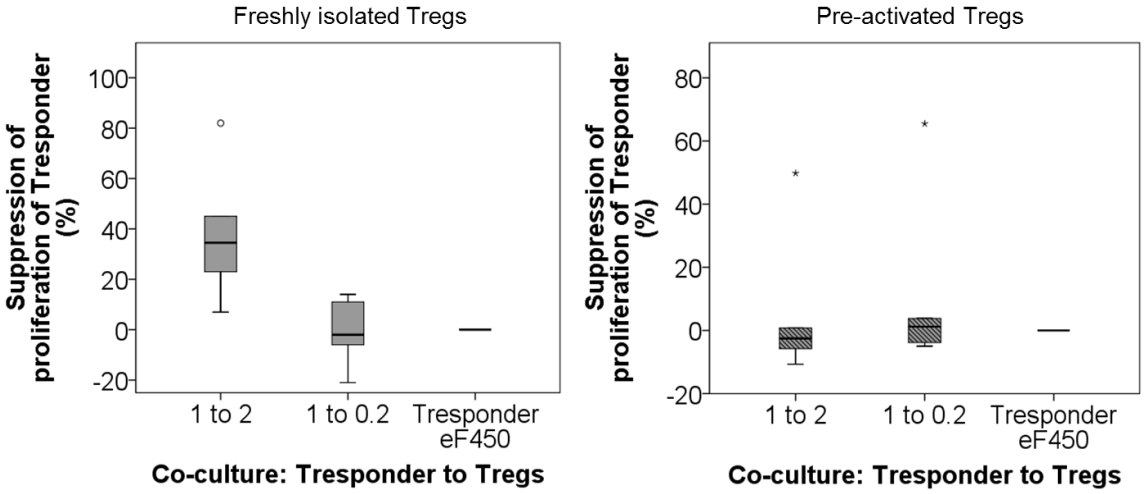

Figure 4.20: Graphical evaluation of the T_{Reg} suppression assay confirmed the successful suppression of the proliferation of CD4+CD25- responder T cells only when co-cultured with freshly isolated murine CD4+ T_{Reg}. Illustrated is the suppression of proliferation of CD4+CD25- T_{Resp} cells using freshly isolated T_{Reg} (left) or pre-activated T_{Reg} (right). Two different co-culture setups were performed: T_{Resp} to T_{Reg} 1 to 2 and T_{Resp} to T_{Reg} 1 to 0.2. T_{Resp} cells were also cultured alone (Tresponder eF450). n= 6

In figure 4.20, the graphical evaluation of the T_{Reg} suppression assays using fresh (left) and pre-activated T_{Reg} (right), respectively, is shown (n= 6). Represented is the suppression of the proliferation of T_{Resp} cells (after co-cultivation with T_{Reg}), based on the proliferation of labeled T_{Resp} cells that were cultured alone. This graphic clearly illustrates that the pre-activation of freshly isolated murine T_{Reg} correlated with a loss of their suppressive capacity in relation to the proliferation of murine CD4+CD25- T_{Resp} that were cultured alone. Based on the findings from the pre-activation culture and the T_{Reg} suppression assay, freshly isolated murine T_{Reg} were used for the following therapeutic intervention approaches *in vivo*.

4.2.1.2 Confirmation of adoptive transfer of regulatory T cells in recipient mice

Prior to starting with the experimental mice to evaluate the potential positive impact of T_{Reg} in bone healing after enrichment, the adoptive transfer of intravenously injected T_{Reg} (into the tail vein) into recipient mice was confirmed. For this analysis, depletion of regulatory T cell (DEREG) mice were used as donors [127]. In these mice, FOXP3+ T_{Reg} express an enhanced green fluorescence protein (eGFP) signal under the control of the FOXP3 gene locus. Therefore, the occurrence of T_{Reg} in the recipient C57BL/6N mice can be followed by flow cytometry due to the present GFP signal. For the adoptive transfer, T_{Reg} were isolated from spleen and lymph nodes of three DEREG donor mice via MACS. Prior to MACS seperation, a small aliquot of the pooled splenocytes and lymph node cells, respectively, and from the peripheral blood of the donor mice were taken in order to analyze the percentage of GFP+ T_{Reg} in the respective tissues (Fig. 4.21 A). Around 80–90 % of the donor T_{Reg} cells expressed a GFP signal in the respective tissues. Freshly isolated DEREG T_{Reg} were adoptively transferred into two recipient mice ($5x10^5$ cells per animal) and the transfer was checked after 24 h. In all three analyzed tissues, GFP+ T_{Reg} could be detected confirming the transfer of donor cells (blood: ~50 %; spleen: ~20 %; LN: ~10 %) (Fig. 4.21 A). In addition

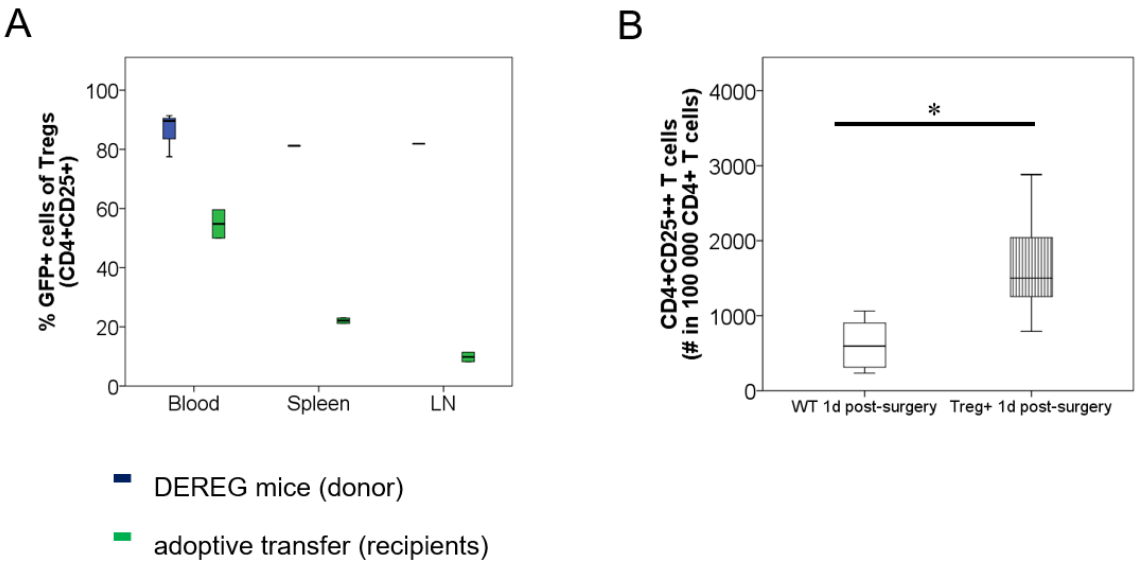

Figure 4.21: Adoptively transferred freshly isolated murine CD4+ T_{Reg} were detectable in recipient mice. DEREG mice were used as donors (FOXP3+ T_{Reg} are eGFP labeled) (A). Status of CD4+CD25++ T cells in the peripheral blood of the experimental mice 1 d post-surgery WT vs T_{Reg} enriched mice (T_{Reg}+) (B). Blue: percentage of eGFP signal in gated T_{Reg} in DEREG mice; green: percentage of eGFP+ T_{Reg} in recipient mice 24 h after adoptive transfer. The following organs were analyzed: Peripheral blood (Blood), spleen and lymph node (LN). (A) n= 1–3, (B) n= 6; *p= 0.015; Mann-Whitney U test.

to the DEREG approach, the percentage of CD4+CD25++ T cells (representing the T_{Reg} population) in the peripheral blood of mice was investigated at the following time points: 1 d post-surgery for WT mice and 1 d post-surgery for T_{Reg} enriched mice (Fig. 4.21 B). The T_{Reg} enriched mice displayed a significantly higher proportion of CD4+CD25++ T cells with regard to the WT 1 d post-surgery. This further confirms the successful adoptive transfer of T_{Reg}.

4.2.1.3 Evaluation of therapeutic potential of regulatory T cells under SPF conditions

The evaluation of the therapeutical potential of murine T_{Reg} in bone regeneration started after confirming the purity of isolated T_{Reg}, their suppressive potential and the adoptive transfer procedure (Chap. 4.2.1.1 and 4.2.1.2). From SPF housed donor mice, cells of the spleen and lymph nodes were pooled, T_{Reg} isolated and equally distributed and adoptively transferred into SPF housed recipient mice (5–7.5x10^5 T_{Reg} per mouse) (further termed: SPF T_{Reg}+). All SPF T_{Reg}+ mice showed a complete bridging (n= 6) (Fig. 4.22 A, right). In comparison, the corresponding wild type control (SPF WT, mice which were also housed under SPF conditions and which also underwent an osteotomy) was not yet completely bridged after 21 d (Fig. 4.22 A, left). The quantification of the µCT evaluation is depicted in figure 4.22 B. SPF T_{Reg}+ mice showed a higher BV (p= 0.082), BV/TV (p= 0.017) and BMD (p= 0.03) in comparison to the SPF WT mice. In conclusion, under SPF housing conditions, I could confirm that an enrichment of T_{Reg} prior to surgery leads to a significantly better healing outcome in our non-critical size defect mouse osteotomy model when compared to an untreated but also fractured control group.

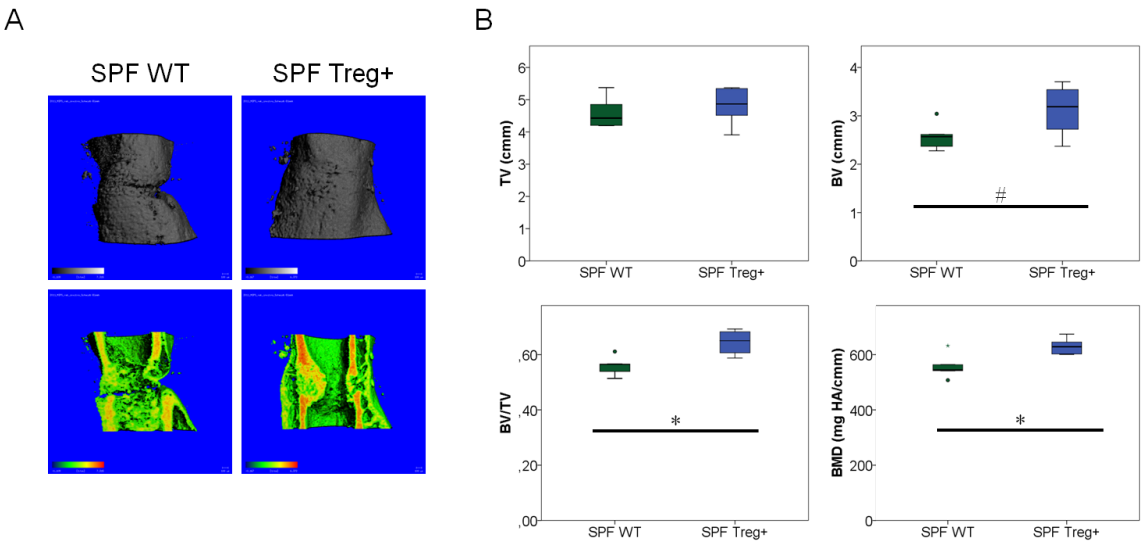

Figure 4.22: Adoptive transfer of T_{Reg} in SPF housed mice improved the healing outcome after 21 d, µCT evaluation. In A, representative images of the analyzed volume of interest of the healing bones are shown. T_{Reg} enriched mice showed complete bridging after 21 d (A, right, SPF T_{Reg}+), whereas the control group did not completely heal after 3 weeks (A, left, SPF WT). In the two lower pictures, the 3D images of the healing bones are cut sagittally/frontally to demonstrate the progress of the remodeling process. The color code indicates the mineralization state, with an increasing mineralization from black to white and blue to red, respectively. The quantification of the µCT data revealed a significantly higher BV/TV and BMD (B). TV= total volume, BV= bone volume, BV/TV= ratio of BV to TV, BMD= bone mineral density. *p= 0.017 (BV/TV), *p= 0.03 (BMD), #p= 0.082; n= 5–6; Mann-Whitney U test.

4.2.1.4 Changes in the murine immune system under SPF and semi-sterile housing conditions

Using SPF housed mice, I could confirm the therapeutic potential of freshly isolated murine T_{Reg} to improve bone fracture healing when adoptively transferred prior to surgery (Chap. 4.2.1.3). SPF housed animals are kept in a specific pathogen free environment. Therefore, the immune system of these animals is less experienced in comparison to animals kept under non-SPF conditions. Even more relevant, the immune system of these SPF housed animals is less experienced with regard to the patient situation in the clinic. In order to have a clinically more relevant situation, the positive potential of T_{Reg} enrichment prior to osteotomy was analyzed under non-SPF housing conditions of the experimental mice.
Before repeating the adoptive transfer experiments, I investigated the changes of the murine immune system due to the different housing conditions without creating an osteotomy in these animals. The immune cell composition of differently housed mice was evaluated in the peripheral blood, the spleen and the bone marrow by flow cytometry.
For CD4+ and CD8+ T cells, there were no differences detectable in animals kept under different housing conditions for all three analyzed tissues (Fig. 4.23 A). In contrast, the percentage of CD4+CD25+ and CD8+CD25+ T cells was significantly higher in the semi-sterile mice compared to SPF housed mice (p= 0.016) (Fig. 4.23 B).

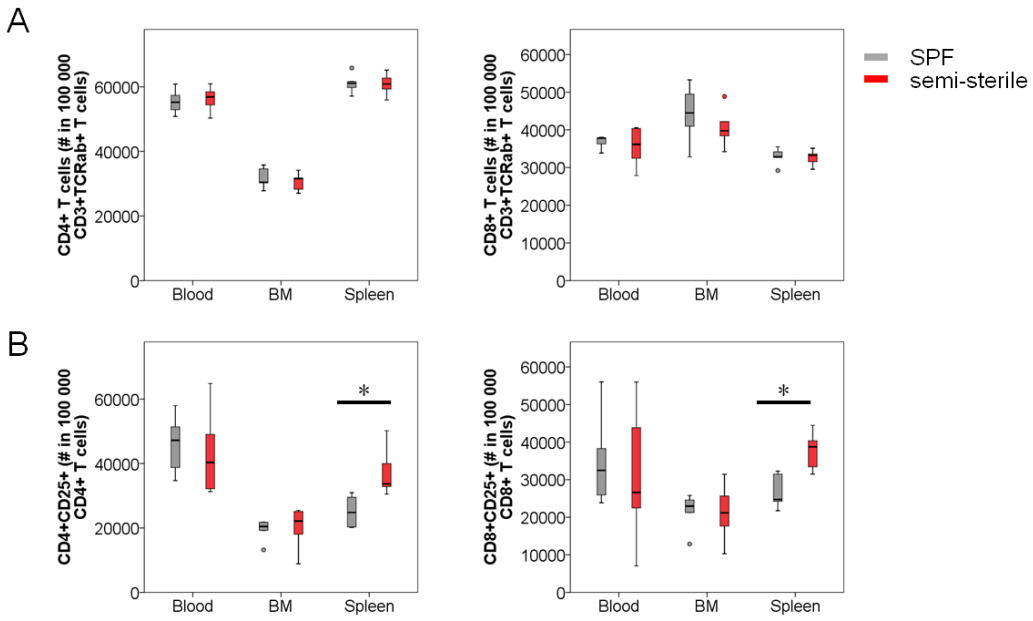

Figure 4.23: Semi-sterile housing led to an increase of CD4+CD25+ and CD8+CD25+ T cells in comparison to SPF housed mice. CD4+ and CD8+ T cell distribution in SPF and semi-sterile housed mice. Percentage of CD4+ and CD8+ T cells in blood, bone marrow and spleen (A), percentage of CD4+CD25+ and CD8+CD25+ T cells (activated T cells and T_{Reg}) in all three organs (B). CD4+ and CD8+ T cells were calculated on the basis of gated CD3+/TCRαβ+ T cells and CD25+ T cells on the basis of gated CD4+ and CD8+ T cells. grey: SPF housing, red: semi-sterile housing, *p= 0.016, n= 5–6; Mann-Whitney U test.

The population of effector, effector memory and central memory T cells was also investigated (Fig. 4.24 and 4.25). The marker CD44 was further included into this and the following analyses, in order to distinguish more precisely between naïve and memory T cells (naïve: CD44-; memory: CD44+). The three subpopulations were gated as follows: effector T cells: CD4+ or CD8+/CD44+/CD62L-/CD25+ (T_{EF}); effector memory T cells: CD4+ or CD8+/CD44+/CD62L-/CD25- (T_{EFM}) and central memory T cells: CD4+ or CD8+/CD44+/CD62L+ (T_{CM}).
Semi-sterile housed mice displayed a higher percentage of CD4+ T effector cells in the spleen (p= 0.052) when compared to the WT group (Fig. 4.24 A). The proportion of CD4+ effector memory T cells was higher in the SPF mice in comparison to the semi-sterile animals (p= 0.032) (A, B). The CD4+ central memory T cells displayed a lower percentage in the semi-sterile mice vs. the SPF animals in the spleen (p= 0.095). Regarding the CD8+ splenocyte population, semi-sterile housed mice possess a significantly higher percentage of T effector cells (p= 0.008) (Fig. 4.25 A). The proportion of central memory CD8+ T cells was significantly lower in the spleen in the semi-sterile mice vs. SPF mice (p= 0.016) (Fig. 4.25 B). Further, I investigated the population of T_{Reg} in all three analyzed tissues. Interestingly, in the bone marrow, a significantly higher proportion of CD4+ T_{Reg} was found in the semi-sterile animals with regard to the SPF mice (p= 0.03) (Fig. 4.26). The blood and the spleen showed an equal distribution of T_{Reg} between both housing conditions.

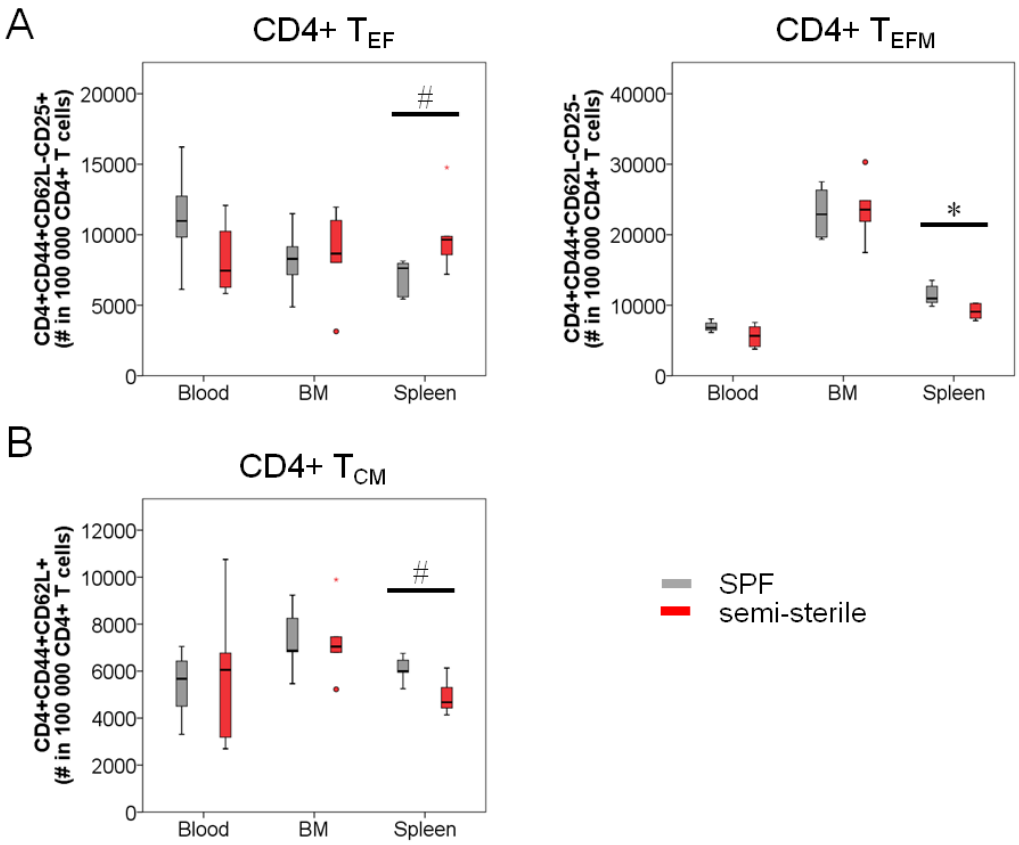

Figure 4.24: Semi-sterile housing led to changing proportions of CD4+ effector, effector memory and central memory T cells in comparison to SPF housed mice. CD4+ effector, effector memory and central memory T cell distribution in SPF and semi-sterile housed mice. Flow cytometry anylsis of the percentage of CD4+ T effector (T_{EF}) and T effector memory T cells (T_{EFM}) (A), percentage of CD4+ central memory T cells (T_{CM}) (B) in blood, bone marrow and spleen. Cells were calculated on the basis of gated CD3+/TCR$\alpha\beta$+/CD4+ T cells. grey: SPF housing, red: semi-sterile housing, *p= 0.032, #p= 0.056 (A), #p= 0.095 (B), n= 5–6; Mann-Whitney U test.

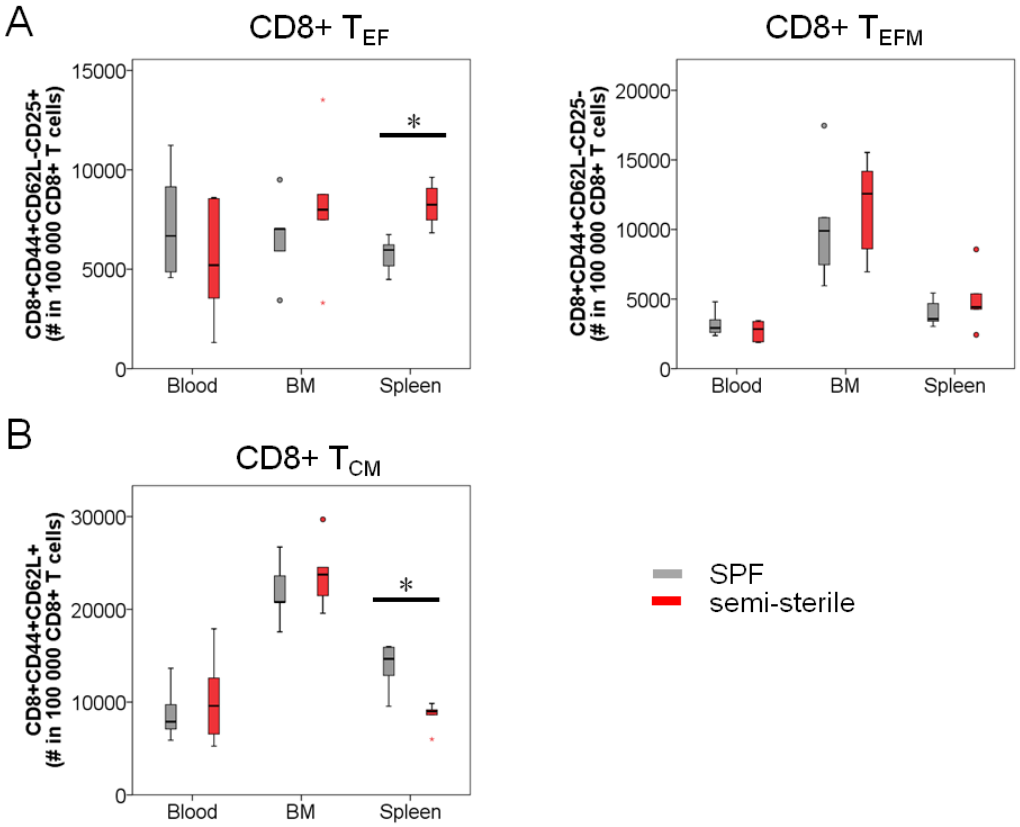

Figure 4.25: Semi-sterile housing led to changing proportions of CD8+ effector, effector memory and central memory T cells in comparison to SPF housed mice. CD8+ effector, effector memory and central memory T cell distribution in SPF and semi-sterile housed mice. Flow cytometry analysis of the percentage of CD8+ T effector (T_{EF}) and T effector memory T cells (T_{EFM}) (A), percentage of CD8+ central memory T cells (T_{CM}) (B) in blood, bone marrow and spleen. Cells were calculated on the basis of gated CD3+/TCRαβ+/CD8+ T cells. grey: SPF housing, red: semi-sterile housing, *p= 0.008 (T_{EF}) (A), *p= 0.016 (B), n= 5–6; Mann-Whitney U test.

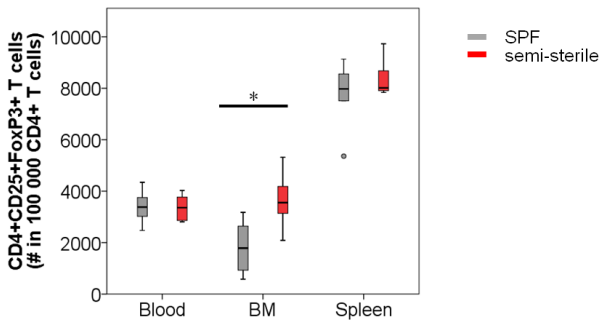

Figure 4.26: Semi-sterile housing led to an increase of CD4+ T_{Reg} in comparison to SPF housed mice. CD4+ T_{Reg} cell distribution in SPF and semi-sterile housed mice. Percentage of CD4+ T_{Reg} in blood, bone marrow and spleen. CD4+ T_{Reg} were calculated on the basis of gated CD3+/CD4+ T cells. grey: SPF housing, red: semi-sterile housing, *p= 0.03; n= 6; Mann-Whitney U test.

4.2.1.5 Evaluation of the healing outcome after enrichment of regulatory T cells under semi-sterile conditions

The housing of the experimental mice in a semi-sterile environment effectively influenced the immune cell composition in these animals towards a higher experienced immune status (Chap. 4.2.1.4). For a clinically more relevant approach, I repeated the evaluation of the healing outcome after adoptive T_{Reg} transfer, this time using donor and recipient mice housed in a semi-sterile environment.
A controversial picture was observed regarding the healing outcome of the T_{Reg} enriched mice (Fig. 4.27, T_{Reg}+). Four of the eight operated mice showed a significantly better healing and the other four a significantly less good healing compared to the WT group (Fig. 4.27 and 4.28 B). In figure 4.27, representative μCT images of the healing bones after 21 d are presented. As comparison, the images from the SPF approach were also included into the figure. Regarding the slightly better healing outcome of SPF WT in comparison to the WT mice, it already demonstrated the improved healing outcome under SPF housing, already implicating the partial negative impact of the adaptive immune system in fracture repair [12]. But also between the good healer of the T_{Reg}+ mice (Fig. 4.27, T_{Reg}+ left) and the SPF T_{Reg}+ animals, it seemed that the SPF T_{Reg}+ displayed a more progressed remodeling of the fracture area, following the cut μCT images (Fig. 4.27, lower picture). Regarding the T_{Reg}+ animals as one group, without dividing between good and bad healing mice, no differences in the quantification of the μCT results were observed with regard to the WT control group (Fig. 4.28 A). After separating the different healing outcome of the T_{Reg} enriched mice into two groups (good healer: T_{Reg}+ good; bad healer: T_{Reg}+ bad), a better healing of the T_{Reg}+ good mice could be observed in comparison to the WT which was even significant for TV and BV (Fig. 4.28 B; $p = 0.01$ (TV and BV), $p = 0.038$ (BV/TV)). T_{Reg}+ bad mice revealed a significantly poorer healing outcome vs. the WT animals (Fig. 4.28 B; $p = 0.01$ (TV and BV)). Therefore, a better healing outcome was detected for all four analyzed parameters in the T_{Reg}+ good with regard to the T_{Reg}+ bad mice ($p = 0.029$). Histomorphometrical analysis confirmed the observed differences in the healing outcome between the T_{Reg}+ good and T_{Reg}+ bad mice (Fig. 4.30). In figure 4.29, representative Movat Pentachrome pictures are shown, illustrating the complete bridging in the T_{Reg}+ good group and the sealed medullary canal of the non-bridging in the T_{Reg}+ bad healing group. Although the bone parameters were not significantly different between the WT and the two T_{Reg}+ groups, the graphs clearly support the observed findings of the μCT. The content of connective tissue in the analyzed area was increased in the T_{Reg}+ bad mice with regard to the WT mice ($p = 0.029$). This is a clear indication for the non-bridging of these T_{Reg} enriched mice characterized by an accumulation of connective tissue between the closed fracture ends. The cartilage fraction was higher in WT animals vs. the T_{Reg}+ bad and T_{Reg}+ good mice ($p = 0.029$ (T_{Reg}+ bad), $p = 0.057$ (T_{Reg}+ good)).

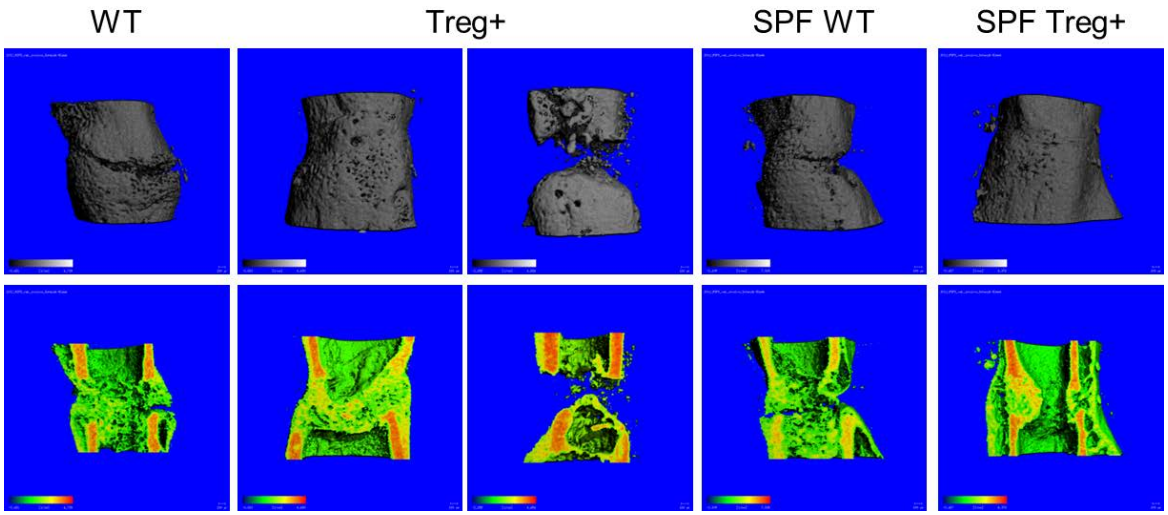

Figure 4.27: Adoptive transfer of CD4+ murine T_{Reg} in semi-sterile housed mice led to a controversial healing outcome after 21 d, µCT evaluation. Representative images of the analyzed volume of interest of the healing bones are shown. WT mice, housed in a semi-sterile environment, showed no complete bridging after 21 d (left, WT). In contrast, T_{Reg} enriched animals under semi-sterile housing conditions displayed a controversial healing outcome: four mice showed complete bridging (T_{Reg}+ left), wheras four mice showed no bridging (T_{Reg}+ right). µCT images from the corresponding groups under SPF conditions are also depicted as comparison (SPF WT and SPF T_{Reg}+). In the lower pictures, the 3D images of the healing bones are cut sagittally/frontally to demonstrate the progress of the remodeling process. The color code indicates the mineralization state, with an increasing mineralization from black to white and blue to red, respectively. n= 4–6

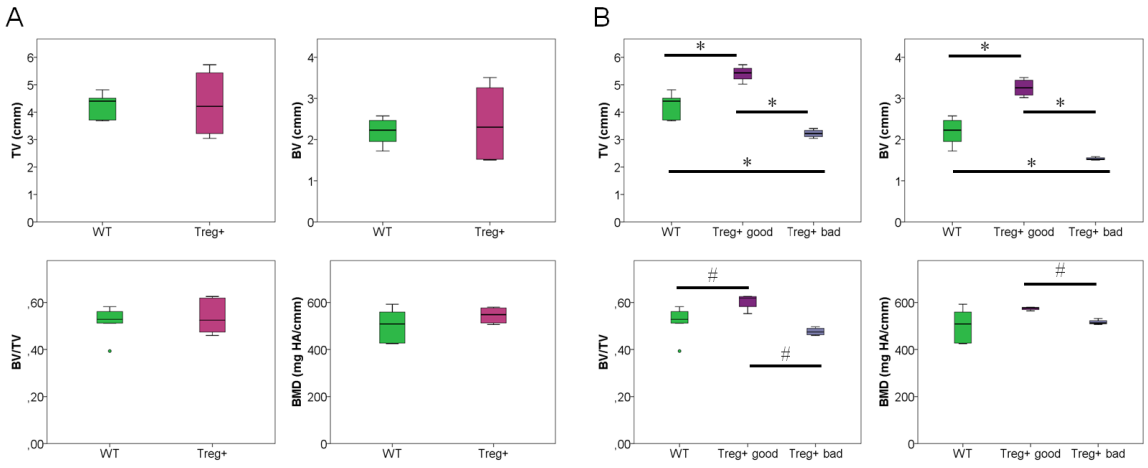

Figure 4.28: Adoptive transfer of CD4+ murine T_{Reg} in semi-sterile housed mice led to a controversial healing outcome after 21 d, µCT quantification. The healing outcome of the T_{Reg} enriched mice (T_{Reg}+) revealed a controversial healing outcome. Regarding the T_{Reg}+ animals as one group, no differences were observed vs. the WT control (A). Separating the good and bad healing T_{Reg}+ mice, T_{Reg}+ good displayed a significant better and the T_{Reg}+ bad a significant poorer healing outcome with regard to the WT (B). TV= total volume, BV= bone volume, BV/TV= ratio of BV to TV, BMD= bone mineral density. *p=0.01–0.029, #p= 0.029–0.038; n= 4–6; Mann-Whitney U test, Bonferroni correction.

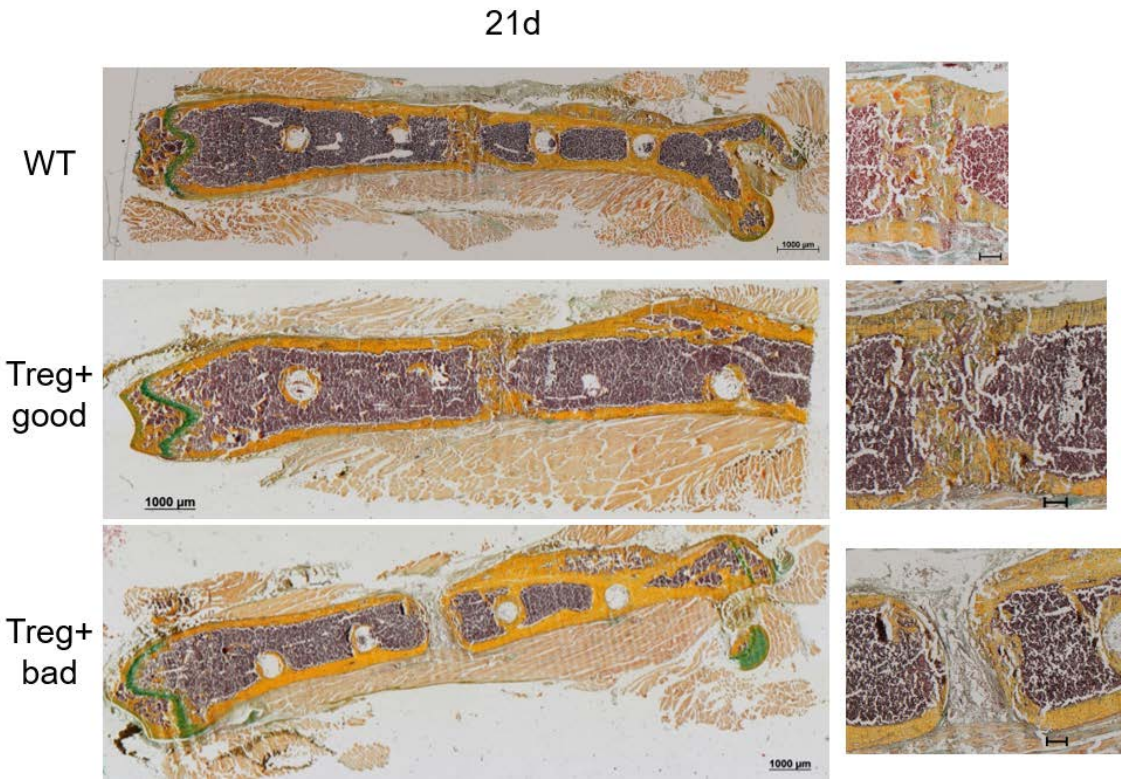

Figure 4.29: Movat Pentachrome stainings confirmed the controversial healing outcome observed after 21 d after adoptive T_{Reg} transfer in semi-sterile housed mice. Movat Pentachrome stainings of regenerating murine femora of WT, T_{Reg}+ good and T_{Reg}+ bad mice after 21 d. Representative images of each group are shown, on the left as the total femur, on the right as a magnification of the gap area. Coloration of the following tissues: mineralized bone and cartilage= yellow, cartilage= blue/green, connective tissue= bluish, bone marrow= purple and cell nuclei= black. Error bars of the magnifications: 200 µm.

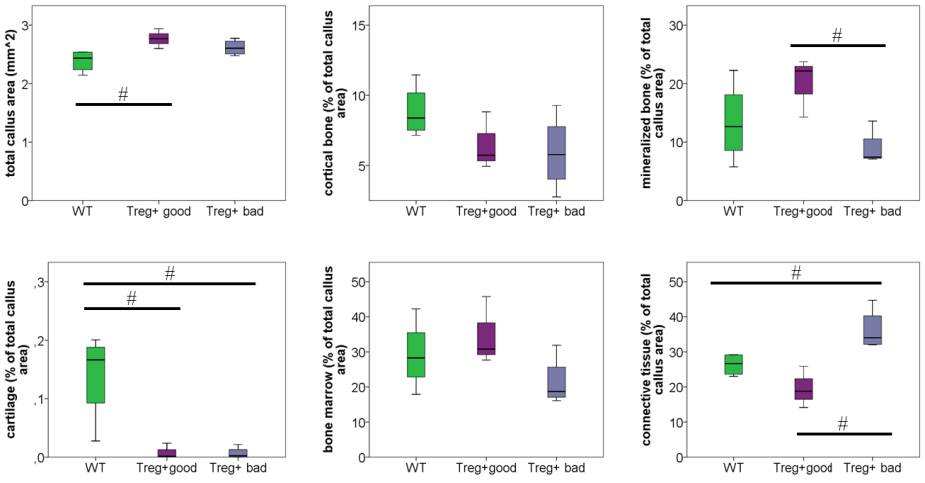

Figure 4.30: Histomorphometrical analysis of the tissue distribution confirmed the controversial healing outcome observed after 21 d after adoptive T_{Reg} transfer in semi-sterile housed mice. Based on Movat Pentachrome stainings done on tissue cryo-sections from WT and T_{Reg} enriched mice, the distribution of different tissue types within the fracture area was evaluated. n= 3–4; #p= 0.029–0.057; Mann-Whitney U test, Bonferroni correction.

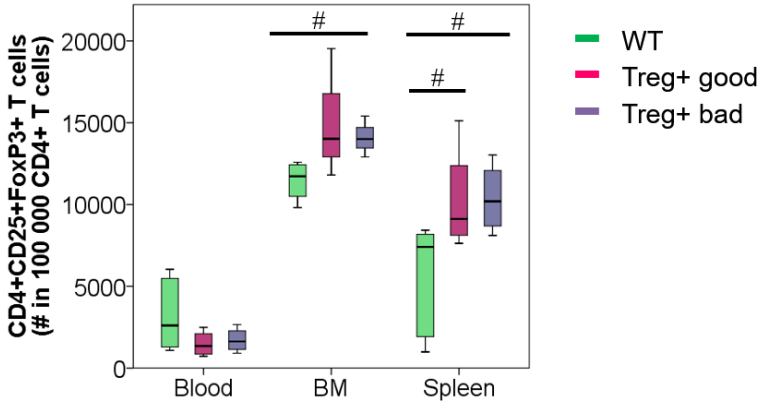

Figure 4.31: Adoptively transferred T_{Reg} were still detectable after 21 d in the semi-sterile housed mice, independent from the healing outcome. CD4+ T_{Reg} cell distribution in WT and T_{Reg} enriched mice kept under semi-sterile housing conditions after 21 d. Percentage of CD4+ T_{Reg} in blood, bone marrow and spleen. CD4+ T_{Reg} were calculated on the basis of gated CD3+/CD4+ T cells. green: WT, pink: T_{Reg}+ good healer, purple: T_{Reg}+ bad healer, #p= 0.038–0.057; n= 3–6; Mann-Whitney U test, Bonferroni correction.

One reasonable explanation for the observed controversial healing outcome could be an unsuccessful adoptive transfer of T_{Reg} prior to osteotomy. Therefore, the percentage of T_{Reg} was analyzed 21 days post-sugery in the adoptively transferred mice (Fig. 4.31). For both T_{Reg} enriched groups (good and bad healer) a higher proportion of T_{Reg} was detected in the spleen and bone marrow in comparison to the control WT group even after 21 d (bone marrow: p= 0.057, spleen: p= 0.038). However, between both healing groups of the T_{Reg} enriched mice, no differences in the percentage were detectable. Furthermore, also the populations of total CD4+ and CD8+ T cells and their effector/effector memory and central memory subsets were evaluated 21 d after surgery by flow cytometry. The total population of CD4+ and CD8+ T cells was relative equal between the three groups in all three evaluated tissues (Fig. 4.32 A). The highest percentage of CD4+ T cells was found in the spleen and the lowest in the bone marrow. For the CD8+ T cell subset, the highest percentage was detected in the blood and a relative equal proportion in bone marrow and spleen. For CD4+CD25+ and CD8+CD25+ T cells, the T_{Reg} enriched mice displayed a higher percentage in all three tissue types, independent of the healing outcome (Fig. 4.32 B). Between both T_{Reg} enriched groups, there was even a significantly higher proportion of the CD8+CD25+ T cells in the T_{Reg}+ bad animals vs. the T_{Reg}+ good healer in the blood (p= 0.01) (CD4+CD25+: p= 0.029). Between the WT and the T_{Reg}+ bad mice, the differences for both, CD4+CD25+ and CD8+CD25+ T cells, were either significant (indicated by *) or a trend (indicated by #) in all three evaluated tissues (CD4+CD25+: p= 0.01 (blood), p= 0.057 (bm), p= 0.01 (spleen); CD8+CD25+: p= 0.01 (blood), p= 0.057 (bm), p= 0.01 (spleen)). For the WT and the good healing T_{Reg} enriched mice, differences in the percentage of CD4+CD25+ and CD8+CD25+ T cells, respectively, were significant in the spleen (CD4+CD25+, p= 0.01; CD8+CD25+, p= 0.019) and blood (p= 0.038).

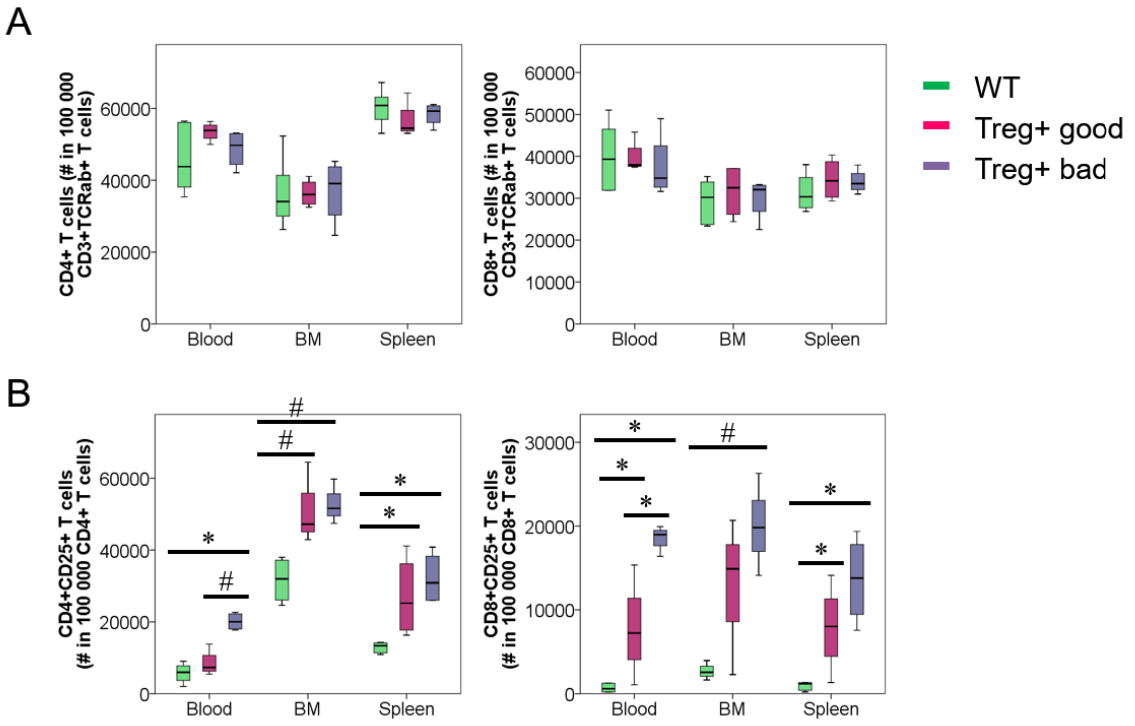

Figure 4.32: WT and T_{Reg} enriched mice showed different expression pattern of CD4+CD25+ and CD8+CD25+ T cells after 21 d under semi-sterile housing conditions. Percentage of CD4+ and CD8+ T cells in blood, bone marrow and spleen (A), percentage of CD4+CD25+ and CD8+CD25+ T cells (activated T cells and T_{Reg}) in all three organs (B). CD4+ and CD8+ T cells were calculated on the basis of gated CD3+/TCRαβ+ T cells and CD25+ T cells on the basis of gated CD4+ and CD8+ T cells. green: WT, pink: T_{Reg}+ good healer, purple: T_{Reg}+ bad healer; *p= 0.01–0.038; #p= 0.029–0.057, n= 4–6

The systemic distribution of CD4+ and CD8+ T effector, effector memory and central memory T cells was further analyzed in peripheral blood, bone marrow and spleen. For this analysis, only two of the six WT animals could be included into the evaluation. During my thesis, we decided to modify the antibody panel for this staining by including the surface marker CD44. This enabled me to distinguish more precisely between the naïve (CD44-) and memory (CD44+) T cell subpopulations. However, four of the six WT animals had already been operated and sacrificed and thus also measured by flow cytometry before modifying the staining panel. Therefore, WT 1–4 were not included into the analysis of the T_{EF}/T_{EFM}/T_{CM} pool of CD4+ and CD8+ cells. In the CD4+ T_{EF} subset, the WT was higher in all three tissues (Fig. 4.33 A). In addition, the T_{Reg}+ bad mice displayed a higher proportion in the blood and bone marrow vs. the T_{Reg}+ good mice (p= 0.029). The same picture was seen in the CD8+ T_{EF} cells (p= 0.057). The CD4+ T_{EFM} subpopulation was relatively equal distributed between the three groups in all three organs, showing the highest percentage again in the bone marrow. A similar picture was seen in the corresponding CD8+ T cells, whereas the WT displayed a slightly higher percentage in the blood and spleen in comparison to the T_{Reg} enriched mice. For the central memory cells of both T cell subsets, the T_{Reg}+ bad animals possessed a higher proportion in the bone marrow and spleen with regard to the T_{Reg}+ good mice (CD8+ T_{CM}: p= 0.029) (Fig. 4.33 B; 4.34 B).

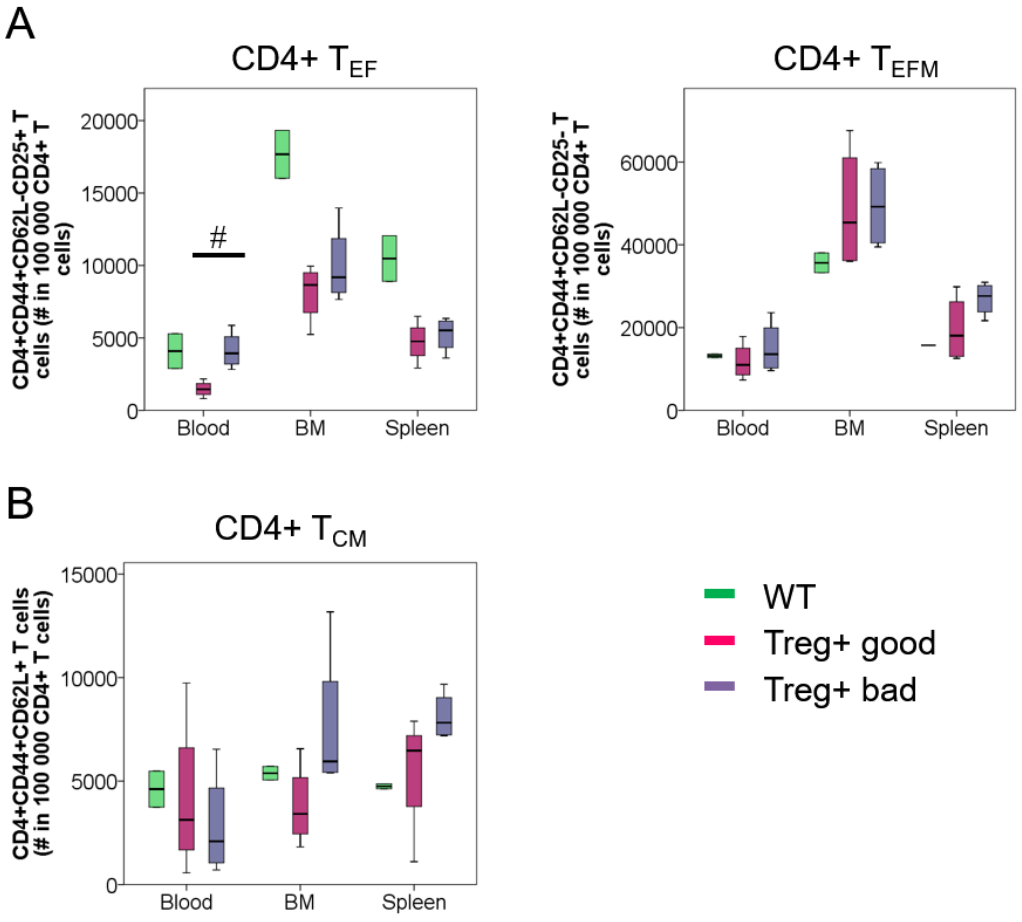

Figure 4.33: T_{Reg} enriched mice with a less good healing outcome had a higher proportion of CD4+ effector T cells in comparison to the good healing animals 21 d post-surgery. CD4+ effector, effector memory and central memory T cell distribution in WT and T_{Reg} enriched mice kept under semi-sterile housing conditions. Flow cytometry analysis of the percentage of CD4+ T effector (T_{EF}) and T effector memory T cells (T_{EFM}) (A), percentage of CD4+ central memory T cells (T_{CM}) (B) in blood, bone marrow and spleen. Cells were calculated on the basis of gated CD3+/TCRαβ+/CD4+ T cells. green: WT, pink: T_{Reg}+ good healer, purple: T_{Reg}+ bad healer, #p= 0.029; n= 2–4; Mann-Whitney U test, Bonferroni correction.

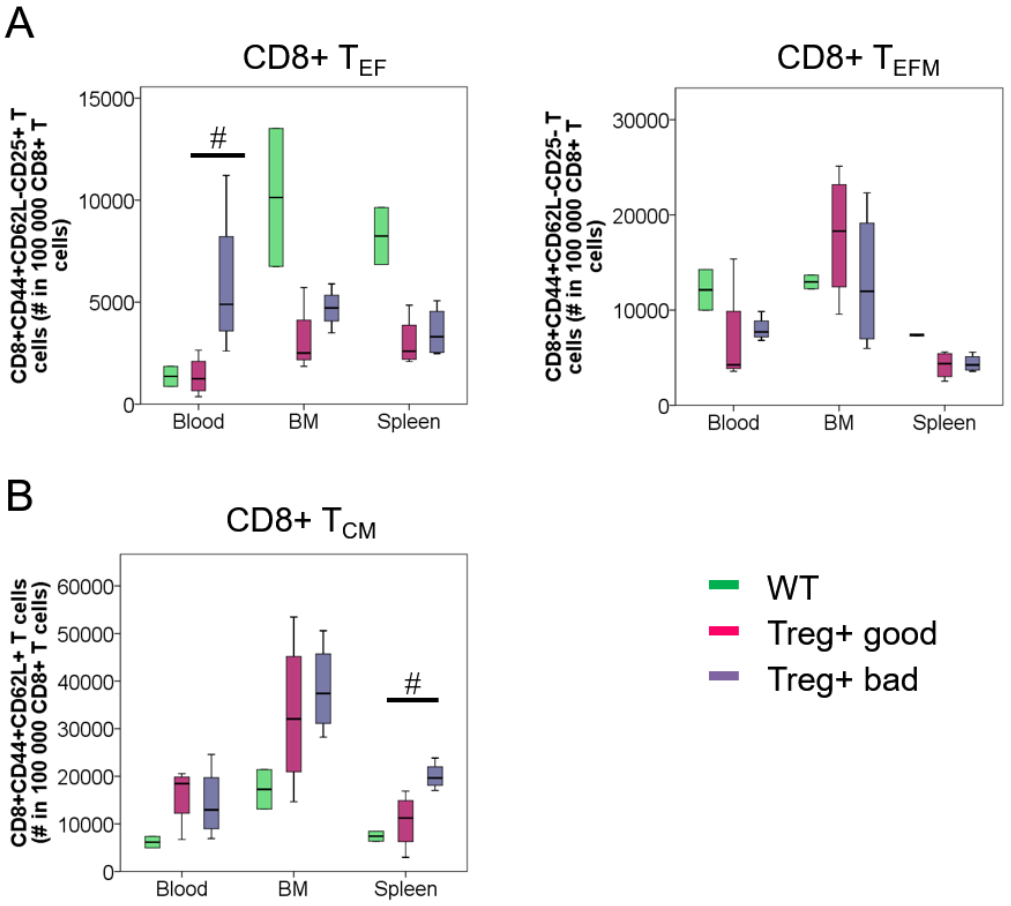

Figure 4.34: T_{Reg} enriched mice with a less good healing outcome had a higher proportion of CD8+ effector T cells in comparison to the good healing animals 21 d post-surgery. CD8+ effector, effector memory and central memory T cell distribution in WT and T_{Reg} enriched mice kept under semi-sterile housing conditions. Flow cytometry analysis of the percentage of CD8+ T effector (T_{EF}) and T effector memory T cells (T_{EFM}) (A), percentage of CD8+ central memory T cells (T_{CM}) (B) in blood, bone marrow and spleen. Cells were calculated on the basis of gated CD3+/TCRαβ+/CD8+ T cells. green: WT, pink: T_{Reg}+ good healer, purple: T_{Reg}+ bad healer, #p= 0.029; n= 2–4; Mann-Whitney U test, Bonferroni correction.

4.2.2 Therapeutic intervention: CD25+ T cell depletion prior to surgery

The approach of the CD25+ T cell depletion prior to surgery was carried out in order to evaluate the healing outcome after 21 d when T_{Reg} were absent at the moment of setting the osteotomy. T_{Reg} are characterized by the expression of the surface marker CD25. Several studies already reported a successful depletion of T_{Reg} by an anti-CD25 antibody [128, 129, 130]. Thus, a specific monoclonal α-CD25 antibody was injected intraperitoneally into semi-sterile housed mice for four consecutive injections, starting 3 days prior to osteotomy (Fig. 4.35). The healing outcome was investigated after 21 d by μCT and histomorphometry.
Before starting the experiment, the depletion of CD4+CD25+ T cells was confirmed (p= 0.008) (Fig. 4.36).

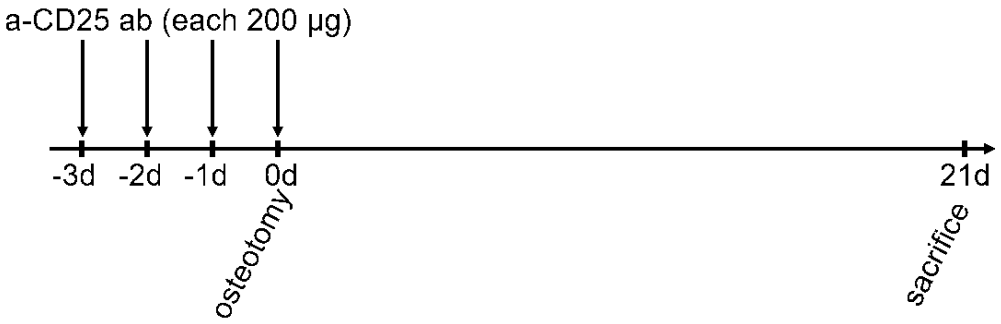

Figure 4.35: Scheme of the experimental design of CD25+ T cell depletion. A monoclonal α-CD25 antibody was injected for four consecutive injections (intraperitoneal), starting 3 days prior to surgery (-3 d). The healing outcome was evaluated after 21 days. ab= antibody

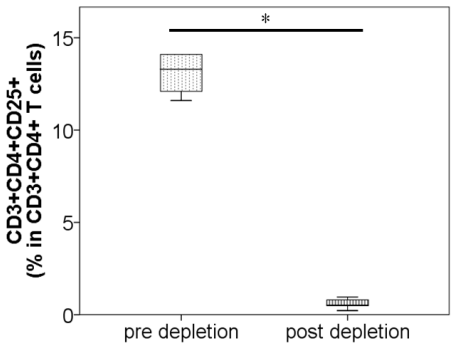

Figure 4.36: Confirmation of the depletion of CD25+ T cells. CD25+ T cells were depleted by four consecutive injections of a monoclonal α-CD25 antibody. From depleted mice, blood samples were taken pre- and post-depletion, respectively. The percentage of CD4+CD25+ T cells was investigated by flow cytometry based on the population of CD3+CD4+ T cells. *p= 0.008; n= 5

Afterwards, the experimental mice were depleted and operated (further termed: CD25-). After 21 d, the healing outcome was evaluated by µCT measurements (Fig. 4.37). In comparison to the WT control group, no differences were observed in the CD25- mice by µCT. This was also confirmed by the quantification of the µCT results (Fig. 4.37 B). The histomorphometrical analysis of Movat Pentachrome stained cryo-sections confirmed the picture of the healing outcome already observed by µCT (Fig. 4.39). In figure 4.38, representative images of the Movat Pentachrome stained sections are displayed. A slight increase of the proportion of mineralized bone was observed in the depleted animals with regard to the WT. The presence of cartilage in the evaluated fracture area showed also a higher proportion in the CD25- vs. the WT, however, again without being significant. In addition to the µCT measurement and histomorphometrical analysis, flow cytometry analyses were done 2 days post-surgery. The depletion of T_{Reg} was confirmed for all three investigated tissues (Fig. 4.40). In accordance with the former flow cytometry analyses, the proportion of effector and memory T cells were also investigated. The populations of CD4+ and CD8+ effector T cells decreased or were even absent (Fig. 4.41). A clear decrease was also observed for the effector memory T cell subpopulation after depletion (Fig. 4.42). Statistical significances were not determined due to the small sample size of n= 3 for each mice group.

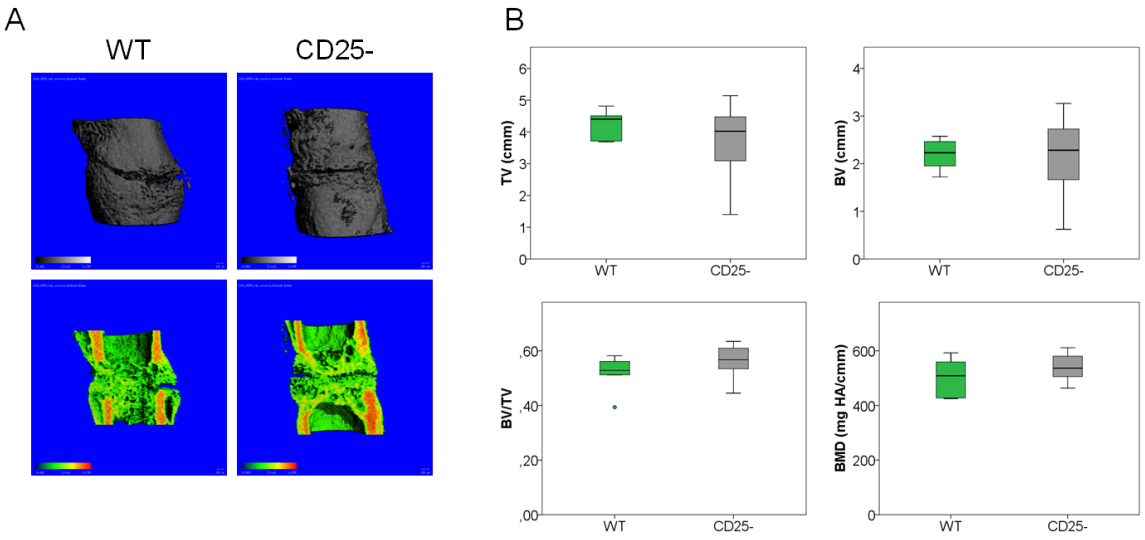

Figure 4.37: CD25+ T cell depletion did not lead to a changing healing outcome after 21 d in comparison to the WT. µCT evaluation of the healing outcome after CD25+ T cell depletion under semi-sterile conditions 21 d post-surgery. In A, representative images of the analyzed volume of interest of the healing bones are shown (WT control group vs. CD25- mice). For both groups, no complete bridging of the fractured bone was achieved after 21 d. In the two lower pictures, the 3D images of the healing bones are cut sagittally/frontally to demonstrate the progress of the remodeling process. The color code indicates the mineralization state, with an increasing mineralization from black to white and blue to red, respectively. Quantification of the µCT data revealed no differences between both groups (B). TV= total volume, BV= bone volume, BV/TV= ratio of BV to TV, BMD= bone mineral density. n= 6

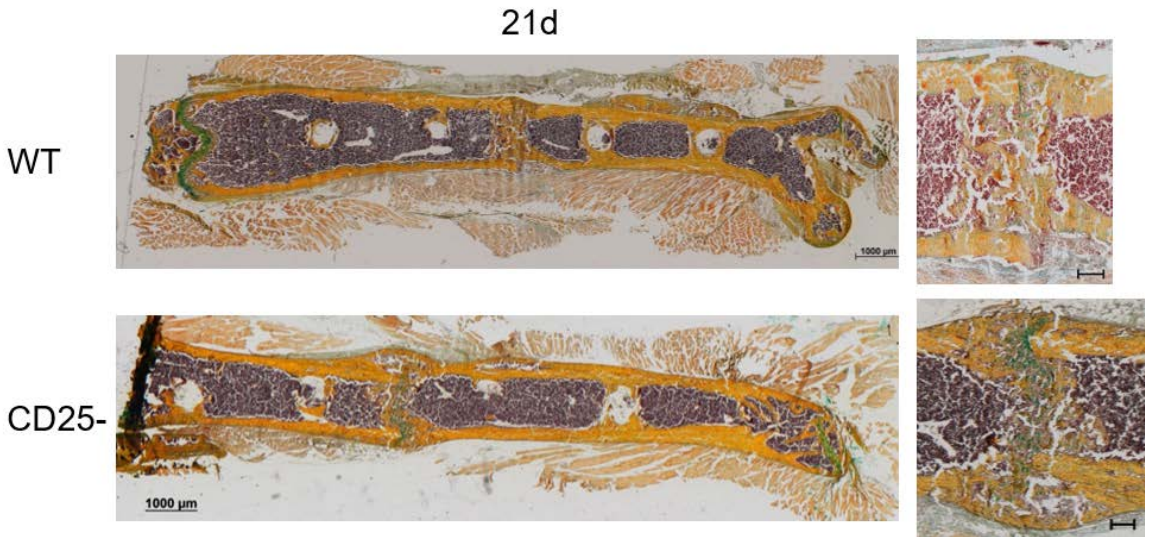

Figure 4.38: Movat Pentachrome stainings confirmed the unchanged healing outcome in the CD25+ T cell depleted animals after 21 d in comparison to the WT. Movat Pentachrome stainings of regenerating murine femora of WT and CD25- mice after 21 d. Representative images of each group are shown, on the left as the total femur, on the right as a magnification of the gap area. Coloration of the following tissues: mineralized bone and cartilage= yellow, hypertrophic cartilage= blue/green, connective tissue= bluish, bone marrow= purple and cell nuclei= black. Error bars of the magnifications: 200 µm.

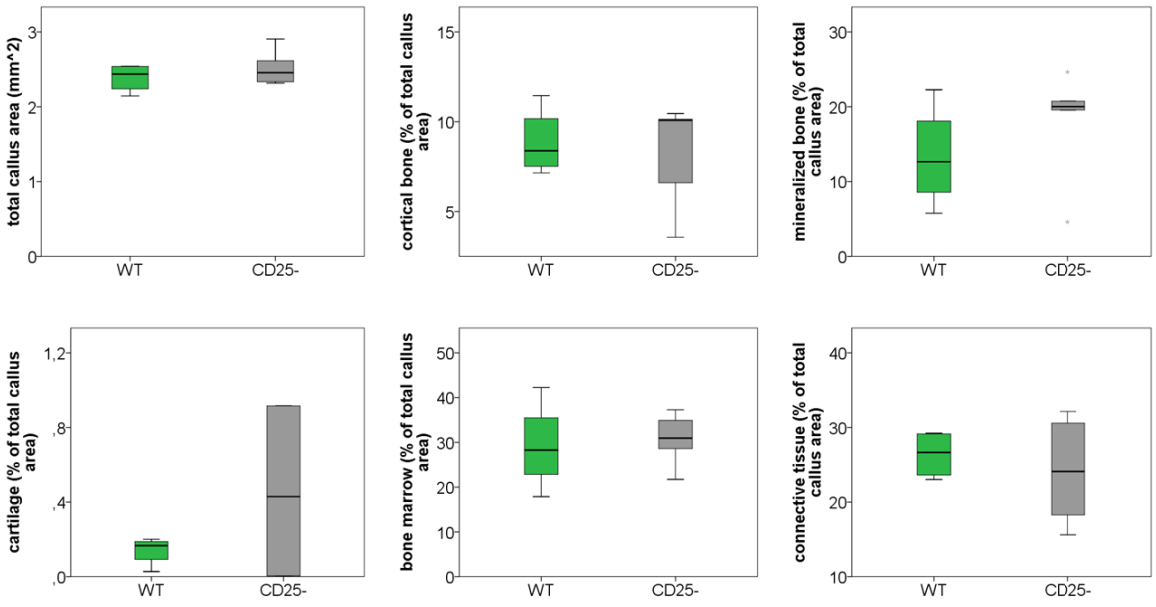

Figure 4.39: Histomorphometrical analysis of the tissue distribution confirmed the unchanged healing outcome in the CD25+ T cell depleted animals after 21 d in comparison to the WT. Based on Movat Pentachrome stainings performed on tissue cryo-sections from WT and CD25+ T cell depleted mice; the distribution of different tissue types within the fracture area was evaluated. n= 4-6

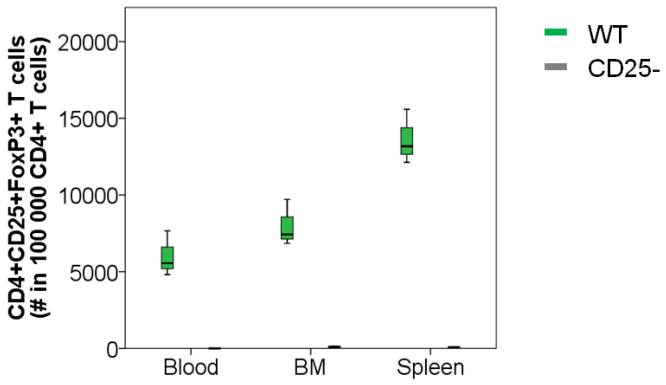

Figure 4.40: CD4+ T_{Reg} depletion was confirmed in the CD25+ T cell depleted mice 2 d post-surgery. CD4+ T_{Reg} cell distribution in WT and CD25- mice kept under semi-sterile housed conditions 2 d post-surgery. Flow cytometry analysis in blood, bone marrow and spleen. CD4+ T_{Reg} were calculated on the basis of gated CD3+/CD4+ T cells. green: WT, grey: CD25-. n= 3

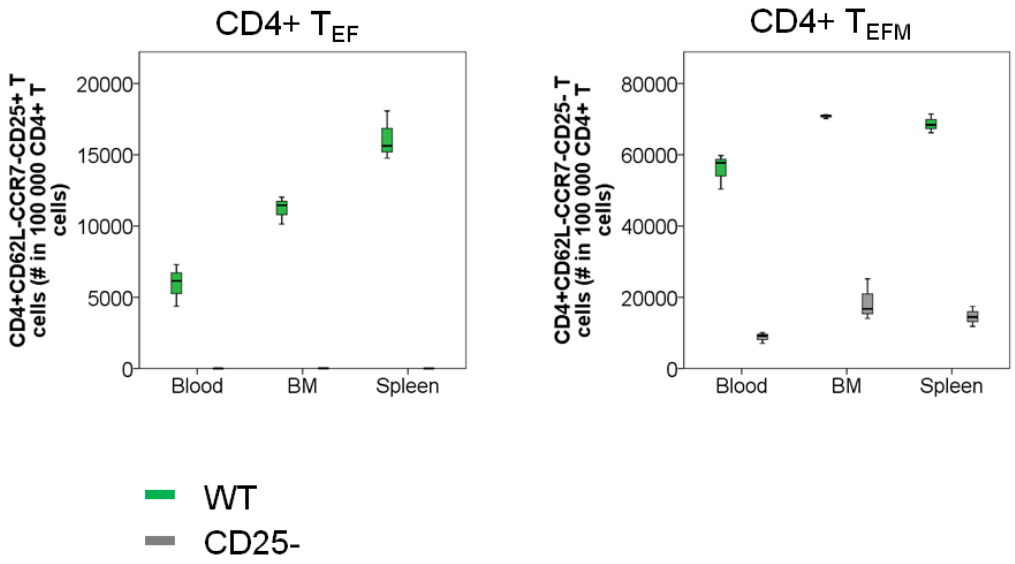

Figure 4.41: CD4+ effector and effector memory T cell depletion was confirmed in the CD25+ T cell depleted mice 2 d post-surgery. CD4+ effector and effector memory T cell distribution in WT and CD25- mice kept under semi-sterile housing conditions 2 d post-surgery. Flow cytometry analysis in blood, bone marrow and spleen. Cells were calculated on the basis of gated CD3+/TCRαβ+/CD4+ T cells. green: WT, grey: CD25-; n= 3

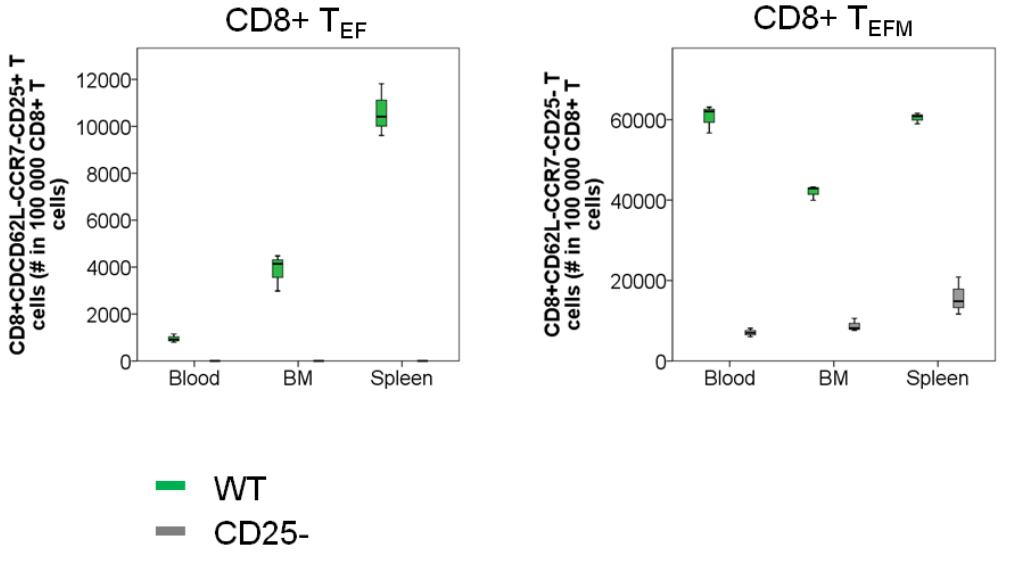

Figure 4.42: CD8+ effector and effector memory T cell depletion was confirmed in the CD25+ T cell depleted mice 2 d post-surgery. CD8+ effector and effector memory T cell distribution in WT and CD25- mice kept under semi-sterile housing conditions 2 d post-surgery. Flow cytometry analysis in blood, bone marrow and spleen. Cells were calculated on the basis of gated CD3+/TCRαβ+/CD8+ T cells. green: WT, grey: CD25-; n= 3

4.3 Proof of concept approach: Prediction prior to surgery of potential good and bad healer based on "immune balance"

Under 4.2, the impact of the adaptive immune system in fracture healing especially in mice housed in a semi-sterile environment was investigated. A semi-sterile housing led to a measurable activation of the adaptive immunity in comparison to housing under SPF conditions: increasing percentage of CD4+CD25+, CD8+CD25+, CD4+ and CD8+ effector and regulatory T cells (Fig. 4.23, 4.24, 4.25, 4.26). Under semi-sterile conditions, a controversial healing outcome was observed between the T_{Reg} enriched mice. 21 d post-surgery, the ratio between CD8+ T effector and T_{Reg} was significantly higher in the T_{Reg}+ bad vs. the T_{Reg}+ good animals (Fig. 4.43). In order to investigate whether the immune status of a mouse prior to osteotomy is determining the healing outcome after T_{Reg} enrichment, a proof of concept (POC) study was carried out. Therefore, blood samples were taken from seven mice prior osteotomy to evaluate the ratio of CD8+ effector T cells to T_{Reg}. These ratios are illustrated in table 4.2. The classification in a potential good or bad healing outcome was done without knowing whether there is really a certain threshold that determines the healing outcome and if yes, what value this threshold has. The cutoff was estimated to be 0.1 considering the ratios of the good and bad healing mice in the previous test. Mice with a lower threshold were classified as a good healer and mice with a higher threshold as bad healer.

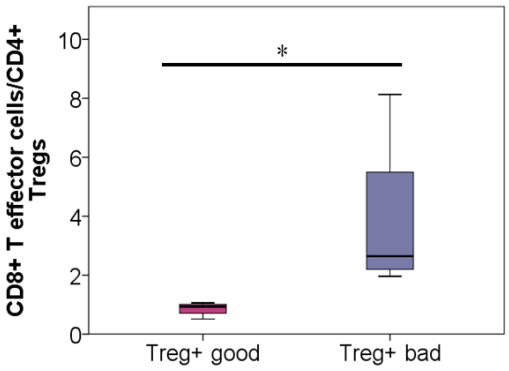

Figure 4.43: T_{Reg} enriched mice with a less good healing outcome had a higher ratio of CD8+ effector T cells to CD4+ T_{Reg} in comparison to the good healing animals. Ratio of CD8+ effector T cells to T_{Reg} in the peripheral blood of T_{Reg}+ mice 21 d post-surgery. Mice housed under semi-sterile housing conditions displayed a controversial healing outcome after T_{Reg} enrichment. Shown is the ratio of the above mentioned T cell subpopulation of the T_{Reg}+ good healer and T_{Reg}+ bad healer mice, respectively. *p= 0.029. n= 4

Table 4.2: Ratio of CD8+ T effector cells to T_{Reg} in the peripheral blood of seven mice prior to surgery. The predicted healing outcome is presented in the right raw. Numbers in the left raw represent the internal mouse numbering.

Mouse	Ratio CD8+ T_{EF}/T_{Reg}	Potential good or bad healer
1	0.048	good
2	0.078	good
5	0.107	bad
6	0.061	good
8	0.216	bad
13	0.060	good
16	0.049	good

T_{Reg} were freshly isolated, equally distributed to the recipient mice and the healing outcome was investigated after 21 d. In figure 4.44, the resulting µCT pictures of the seven mice are presented. A complete bridging was seen for mouse 1. Mice 6, 13 and 16 were still in the process of bridging, but at the time point of harvest not yet completely bridged. Further, a lack of bridging was observed for mice 2, 5 and 8. Comparing the µCT pictures and the predicted healing outcome, the prediction was true for all mice except mouse 2. Based on the estimated threshold of CD8+ effector T cells to T_{Reg} to 0.1, mouse 2 was determined as a good healer. However, the healing outcome showed a lack of bridging, thus an unsuccessful healing outcome. Mouse 2 showed the highest threshold regarding the predicted good healer. Thus, the estimated threshold was eventually not correctly set in order to predict the healing outcome. For the quantification of the µCT results, mouse 2 was included into the group with a poor healing outcome (Fig. 4.45). The less good healing outcome of the predicted non-healer was confirmed by the quantification of the µCT results. For the quantification, the data of the WT mice from the study of T_{Reg} enrichment under semi-serile conditions were used as controls (Chap. 4.2.1.5) (WT vs. bad healer; TV and BV: $p= 0.024$). Also the improved healing outcome of the POC good healer was quantified with regard to the WT animals (BV/TV: $p= 0.038$). For TV, BV and the ratio of both (BV/TV), the good healer clearly displayed a higher value in comparison to the bad healer ($p= 0.057$).
In order to exclude that the poor healing outcome was the result of an unsuccessful adoptive transfer of T_{Reg}, the proportion of T_{Reg} was determined 1 d post-surgery in peripheral blood (Fig. 4.46). A higher percentage of T_{Reg} was detected in both healing groups after adoptive transfer in comparison to the WT animals without a difference between the ensuing good and bad healing animals.
In figure 4.47, the correlation of the pre-calculated ratio of CD8+ T effector and regulatory T cells is demonstrated in a before-after-graph (graph for grouped data). The y-axis of the ratio of CD8+ effector T cells/T_{Reg} is reverted in order to have a better graphical illustration. This graphic clearly shows that the smaller ratio of both T cell subsets of the four mice with a good healing outcome correlated with a higher BV/TV without any overlay with the mice with a poorer healing outcome. Following, a linear regression analysis was performed with these data (Fig. 4.47 B). The coefficient of determination was calculated as $R^2 = 0.6236$.

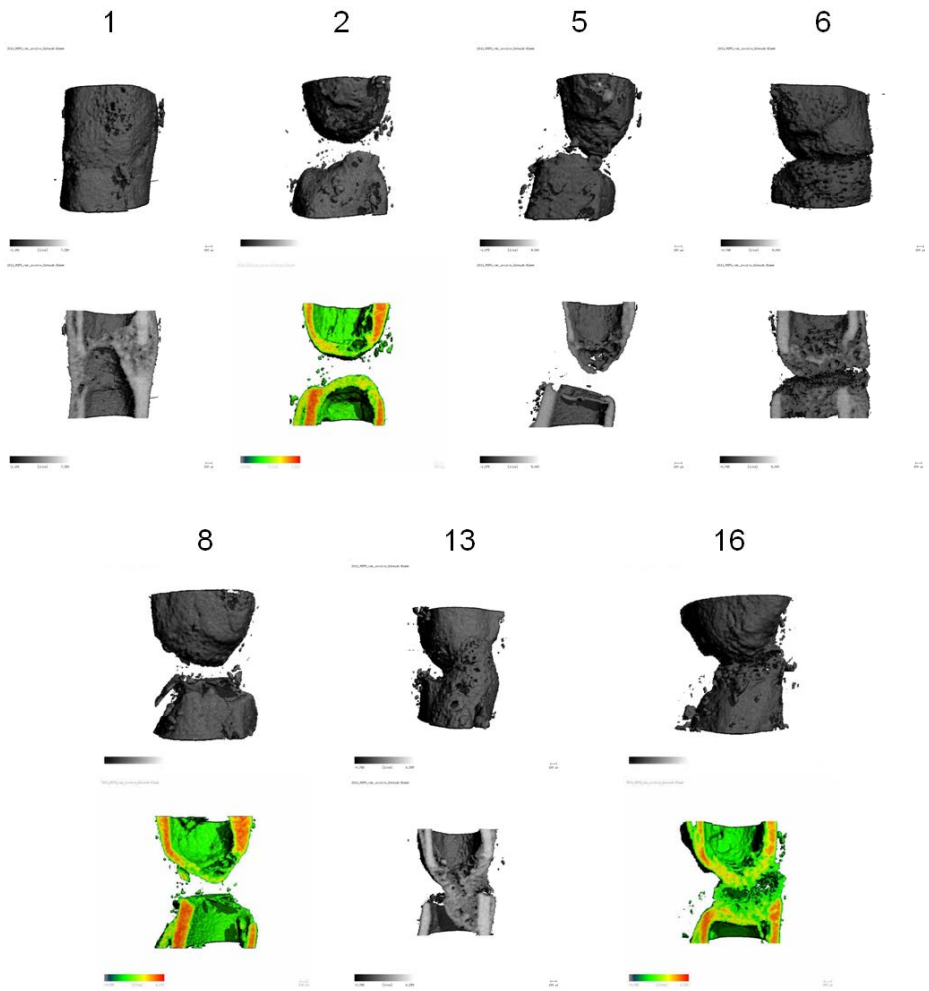

Figure 4.44: T_{Reg} enriched mice of the POC study displayed different healing outcomes after 21 d, µCT evaluation. Mouse 1 was completely bridged; mice 6, 13 and 16 are still in the process of bridging but not completely bridged yet; mice 2, 5 and 8 showed no bridging. In the lower pictures, the 3D images of the healing bones are cut sagittally/frontally to demonstrate the progress of the remodeling process. The color code indicates the mineralization state, with an increasing mineralization from black to white and blue to red, respectively.

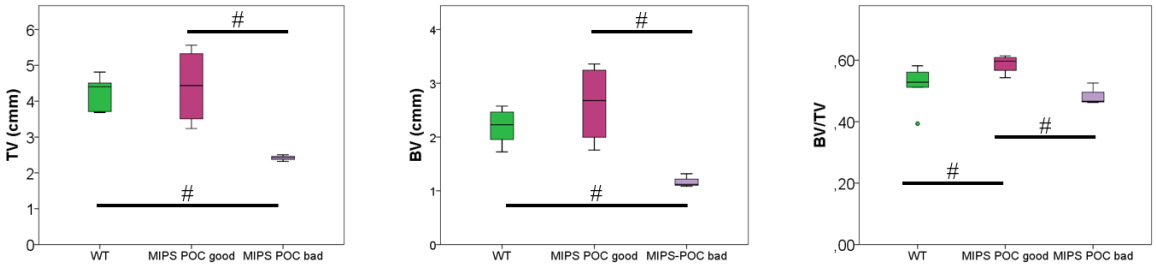

Figure 4.45: T_{Reg} enriched mice of the POC study displayed different healing outcomes after 21 d, µCT quantification. TV= total volume, BV= bone volume, and BV/TV= ratio of BV to TV. #p= 0.024—0.057; n= 3–6

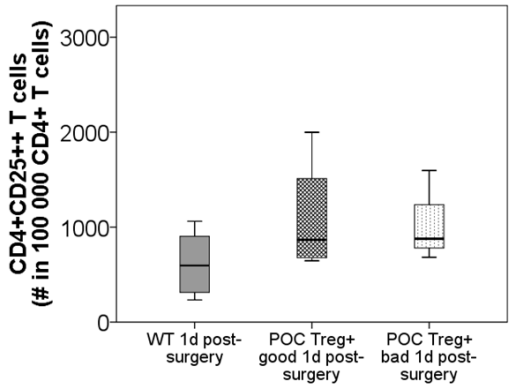

Figure 4.46: T_{Reg} enriched mice of the POC study displayed an increased proportion of CD4+ T_{Reg} in comparison to the WT 1 d post-surgery. Status of CD4+CD25++ T cells in the peripheral blood of the POC mice. Displayed is the cellular percentage post-surgery of WT (WT 1 d post-surgery), POC T_{Reg}+ good healer (POC T_{Reg}+ good 1 d post-surgery) and POC T_{Reg}+ bad healer (POC T_{Reg}+ bad 1 d post-surgery T_{Reg}+). n= 3–6

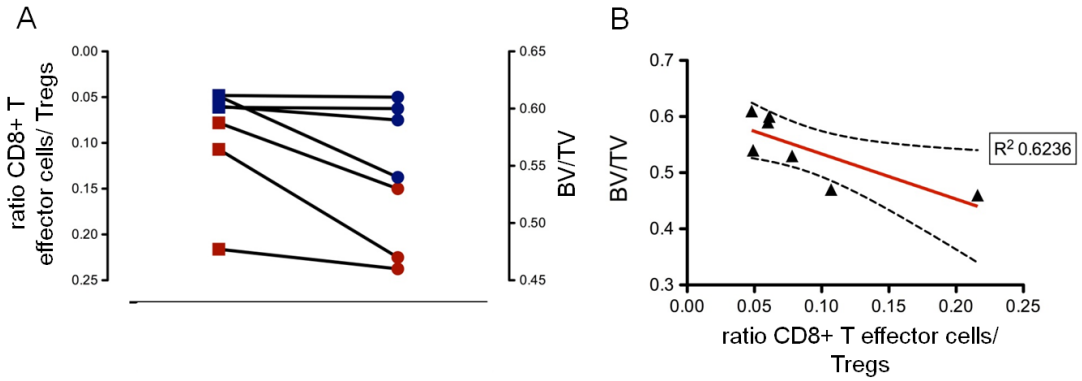

Figure 4.47: Confirmation of the relationship between the ratio of CD8+ effector T cells to CD4+ T_{Reg} and the healing outcome in the mice of the POC study. A) Before-after-graph (graph for grouped data). B) Linear regression analysis of the pre-defined ratio of CD8+ effector T cells and T_{Reg}. Illustrated are the regression straight, the corresponding 95 % confidence interval and the calculated coefficient of determination R^2.

In the proof of concept study, I could show that the pre-surgery status of the ratio of CD8+ T effector to T_{Reg} cells predicted the healing outcome under the here used experimental conditions. In the animals having a ratio above 0.075, the bad healing outcome could not be compensated anymore by the transfer of T_{Reg} as positive modulating cells. For the predicted bad healer of our mouse osteotomy model, the adoptive T_{Reg} transfer even led to a poorer healing outcome with regard to the untreated WT mice and thus should not be performed. However, the presented data are just preliminary and are therefore just indicating that the pre-osteotomy status of certain populations of the adaptive immunity is a relevant factor when immunomodulatory therapy is considered.

5 Discussion

Fracture healing is a highly complex process involving several tissues and cell types. They have to interact in a spatiotemporally well defined interplay in order to ensure the reconstitution of the injured bone [18]. Within secondary (indirect) healing, distinct but overlapping phases have to proceed for a successful healing outcome. The immune system plays an enormous role in bone homeostasis as well as in bone regeneration.
In the first part of my PhD study, an unaltered secondary healing process was characterized in a murine osteotomy model. Animal model systems are a useful tool in order to evaluate different phases of biological processes over a certain time period under comparable animal strain specific and environmental conditions. In the context of this analysis, the interplay between components of the bone and of the immune system was evaluated within the fractured bone. Systemically, the composition of distinct immune cell subsets was investigated. By immunohistology, specific distribution pattern were confirmed during the different healing phases within the fracture area. While B and T cells were detectable throughout the whole healing process, macrophages demonstrated a phenotype switch from a pro- to an anti-inflammatory one at around day 3-7. Anti-inflammatory macrophages seemed to invade the fracture area from the surrounding tissue. Their appearance further coincided with the formation of new vessels. The revascularization of the fracture gap also correlated with the disappearance of Hif1α+ cells, indicating the reestablishment of the necessary oxygen supply. Bone forming osteoblasts were detectable in the fracture area directly from the beginning on. As soon as small isles of newly formed bone were found in the gap area, also bone resorbing osteoclasts were detectable around them.
In the second part of my thesis, an immunomodulatory approach was tested within the characterized mouse model in order to improve the healing outcome after osteotomy. This was done by an enrichment of T_{Reg} prior to osteotomy. Prior to the enrichment, the pre-osteotomy immune status of the mice was analyzed, comparing animals housed under SPF and semi-sterile housing conditions which enabled the maturation of the immune system. These analysis revealed an increase of the proportion of the CD25+ T cell subset under semi-sterile housing conditions. In addition, the percentage of effector T cells also increased. Furthermore, an increase of T_{Reg} was specifically observed in the bone marrow of the semi-sterile housed animals. The positive modulating effect of an enrichment of T_{Reg} prior to osteotomy was confirmed in mice housed in an SPF environment. In contrast, mice housed under semi-sterile housing conditions showed a controversial healing outcome. This result clearly illustrates the importance to consider the individual immune status of the recipient prior to the application of an immunotherapy.

5.1 Analysis of an unaltered healing process in a mouse osteotomy model

5.1.1 Characterization of the spatial and temporal distribution of distinct cellular subsets within the fractured bone

The murine osteotomy model of a non-critical size defect used for this study recapitulates the classical and characteristic phases of a secondary healing process. After the initial hematoma/inflammatory phase, fibrocartilage tissue was present within the fracture gap that was further replaced by cartilage and finally newly formed woven bone. Concerning the distribution of distinct cellular subtypes within the fractured bones analyzed by immunohistology, macrophages, as component of the innate immune system, were detectable over the complete healing duration. Macrophages are needed in order to direct

the orchestrated formation of callus tissue. A complete depletion of macrophages at the time point of surgery led to a disturbed fracture healing process, visible by an impaired formation of soft and hard callus tissue [131]. In addition, after a chemically induced reduction of macrophages, a prolonged cartilage phase with a disturbed transition from soft to hard callus was detectable [5]. These studies highlight the important impact of macrophages already from the early phase on. At day 1–3, the detectable presence of pro-inflammatory macrophages represents the early inflammatory/hematoma phase of the healing process (Fig. 4.4–4.6). Opal and colleagues already reported an interdependency between pro-inflammatory signals, coagulation and the recruitment of cells of the innate immunity (monocytes, macrophages) in wound healing [132]. Although pro-inflammatory macrophages were detectable in the initial repair phase, no clear fracture hematoma was visible by MP staining (Fig. 4.2). A reasonable explanation is that the fracture hematoma was washed out by the sucrose solutions needed during the processing of the carefully harvested bones for the embedding process. The proceeding to the anti-inflammatory phase was detectable by the shift of M1 to M2 macrophages starting from day 3 [5]. The shift from pro-inflammatory M1 to anti-inflammatory M2 is an indispensable step for bone regeneration. M2 macrophages secrete pro-osteogenetic cytokines and thereby promote the formation of new bone [133]. After 7 days, fibrous tissue was visible in the fracture gap by MP stainings of the osteotomized mice femora that was further replaced by cartilage (Fig. 4.2, 4.3). This represents the fibrocartilage/soft callus phase. By immunohistochemistry stainings, predominantly anti-inflammatory M2 macrophages were detected in the fracture area. This further indicates the probably necessary orchestrating function of macrophages for the directed progression of the regeneration process during the soft and hard callus phases. Hif1α positive cells were detected within the fracture gap from day 1 onwards, illustrating the drop of the oxygen level within the fracture area due to the disruption of the blood vessels. Progenitor cells for the revascularization of the disturbed area (identified by CD105+ cells) were stained also directly from day 1 after fracture in the surrounding tissue but also within the bone marrow adjacent to the fracture gap. Hypoxic cells were still visible until day 7, except for day 3, but completely absent from day 14 on. The absence of Hif1α+ cells at day 3 indicates the sufficient reestablishment of the necessary oxygen supply for the fractured bone. This is further supported by the detection of vessel like structures of CD105+ cells within the analyzed area. Thus, the disappearance of Hif1α+ cells positively correlated with the onset of the vessel formation of CD105+ cells. The recurrency of hypoxic cells at day 7 could be due to the onset of the cartilage differentiation where again avascular conditions prevail. The appearance of newly formed vessels also coincided with the invasion of M2 macrophages in the fracture gap. This further demonstrates the participation of M2 macrophages in revascularization or the provision of macrophages via the newly formed vessels. An important involvement of both macrophage subsets in angiogenesis was already reported before [134]. T and B cells as parts of the adaptive immunity were present throughout the whole healing cascade in the bone marrow around the osteotomy gap. They showed a partial co-localization with osteoblasts and osteoclasts. Regarding osteoclastogenesis, T and B cells can act pro- or anti-osteogenetic [3, 64, 8, 135]. Activated T cells express RANKL and thereby stimulate the formation of osteoclasts. But, they can also inhibit osteoclastogenesis by the secretion of IFNγ. B cells express RANKL and OPG, respectively. Thus, they can also either support or inhibit the formation of osteoclasts. A supporting function of T cells in osteoblastogenesis was also reported before [136]. Thus, B and T cells seem to be necessary throughout the whole healing cascade in order to orchestrate the functioning of bone cells in fracture repair [135]. Osteoblasts, the bone producing cells, were detectable at the periosteum and directly within the fracture gap in the early healing phase. Their appearance in the fracture zone correlated with the invasion

of M2 macrophages. This further highlights the orchestrating function of M2 macrophages for osteoblast function and bone formation, as already mentioned above. During the soft callus phase, osteoblasts were also visible at the endosteal side of the cortices around the fracture area. This likely indicates the ongoing process of the production of new bone from the endosteal side for the regeneration of the fractured bone. Osteoclasts, the bone resorbing cells, were detectable on both sides of the cortices, directly from the beginning. Both, osteoclasts and osteoblasts were found around isles of newly formed woven bone as soon as they appear in the regeneration process. This demonstrates the remodeling of newly formed woven bone in order to reestablish the bony architecture. In accordance with already published findings, none of the investigated cell types was detected in areas of cartilage tissue [8]. After 21 d, a hard callus was formed that was partially also already remodeled, indicated by the observed lamellar structure of the newly formed bone tissue. The bone marrow composition of this healing phase was characterized by CD80- and CD206- macrophages, B cells, T cells and at the endosteum lying osteoclasts. Osteoblasts were again only found at the periosteal surface of the cortices. The findings at day 21 could represent the (beginning of the) reestablishment of the composition of the medullary canal as before injury.

5.1.2 Characterization of the systemic changes of distinct cellular subsets

Besides cellular changes within and around the fracture area, also systemic changes were detectable by flow cytometry, especially in the effector memory and central memory subset of T cells. Presented flow cytometry data were calculated on the basis of CD3+/TCRαβ+/CD4+ and CD3+/TCRαβ+/CD8+ T cells or CD3+/CD4+ T cells (for T_{Reg}). Thus, the data are presented as percentages and not amounts. In order to exclude false interpretation of observed shifting percentages between compared mice groups due to a shift already in the CD3+ T cell population, the percentages of CD3+ T cells were compared based on a defined lymphocyte gate in the SSC/FSC. No differences were detected in the resulting CD3+ T cell population between the groups of animals that were compared. In the spleen, the CD3+ T cells were 37 % of the living cells of the lymphocyte population with a standard deviation of 3.5. Thus, differences in the calculated percentages of the evaluated T cell subsets can be interpreted and discussed as real changes in the composition of T cell subsets.
Directly after injury, a decrease of the total CD4+ and CD8+ T cells, as well as their respective CD25+ and central memory subsets, was detectable. Alterations of the hosts adaptive immunity after injury, including a decrease in the systemic distribution of CD4+ and CD8+ T cell subsets, were already reported in the literature [137, 138]. These alterations are often associated with a T cell dependent unresponsiveness of the adaptive immunity [139], leading in the worst case to a multi organ failure of the patient. On the one side, the observed changes are suggested to be a compensatory reaction of the body due to the high early inflammatory phase caused by the injury [138]. However, on the other side, the early inflammatory phase after injury can also function as an attractant for cells of the adaptive immunity to the side of injury necessary for the repair process. This recruitment is probably mediated via the production of a high proportion of prostaglandin E by macrophages [140], further highlighting the tight interaction between the innate and adaptive immunity not only at the injury side itself, but also in the periphery. For CD8+ T cells, a constant decrease was observed in the bone marrow over the whole healing phase. This constant decrease was in contrast to the observed findings in the blood and spleen where the percentage of CD8+ T cells constantly increased from day 2/day 3. Also for the CD4+CD25+ T cell compartment, which includes activated, regulatory and effector T cells, the systemic bone marrow reacted

slightly different with regard to the peripheral blood and spleen. In the bone marrow, the decrease of the cellular proportion was much stronger, especially in the later phase (day 7–day 14). Regarding the total population of CD4+ and CD8+ T cells, as well as their CD25+ subsets, differences in the distribution over the healing process have been observed in the bone marrow for CD8+ and CD4+CD25+ T cells with regard to their distribution in the two other tissues. These findings potentially indicate a tissue specific systemic response of the body due to the injury. Thus, after bone fracture, reactions of the adaptive immune system do not only occure in the regenerating bone itself but also in the systemic bone marrow.
The proportion of the fast reacting effector T cells stayed relatively constant in all three analyzed tissues in the early healing phase. In the bone marrow, a constant increase was further detected over the whole cascade, which was not seen in the blood and spleen. The population of slower reacting effector memory T cells showed a clear increase in the first days after trauma. This indicates a reactivation of these cells initiated by the osteotomy and further supports the systemic involvement of the adaptive immunity during bone regeneration. Over the whole healing cascade, CD4+ and CD8+ effector memory T cells displayed an increased percentage, implicating their interaction in the regeneration process. However, this interaction was not tissue dependent. A clear decrease in the proportion of central memory T cells after osteotomy and further over the whole healing process in comparison to the pre-surgery value was seen. In the blood, they increased again from day 7, which was not seen in the bone marrow and spleen. The early systemic decrease of central memory T cells could be explained by the interdependency and plasticity of the different T cell memory subsets in mice. Wherry and colleagues proposed a model of a continuum lineage commitment of central and effector memory T cells rather than talking about distinct subpopulations, seeing the central memory T cells as the real final memory subset: T effector → T effector memory → T central memory [141]. After antigen re-stimulation, central memory T cells can convert back to the effector memory subset [142]. This re-conversion could explain the observed decrease of the central memory subsets in bone marrow, spleen and peripheral blood which occured simultaneously with the increase of the effector memory T cells. However, all these analyses focusing on the plasticity and re-conversion of memory T cell subsets were carried out with an antigen dependent effect on these cells. So far, little is known about the role of memory T cells in bone repair. It is still unclear how theses T cells exactly interfere and how they get activated in bone regeneration. Reinke and colleagues clearly showed the high impact and negative correlation of an increased number of CD8+ T_{EMRA} cells in the human peripheral blood and an impaired healing outcome after isolated, closed tibia head fracture [4].
The population of regulatory T cells showed clear changes in the contralateral bone marrow where the percentage constantly increased directly after fracture till 21 d post-surgery (Fig. 4.14). This observation indicates either a systemic involvement of T_{Reg} over the whole healing cascade in bone regeneration or an influence of the regeneration process after osteotomy on the T_{Reg} population in the contralateral and thus systemic bone marrow. An injury dependent suppressive activity of T_{Reg} on cells of the innate immunity as well as their positive impact in the healing outcome after burn injury was already reported [143, 144]. Thus, this could demonstrate a tissue specific effect of the osteotomy on the subpopulation of T_{Reg} by inducing their systemic increase in the total bone marrow. This could further imply that after bone injury, the T_{Reg} percentage is up-regulated in order to orchestrate the well-defined repair process for a successful healing outcome. However, the frequency of T_{Reg} within the fractured bone itself was not analyzed in this study. In this context, Al-Sebaei and colleagues already showed in a mouse study that the T_{Reg} percentage is also upregulated in the injured bone in comparison to the pre-injury value [145].

In conclusion, this first part of my PhD thesis gives for the first time an overview of the interplay of bone cells, immune reaction, hypoxia and vessel formation during secondary bone healing which was investigated by immunohistology. This part further covers the different healing phases and investigates all the tissues participating in the healing process (bone, endosteum, periosteum, bone marrow, callus and muscle). The tight interplay of the bone and the immune system within the injured femur as well as the systemic impact of the adaptive immunity in bone regeneration is clearly demonstrated by the presented data.

5.2 Changes in the murine adaptive immune system comparing SPF and semi-sterile housing

Within an aging population, the risk for fractures increases [146, 147]. In addition, fractures of aged people show a higher percentage of impaired healing outcomes [148]. Throughout life, the human immune system is constantly exposed to pathogens. This leads to an activation of the adaptive immunity. Thus, an older person has a more experienced immune system compared to a younger person. This is reflected by a higher amount of memory T cells [149]. The question is how these changes in the immune cell composition will impact bone fracture healing.
During this study, a more experienced immune system of the experimental mice was induced by using different housing conditions and thereby mimicking an immune system of older people. In the semi-sterile environment of our animal facility, mice were exposed to a higher amount of pathogens in comparison to those animals housed under SPF conditions. As seen in humans, a higher activation status of the immune system is detectable by an increasing percentage of activated, as well as effector T cells within the experimental mice. For theses mice, a more experienced immune system was confirmed by an increase of CD4+CD25+ and CD8+CD25+ T cells (activated T cells and T_{Reg}) as well as of the effector pool of both T cell subsets in the spleen of mice in the semi-sterile housing. Effector cells are produced following antigen stimulation of naïve T cells. Thus, a higher amount of effector cells is the consequence of a higher antigen exposure to pathogens. Furthermore, the simultaneously observed decrease of central memory T cells alone (CD8+ T cells) or both effector memory and central memory T cells (CD4+ T cells) highlights again the proposed plasticity of these three T cell subsets (effector, effector memory and central memory) [141]. Regarding bone regeneration after injury, we are just at the beginning to elucidate the impact of effector and memory T cells. One of the main questions is how effector and memory T cells can interact in bone repair. Is it an antigen-driven process or bystander activation [150]? Bystander activation means that memory T cells are indirectly activated during bone repair by e. g. cytokines released by other cells and is thereby independent from antigen stimulation. Another aspect of an increasing effector and memory T cell pool is a changing antigen specificity. T cells are characterized by their antigen specific TCR. Thus, a higher amount of effector T cells leads to a changing TCR repertoire of effector and central memory T cells between mice housed under the two different housing conditions. Follow-up studies will be needed in order to further investigate the differences in the TCR repertoire in depth. This was not the focus of my project. However, a changing TCR repertoire would further influence the specificity and recall response capacity between T cells from both housing environments. For the subpopulation of T_{Reg}, semi-sterile housed mice displayed a higher percentage in the bone marrow, whereas no changes were detectable in the peripheral blood and spleen. This finding further highlights the importance of the bone marrow as a reservoir for T_{Reg}, especially in an organism with a more experienced immune status.

Different housing conditions effectively impacted the immune cell composition of the analyzed mice. In the spleen, the semi-sterile environment caused a change in the ratio of effector to effector memory to central memory T cells to T_{Reg} of both T cell subsets, CD4 and CD8. These changing ratios are due to changes in the effector and memory subsets but unaffected T_{Reg}. But also in the bone marrow, changes in the ratio of these four subpopulations were revealed due to the higher percentage of T_{Reg} but an unchanged proportion of effector, effector memory and central memory T cells between animals housed under the different housing conditions. In the clinical situation, a changing immune cell composition in older patients, as it was artificially mimicked in the semi-sterile housed mice, could negatively influence the process of tissue regeneration by creating an unfavorable cytokine milieu at the site of injury (inflammaging) [151]. This might further impair the healing outcome which is already observed in a certain percentage of older patients [148].

5.3 Immunomodulation of the bone fracture healing process

5.3.1 Enrichment of regulatory T cells prior to osteotomy

The investigation of the healing outcome after adoptive T_{Reg} transfer was carried out with freshly isolated murine T_{Reg}. Apart from the required high purity and functionality of the isolated T_{Reg} for this immunomodulatory approach, the activation status of the used T_{Reg} was considered. These parameters had to be tested and confirmed prior to adoptive transfer. In order to obtain a highly purified cell population, magnetic activated cell sorting (MACS) was used. This is an already well-established and accepted technique for the isolation of murine cell subsets with a high purity. After MACS purification, I confirmed a purity of around 85 % of mouse T_{Reg} from spleen and lymph nodes (Fig. 4.16). The functionality of the freshly isolated T_{Reg} was analyzed in a T_{Reg} suppression assay. T_{Reg} are characterized by their ability to suppress the proliferation of CD4+CD25- T_{Resp} in co-culture systems. When cultured alone, several studies already reported an unresponsiveness of T_{Reg} to TCR stimulation that was not observed to TCR-independent stimuli, like phorbol-12-myristat-13-acetat (PMA). However, when co-cultured together with T_{Resp}, the same studies also reported a TCR stimulation-dependent successful suppression of the proliferation of T_{Resp} by T_{Reg} [152, 111]. These findings are in accordance with my data, showing a dose-dependent suppressive capacity of freshly isolated murine T_{Reg} on the proliferation of T_{Resp}. Thus, the freshly isolated T_{Reg} are still functional. Several reports in the literature state an even superior suppressive activity after *in vitro* pre-activation of murine and human T_{Reg} on the proliferation of T_{Resp} (consideration of the activation status of the used T_{Reg}). In contrast, in my study, pre-activated T_{Reg} did no show a higher suppressive response but rather a loss of their suppressive capacity. No standard protocol exists for the pre-activation of freshly isolated T_{Reg}. Different groups used different media compositions, different cell numbers, and different pre-activation time periods [153, 154, 112]. Thus, although I observed a higher expression of the activation marker CD69 in the pre-activated T_{Reg}, it is still possible that the used conditions in my pre-activation culture were at least partially unfavorable for their suppressive capacity. In addition, after an *in vivo* pilot test of adoptive transfer of freshly isolated and pre-activated T_{Reg}, respectively, prior to osteotomy in mice, an improved healing outcome was only observed with freshly isolated T_{Reg} with regard to untreated WT animals but not with pre-activated T_{Reg} (data not shown). Based on these preliminary data and on the *in vitro* findings from the pre-activation and T_{Reg} suppression assay, the following immunomodulatory *in vivo* approach was realized with freshly isolated murine T_{Reg}.
In this study, I have confirmed the capacity of freshly isolated murine T_{Reg} to improve

fracture healing in the used mouse osteotomy model. However, this was only completely true when T_{Reg} recipient mice were housed under SPF conditions. Under semi-sterile conditions, the healing outcome was controversial; one half of the animals healed significantly better, the other half showed a significantly poorer healing outcome. A higher percentage of T_{Reg} 21 d post-surgery in the bone marrow and spleen of the T_{Reg} enriched with regard to the WT animals confirmed the successful T_{Reg} enrichment in the good as well as bad healing mice. However, the obvious controversial healing outcome of the adoptively transferred T_{Reg}+ mice clearly demonstrates the impact of the housing condition on the healing outcome. This could either be an impact of the transferred cells, thus of the donor mice, an impact of the recipient animals or an impact of the process of the adoptive T_{Reg} transfer. Regarding possible negative influences of the isolated T_{Reg} cells used for the adoptive transfer, I have successfully confirmed that freshly isolated murine T_{Reg} via MACS technology possessed a high purity and were still functional in their suppressive capacity. Furthermore, the successful adoptive transfer was proven and confirmed. For an adoptive transfer experiment, I always isolated T_{Reg} simultaneously from 2–4 mice, pooled them and distributed them equally to the recipient mice. Thereby, the number of donor and recipient mice was equal and up to 4 mice received the same T_{Reg} transfer. Within such a cell pool, different healing outcomes were observed (good vs. bad). These observations exclude the cell source per se as the cause for the controversial healing outcome of the T_{Reg} enriched mice. The recipient mice were litter mates and had the same age at the time point of surgery. Mice in one cage belonged to one delivery. Within one cage, there were good and bad healing animals. The healing outcome was further independent of the surgical order of the mice. Therefore, the remaining reasonable explanation for the observed different healing outcomes are likely to be differences in the immune status of the recipient mice prior to osteotomy due to the semi-sterile housing environment. As already shown in this study, the semi-sterile environment leads to an activation of components of the adaptive immunity which might further negatively impact the healing outcome.

Bone fracture healing is an inflammation mediated as well as immune cell dependent regeneration process. In bone related diseases like rheumatoid arthritis, an overwhelming pro-inflammatory reaction driven by activated T cells is responsible for the observed disease phenotype of bone loss [155, 156]. T_{Reg} are characterized by the capacity to suppress the pro-inflammatory activity and effector function of activated CD4+ and CD8+ T cells and thereby balancing the immune reactions within an organism. Thus, a well-defined ratio and interplay of T_{Reg}, as potential good cells, and activated/effector/memory T cells, as potential bad cells, is indispensable for a well-balanced immune homeostasis. Also in fracture healing, a too high amount of terminally differentiated CD8+ memory T cells correlates with impaired fracture healing outcome [4]. T_{Reg} could represent one counteracting part by diminishing the effector function of activated and memory T cells [99]. Thereby they could promote the successful progression of the healing cascade. However, to my knowledge, this interplay has not been analyzed in bone regeneration so far. Regarding the systemic flow cytometry data after 21 d from the good and bad healers of the T_{Reg} enriched mice, the bad healers clearly showed a higher percentage of activated and effector T cells (CD4+CD25+, CD8+CD25+, CD4+ effector and CD8+ effector T cells) in comparison to the good healers. It remains unclear if these differences had been already present before osteotomy or if they are a result of the poor healing outcome after 21 days. Besides the different proportions of activated and effector T cells, also the ratio between them and the present T_{Reg} was different for the respective tissue (T_{Reg} distribution was equal in all three evaluated organs between good and bad healer). Based on our previous findings [4], the ratio of CD8+ effector T cells and T_{Reg} was of special interest. Both T cell subsets are present in the bone marrow as already shown in the flow cytometry data obtained in the first part of my PhD thesis. This further

supports the assumption that they might also be involved in fracture repair directly in the injured bone. Regarding the different housing conditions, a shift in the ratio of CD8+ to regulatory T cells was shown due to a changing T_{Reg} percentage in the bone marrow in the semi-sterile environment (Fig. 4.26). This could further influence the progression of the healing process after bone injury. Coming back to the controversial healing outcome, a higher ratio of CD8+ T effector cells to T_{Reg} correlated with a poorer healing outcome, demonstrating a shift of the balance between the two cell types towards CD8+ effector T cells (Fig. 4.43). This further supports our assumption of a well-regulated interplay between CD8+ effector and regulatory T cells for an organized regeneration process after bone injury. It remains open how T_{Reg} can interact in bone regeneration. Zaiss and colleagues intensively studied the interplay of T_{Reg} and osteoclasts and showed that T_{Reg} inhibit osteoclastogenesis in a cell-cell-dependent mechanism. They further demonstrated that this interaction is CTLA-4 dependent, but does not interfere with the RANKL-OPG homeostasis [14, 15, 16]. They also showed that T_{Reg} play a crucial role in normal bone homeostasis. In FoxP3 transgenic mice, a higher bone mass as well as a protection of ovariectomy-induced bone loss was observed compared to a control group. This further highlights the importance and impact of T_{Reg} in the bone metabolism independent from an injury. Going back to our focus on the interplay between CD8+ effector and regulatory T cells, several *in vitro* and *in vivo* studies already showed a possible suppressive effect of T_{Reg} on naïve CD8+ T cells and their differentiation capacity [157, 158]. During the analysis of the characterization of the unaltered healing process in the first part of my study, I showed an increase of CD8+ effector as well as effector memory T cells in the bone marrow over the healing process (Fig. 4.13). An interference of T_{Reg}, especially in the early inflammatory fracture healing phase, could be an indispensable step in order to balance this effector/effector memory cell development as reported by the aforementioned studies. In a viral vaccine model, Kastenmuller and colleagues further demonstrated a specific effect of T_{Reg} on effector CD8+ T cells, without affecting the memory pool [159]. In accordance with other studies, the T_{Reg} mediated suppression was carried out via the limitation of IL-2, needed for effector T cell differentiation and stability. In contrast to this study, a direct negative correlation between the presence of T_{Reg} and CD8+ memory T cells was shown in an *in vivo* situation [160]. The authors concluded a partial negative impact of IL-2 on the maintenance of CD8+ memory T cells. T_{Reg} depletion by an anti-IL-2 treatment even led to an increase in the amount of CD8+ memory T cells. I observed the opposite finding in my study. After T_{Reg} depletion by anti-CD25 treatment, also the proportion of effector memory T cells markedly decreased (Fig. 4.41, 4.42). A possible explanation for this contradictory finding is the definition of a memory T cell subset. Murakami defined them by the expression of CD122, whereas I used the marker set of CD44 and CD62L. It is highly possible that these could represent two different subtypes of T cells, differently affected by the presence of T_{Reg} and by the anti-CD25 treatment [161]. However, the described findings from the literature and my own study clearly highlight the still missing depth in our knowledge of T_{Reg} action on CD8+ effector/memory T cells, especially in the context of fracture healing.

Our data do yet not explain the observed controversial healing outcome in the mice with a more experienced adaptive immune system (semi-sterile housing) and the significantly poorer healing outcome in the non-healers. At first glance, the non-bridging after T_{Reg} enrichment indicates also a possible negative impact of T_{Reg} in bone regeneration. One may assume that a well-defined interplay between CD8+ effector and regulatory T cells is a prerequisite for a successful healing outcome. An enrichment of T_{Reg} prior to surgery would shift the ratio towards the anti-inflammatory T_{Reg} which would thereby accelerate the fracture healing process. This acceleration was observed in the SPF and partial in the semi-sterile T_{Reg}+ animals (good healing mice). The faster healing of the fracture ends

could be realized by a suppression of the action of CD8+ effector T cells. Now, one may imagine a pre-surgery situation in which the ratio between the two is markedly shifted towards the CD8+ effector T cell population and an enrichment of T_{Reg}, as done in my study, would not be sufficient anymore to balance this ratio towards a regenerative setting. A growing number of studies have challenged the previously stated opinion that T_{Reg} are a committed stable cellular subpopulation. Then, under certain circumstances, T_{Reg} can lose their FOXP3 expression and can, dependent on the present environmental stimuli; convert to another CD4+ effector T cell subset [162, 163, 164, 165]. This conversion could have a negative impact in bone healing. Among others, CD4+ effector cell types interact differently in the process of osteoclastogenesis and can thereby modify bone regeneration. For CD4+ T cell subpopulations, it was already shown that Th1 and Th2 cells inhibit the differentiation of bone resorbing osteoclasts by the secretion of IFN-γ and IL-4, respectively. In contrast, CD4+ Th17 T cells are pro-osteoclastogenic by their production of RANKL. This can act directly on osteoclast precursors. In addition, Th17 cells can also induce the secretion of RANKL by osteoblasts and synovial fibroblasts. Although Th17 cells also seem to act pro-osteogenic, it is further postulated that the reason for several bone disorders like rheumatoid arthritis, osteoporosis and periodontitis is an imbalance of the ratio of Th17 and T_{Reg} cells [104, 105]. Several *in vitro* studies with human and murine cells revealed a possible transition between T_{Reg} and IL-17 producing (Th17) T cells. Xu and colleagues reported an IL-6 dependent shift of T_{Reg} to IL-17 producing cells in *in vitro* analyses with murine T_{Reg} [162]. In further studies, murine T_{Reg} that also express Rorγt, the master transcription factor of Th17 cells, were shown to be able to obtain the production of IL-17 after co-culture with selectively activated dendritic cells [166]. This conversion between purified T_{Reg} to IL-17 producing T cells was also demonstrated with human cells [167, 168]. In this context, Beriou and colleagues reported a possible stimulus dependent simultaneous loss of suppressive capacity of IL-17 secreting T_{Reg}.
Recalling a pre-surgery situation of an unbalanced CD8+ effector to regulatory T cell ratio towards the CD8+ T effector cells: If the amount of adoptively transferred T_{Reg} was not sufficient in order to re-balance this ratio, effector/memory T cells and in particular CD8+ ones could have created such a pro-inflammatory and unfavorable cytokine environment that the enriched T_{Reg} attracted to the site of injury could have been converted into a negatively modulating effector cell population like IL-17 secreting T_{Reg}. This assumption, of course, is highly provocative. However, the aforementioned publications reporting the interplay between CD8+ and regulatory T cells as well as the plasticity between T_{Reg} and IL-17 producing cells strongly support this possible conclusion. A totally different explanation for the observed controversial healing outcome could be a too strong presence of T_{Reg} in the fracture area after adoptive transfer. A too high amount of T_{Reg} could directly suppress the indispensable pro-inflammatory reaction in the initial fracture healing phase and could thereby promote an impaired regeneration process.
Follow up studies are already planned to analyze this apparently crucial interplay between different cellular subtypes of the adaptive immune system and T_{Reg} as well as bone cells and T_{Reg} in order to obtain a deeper knowledge about the underlying mechanism of T_{Reg} interaction in bone regeneration.

5.3.2 Depletion of CD25+ T cells prior to osteotomy

In order to investigate the healing outcome when T_{Reg} are absent at the moment of osteotomy, a CD25+ T cell depletion was performed prior to surgery. Anti-CD25+ T cell depletion is a widely used approach to deplete specifically T_{Reg} in mice studies analyzing e. g. tumor

immunology, transplantation tolerance and infection models [128, 129, 130]. All of these studies reported a successful depletion of T_{Reg} and subsequently a successful immune-based therapy. The depletion of T_{Reg} cells was also confirmed in the presented study by flow cytometry 2 d post-depletion and post-surgery. In contrast to the expectation, this depletion did not alter the healing outcome with regard to the WT control animals. A poorer healing outcome was expected due to the missing T_{Reg} as positive modulating cell population in bone regeneration. The evaluation of the healing outcome after 21 d by μCT and histomorphometry was comparable to the one seen in the WT mice (Fig 4.37, 4.38, 4.39). In addition to the T_{Reg} depletion, a reduction or even absence after anti-CD25 antibody treatment was also observed for effector T cells. CD4+ and CD8+ effector as well as activated and certain memory T cells also express the CD25 molecule on their surface. Thus, these T cell subsets will also be depleted by this antibody as shown in this study for the effector subpopulation. In accordance, there are also experimental approaches reported in the literature showing a failure to consistently enhance the therapy outcome after T_{Reg} depletion by an anti-CD25 antibody treatment. The authors consider an unspecific effect of the anti-CD25 treatment on other CD25+ T cell populations [169, 170, 171]. They explain the observed inconsistent therapy success after T_{Reg} depletion with a simultaneous unwanted depletion of other CD25 expressing T cell subsets. Interestingly, the population of effector memory T cells also decreased, indicating an effect of the CD25+ T cell depletion also on this cell subpopulation although they do not express CD25. Thus, this antibody does not specifically deplete CD25+ T_{Reg}, but also other T cell subsets expressing the surface marker CD25 and affects furthermore CD25- cellular subsets. The observed decrease of CD8+CD25- effector memory T cells could be an indirect effect of the depletion approach. One explanation is that the organism tries to reconvert effector T cells from the memory pool. If the antibody directly affects the already present as well as the reconverted CD25+ effector T cells, the organism will carry on to reconvert more and more effector memory T cells to effector cells. Thereby, the proportion of T effector memory T cells also decreases.
To conclude, the use of an anti-CD25 antibody as immunomodulatory approach does not only deplete CD25+ T_{Reg} cells, but also other cell populations expressing CD25. Although this depletion obviously changed the immunological homeostasis within the treated animals, the balance between CD8+ effector T cells and T_{Reg} remained constant comparable to the WT mice regarding the outcome of the bone regeneration process. This could be an explanation for the investigated unchanged healing outcome of the depleted animals with regard to the WT because both T cell subsets, T_{Reg} and CD8+ effetor T cells, lack at the moment of osteotomy. This further supports the assumption that a balanced ratio between CD8+ effector T cells and T_{Reg} is required for a successful healing outcome in the used mouse osteotomy model system.

5.4 Identification of a potential biomarker to predict the healing outcome after adoptive transfer of regulatory T cells

The flow cytometry data after 21 d of the T_{Reg} enriched mice housed in a semi-sterile environment showed an increased percentage of possible negative acting cells in bone repair (CD8+ effector T cells) in the peripheral blood of the T_{Reg}+ bad vs. the T_{Reg}+ good animals (Fig. 4.34 A). Due to the fact that the distribution of T_{Reg} was equal in these animals in the blood after 21 d, the interplay and ratio of both CD8+ effector T cells and T_{Reg} might be crucial for a successful healing process. This assumption is further supported by the findings of Reinke and colleagues who already reported a negative impact of CD8+ effector T cells in bone repair in patient samples [4]. Therefore, a proof of concept (POC) study was performed

in which the healing outcome of a pre-surgery defined ratio between CD8+ effector and regulatory T cells was analyzed 21 d after T_{Reg} enrichment in the murine osteotomy model. Due to the small sample size and thus measurable and analyzable cell numbers in 1–2 drops of peripheral blood, only small ratios of CD8+ effector to regulatory T cells could be calculated pre-osteotomy (Tab. 4.2). However, differences in the ratios were clearly detectable, indicating different immune statuses in the experimental mice. Regarding the healing outcome after 21 d, the pre-surgery defined healing outcome was confirmed for all mice except mouse 2 (Fig. 4.44). The healing outcome was predicted using an estimated set threshold. Mouse 2 showed the highest pre-surgery ratio from the predicted good healer. In fact, we consider the set threshold to be not exactly true and consequently corrected the threshold from 0.1 to around 0.075. Thus, based on the μCT pictures, mouse 2 was included into the mice with a poorer healing outcome. The quantification of the μCT of the POC animals clearly confirmed a better healing outcome in the good healers with regard to the bad healers (Fig. 4.45). Furthermore, the bad healers demonstrated again even poorer bone regeneration in comparison to the corresponding WT mice. An unsuccessful adoptive T_{Reg} transfer as the cause of the observed non-bridging in the bad healing POC mice was excluded due to the proof of the cell transfer 1 d post-osteotomy in peripheral blood. Both healing groups of the POC animals showed a relative higher value of T_{Reg} with regard to the WT. A direct linear correlation between the pre-osteotomy ratio of CD8+ effector T cells and T_{Reg} and the healing outcome has not been determined in the POC study ($R^2 = 0.6236$). Nevertheless, the prediction of a healing outcome does not neccessarily follow a linear behavior. The before-after-graph clearly shows the correlation between a higher ratio of CD8+ effector T cells to T_{Reg} and the poorer bone regeneration without any overlap (Fig. 4.47 A). Obviously, this effect was not altered after adding the adoptively transferred T_{Reg}. We conclude that there is a certain threshold for the animals of the POC approach that predicts a poorer healing outcome when the ratio is higher 0.075. Thus, for the POC approach, I confirmed that a pre-defined ratio of CD8+ effector memory T cells to T_{Reg} correlated with the healing outcome after T_{Reg} enrichment in the given experimental conditions.
It is important to mention that only seven animals were analyzed for the experimental setting in the POC study. More studies would be needed in order to confirm the observed results. Thus, the observed findings are just indications for the evaluated data as well as healing outcomes and have to be interpreted with caution. However, the herein defined threshold clearly shows that there are differences in the cellular composition of the used mice that influence the healing outcome and probably also the fate of the adoptively transfered T_{Reg}. Likely, these cells do not act as T_{Reg} when cast into the high effector environment but change into cells that are detrimental for the healing process and thus cause a significantly poorer outcome.

5.5 Conclusion

The obtained and presented data of the immunomodulatory treatment approach clearly demonstrate the impact of the immune status on the regenerative process of bone. This impact is determined by the maturation/experience of the adaptive immune system due to pathogen exposure. In figure 5.1, the findings are schematically illustrated, including the state of the scientific knowledge my PhD thesis is based on (Fig. 5.1, upper picture). Under SPF housing conditions and thus a lesser experienced immune system, adoptively transferred CD4+ T_{Reg} led to a consistently improved healing outcome in our clinically relevant mouse osteotomy model in comparison to the wild type control group (Fig. 5.1, lower left picture). Semi-sterile housing led to a more experienced adaptive immunity of

the immune system due to a higher pathogen exposure. Hereby, the healing outcome was dependent on the ratio of CD8+ effector T cells and CD4+ T_{Reg} that was present in the mouse before osteotomy and immunomodulation (Fig. 5.1, lower right picture). Therefore, the immunomodulatory treatment approach shows the importance of considering the immune status of each individual before applying an immunomodulatory therapy. Transferring these findings to the clinical situation cautions how individual each patient could react to the same immunomodulatory therapy and how this approach could affect the treatment outcome in an unfavorable way. Therefore, for the clinic, it is even more important to develop and to apply patient based treatment approaches in the field of immunotherapy considering the individual immune status of each patient prior to treatment.

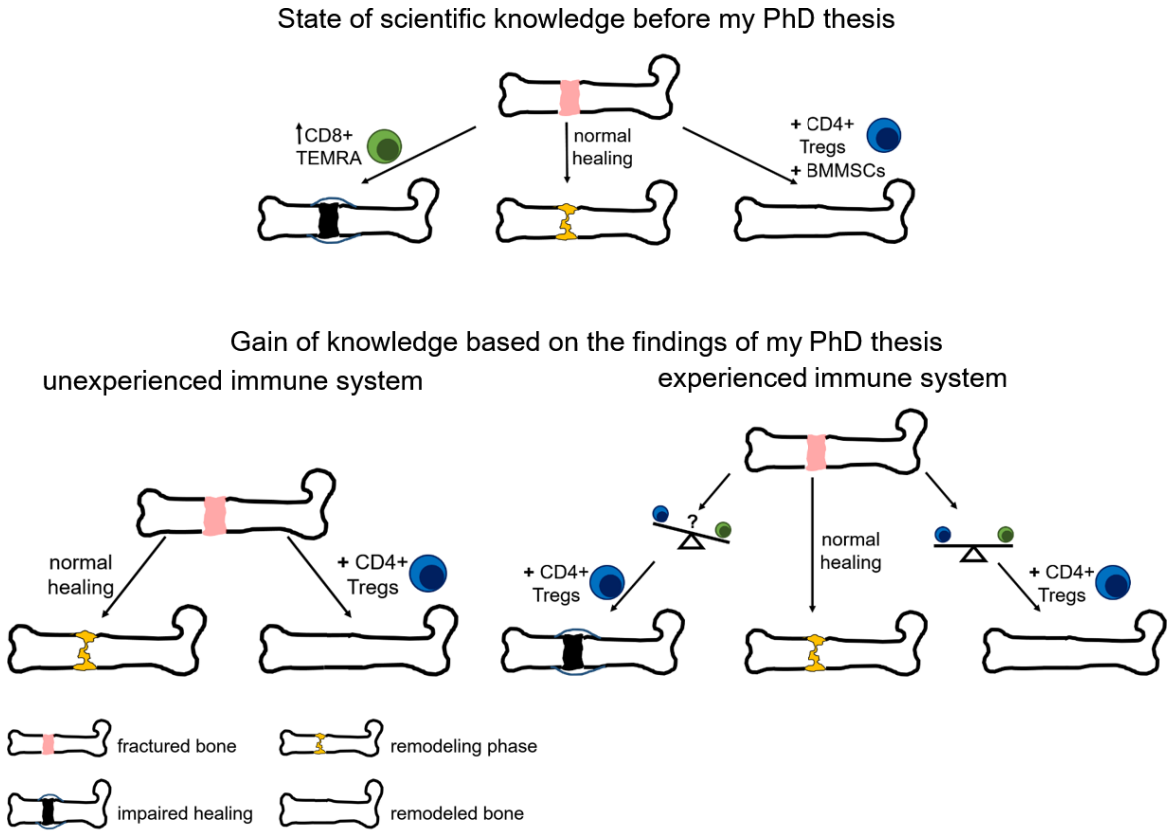

Figure 5.1: Interplay between the adaptive immune system, immunomodulation and bone fracture healing. Schematic illustration of the scientific knowledge before I started my PhD thesis (upper picture) and the gain of knowledge based on the findings of my PhD thesis (lower picture). Upper picture: CD8+ TEMRA T cells were already shown to have a negative impact in bone repair (humans and mouse model, long bones) whereas CD4+ T_{Reg} were shown to improve bone repair when simultaneously transferred with bone marrow MSCs (mouse model, skull). Lower picture: In bone repair, the healing outcome after immunomodulation by adoptively transferred CD4+ T_{Reg} is dependent on the status of the adaptive immune system before therapy. Using mice with an unexperienced immune system (SPF housing), the healing outcome was improved after CD4+ T_{Reg} transfer. However, using mice with an exprienced immune system (semi-sterile housing), the healing outcome after adoptive transfer of CD4+ T_{Reg} was dependent on the ratio of CD8+ effector T cells to T_{Reg}. Colors in bone scheme: cortices = black, hematoma = rose, callus = blue, newly formed bone = yellow, impaired healing = black in the fracture area; color code of the cells: CD8+ T cells = green, CD4+ T_{Reg} = blue.

5.6 Outlook

The here presented study clearly elucidates the tight interplay between the bone and the immune system in bone regeneration. The data also shows a circumstance-dependent positive modulating effect of murine T_{Reg} in fracture repair, as hypothesized at the beginning of this project. However, one major unanswered question is how T_{Reg} exactly interact in bone healing. Are tissue resident T_{Reg} responsible for the healing process? Are they recruited from the periphery? If yes, is this attraction mediated by cytokines released in the fracture area or in the periphery due to the injury? Furthermore, the functional mechanism of T_{Reg} action in bone repair is not completely revealed. How do they interact in the injured bone and with which cells do they interact?

In order to elucidate the spatial and temporal localization of T_{Reg} in bone healing, the behavior of T_{Reg} would have to be monitored in *in vivo* models. This could be realized by fluorescently labeled T_{Reg} and by a subsequent imaging analysis of the fracture area at different time points of the healing cascade. Using *in vitro* co-culture setup systems of T_{Reg} and different cell types of the innate and adaptive immunity, as well as bone cells, will allow to further analyze the working mechanism of T_{Reg}. Such an approach also includes the use of blocking antibodies or induced pro-inflammatory conditions in order to evaluate changes in the T_{Reg} behavior or T_{Reg}-independent changes in the behavior of the co-cultured cell type(s).

The here presented data clearly demonstrate the impact of the environment in which the experimental mice are housed in on the status of their adaptive immune system. So far, only the distribution of T_{Reg} was investigated between a lesser and a more experienced immune system. Another big question is the influence of the environment and thus of the pathogen exposure on the functionality of the respective T_{Reg}. This has not been investigated by any study so far. Especially for the translational use of experimental model systems analyzing immunomodulatory approaches with T_{Reg}, differences in the immune status of the used animals have to be considered as shown in my study.

Bibliography

[1] T. A. Einhorn and J. M. Lane. Significant advances have been made in the way surgeons treat fractures. *Clin Orthop Relat Res*, (355 Suppl):S2–3, 1998.

[2] C. Zeckey, P. Mommsen, H. Andruszkow, C. Macke, M. Frink, T. Stubig, T. Hufner, C. Krettek, and F. Hildebrand. The aseptic femoral and tibial shaft non-union in healthy patients - an analysis of the health-related quality of life and the socioeconomic outcome. *Open Orthop J*, 5:193–7, 2011.

[3] J. R. Arron and Y. Choi. Bone versus immune system. *Nature*, 408(6812):535–6, 2000.

[4] S. Reinke, S. Geissler, W. R. Taylor, K. Schmidt-Bleek, K. Juelke, V. Schwachmeyer, M. Dahne, T. Hartwig, L. Akyuz, C. Meisel, N. Unterwalder, N. B. Singh, P. Reinke, N. P. Haas, H. D. Volk, and G. N. Duda. Terminally differentiated CD8(+) T cells negatively affect bone regeneration in humans. *Sci Transl Med*, 5(177):177ra36, 2013.

[5] C. Schlundt, T. El Khassawna, A. Serra, A. Dienelt, S. Wendler, H. Schell, N. van Rooijen, A. Radbruch, R. Lucius, S. Hartmann, G. N. Duda, and K. Schmidt-Bleek. Macrophages in bone fracture healing: Their essential role in endochondral ossification. *Bone*, 2015.

[6] A. Barbul, R. J. Breslin, J. P. Woodyard, H. L. Wasserkrug, and G. Efron. The effect of in vivo T helper and T suppressor lymphocyte depletion on wound healing. *Ann Surg*, 209(4):479–83, 1989.

[7] C. J. Hauser, X. Zhou, P. Joshi, M. A. Cuchens, P. Kregor, M. Devidas, R. J. Kennedy, G. V. Poole, and J. L. Hughes. The immune microenvironment of human fracture/soft-tissue hematomas and its relationship to systemic immunity. *J Trauma*, 42(5):895–903; discussion 903–4, 1997.

[8] I. Konnecke, A. Serra, T. El Khassawna, C. Schlundt, H. Schell, A. Hauser, A. Ellinghaus, H. D. Volk, A. Radbruch, G. N. Duda, and K. Schmidt-Bleek. T and B cells participate in bone repair by infiltrating the fracture callus in a two-wave fashion. *Bone*, 64:155–65, 2014.

[9] A. A. Naik, C. Xie, M. J. Zuscik, P. Kingsley, E. M. Schwarz, H. Awad, R. Guldberg, H. Drissi, J. E. Puzas, B. Boyce, X. Zhang, and R. J. O'Keefe. Reduced COX-2 expression in aged mice is associated with impaired fracture healing. *J Bone Miner Res*, 24(2):251–64, 2009.

[10] K. Schmidt-Bleek, H. Schell, P. Kolar, M. Pfaff, C. Perka, F. Buttgereit, G. Duda, and J. Lienau. Cellular composition of the initial fracture hematoma compared to a muscle hematoma: a study in sheep. *J Orthop Res*, 27(9):1147–51, 2009.

[11] K. Schmidt-Bleek, A. Petersen, A. Dienelt, C. Schwarz, and G. N. Duda. Initiation and early control of tissue regeneration - bone healing as a model system for tissue regeneration. *Expert Opin Biol Ther*, 14(2):247–59, 2014.

[12] C. Schlundt, H. Schell, S. B. Goodman, G. Vunjak-Novakovic, G. N. Duda, and K. Schmidt-Bleek. Immune modulation as a therapeutic strategy in bone regeneration. *Journal of experimental orthopaedics*, 2(1):1, 2015.

[13] J. E. Efron, H. L. Frankel, S. A. Lazarou, H. L. Wasserkrug, and A. Barbul. Wound healing and T-lymphocytes. *J Surg Res*, 48(5):460–3, 1990.

[14] M. M. Zaiss, R. Axmann, J. Zwerina, K. Polzer, E. Guckel, A. Skapenko, H. Schulze-Koops, N. Horwood, A. Cope, and G. Schett. Treg cells suppress osteoclast formation: a new link between the immune system and bone. *Arthritis Rheum*, 56(12):4104–12, 2007.

[15] M. M. Zaiss, K. Sarter, A. Hess, K. Engelke, C. Bohm, F. Nimmerjahn, R. Voll, G. Schett, and J. P. David. Increased bone density and resistance to ovariectomy-induced bone loss in FoxP3-transgenic mice based on impaired osteoclast differentiation. *Arthritis Rheum*, 62(8):2328–38, 2010.

[16] M. M. Zaiss, B. Frey, A. Hess, J. Zwerina, J. Luther, F. Nimmerjahn, K. Engelke, G. Kollias, T. Hunig, G. Schett, and J. P. David. Regulatory T cells protect from local and systemic bone destruction in arthritis. *J Immunol*, 184(12):7238–46, 2010.

[17] Y. Liu, L. Wang, T. Kikuiri, K. Akiyama, C. Chen, X. Xu, R. Yang, W. Chen, S. Wang, and S. Shi. Mesenchymal stem cell-based tissue regeneration is governed by recipient T lymphocytes via IFN-gamma and TNF-alpha. *Nat Med*, 17(12):1594–601, 2011.

[18] K. Schmidt-Bleek, H. Schell, J. Lienau, N. Schulz, P. Hoff, M. Pfaff, G. Schmidt, C. Martin, C. Perka, F. Buttgereit, H. D. Volk, and G. Duda. Initial immune reaction and angiogenesis in bone healing. *J Tissue Eng Regen Med*, 8(2):120–30, 2014.

[19] D. Pennig. [the biology of bones and of bone fracture healing]. *Unfallchirurg*, 93(11):488–91, 1990.

[20] G. A. Rodan. Introduction to bone biology. *Bone*, 13 Suppl 1:S3–6, 1992.

[21] H. K. Datta, W. F. Ng, J. A. Walker, S. P. Tuck, and S. S. Varanasi. The cell biology of bone metabolism. *J Clin Pathol*, 61(5):577–87, 2008.

[22] A. Remedios. Bone and bone healing. *Vet Clin North Am Small Anim Pract*, 29(5):1029–44, v, 1999.

[23] J. A. Buckwalter, M. J. Glimcher, R. R. Cooper, and R. Recker. Bone biology. I: Structure, blood supply, cells, matrix, and mineralization. *Instr Course Lect*, 45:371–86, 1996.

[24] J. Wolff. Das Gesetzt der Transformation der Knochen. *Hirschwald Verlag, Berlin*, 1892.

[25] M. Capulli, R. Paone, and N. Rucci. Osteoblast and osteocyte: games without frontiers. *Arch Biochem Biophys*, 561:3–12, 2014.

[26] S. L. Dallas and L. F. Bonewald. Dynamics of the transition from osteoblast to osteocyte. *Ann N Y Acad Sci*, 1192:437–43, 2010.

[27] S. C. Miller, L. de Saint-Georges, B. M. Bowman, and W. S. Jee. Bone lining cells: structure and function. *Scanning Microsc*, 3(3):953–60; discussion 960–1, 1989.

[28] V. Everts, J. M. Delaisse, W. Korper, D. C. Jansen, W. Tigchelaar-Gutter, P. Saftig, and W. Beertsen. The bone lining cell: its role in cleaning Howship's lacunae and initiating bone formation. *J Bone Miner Res*, 17(1):77–90, 2002.

[29] T. A. Franz-Odendaal, B. K. Hall, and P. E. Witten. Buried alive: how osteoblasts become osteocytes. *Dev Dyn*, 235(1):176–90, 2006.

[30] L. F. Bonewald. Osteocytes as dynamic multifunctional cells. *Ann N Y Acad Sci*, 1116:281–90, 2007.

[31] S. Khosla. Minireview: the OPG/RANKL/RANK system. *Endocrinology*, 142(12):5050–5, 2001.

[32] M. Mulari, J. Vaaraniemi, and H. K. Vaananen. Intracellular membrane trafficking in bone resorbing osteoclasts. *Microsc Res Tech*, 61(6):496–503, 2003.

[33] V. E. Arana-Chavez and V. Bradaschia-Correa. Clastic cells: mineralized tissue resorption in health and disease. *Int J Biochem Cell Biol*, 41(3):446–50, 2009.

[34] W. J. Boyle, W. S. Simonet, and D. L. Lacey. Osteoclast differentiation and activation. *Nature*, 423(6937):337–42, 2003.

[35] L. C. Gerstenfeld, Y. M. Alkhiary, E. A. Krall, F. H. Nicholls, S. N. Stapleton, J. L. Fitch, M. Bauer, R. Kayal, D. T. Graves, K. J. Jepsen, and T. A. Einhorn. Three-dimensional reconstruction of fracture callus morphogenesis. *J Histochem Cytochem*, 54(11):1215–28, 2006.

[36] R. Marsell and T. A. Einhorn. The biology of fracture healing. *Injury*, 42(6):551–5, 2011.

[37] R. E. Kaderly. Primary bone healing. *Semin Vet Med Surg (Small Anim)*, 6(1):21–5, 1991.

[38] K. Mizuno, K. Mineo, T. Tachibana, M. Sumi, T. Matsubara, and K. Hirohata. The osteogenetic potential of fracture haematoma. Subperiosteal and intramuscular transplantation of the haematoma. *J Bone Joint Surg Br*, 72(5):822–9, 1990.

[39] S. H. Park, M. Silva, W. J. Bahk, H. McKellop, and J. R. Lieberman. Effect of repeated irrigation and debridement on fracture healing in an animal model. *J Orthop Res*, 20(6):1197–204, 2002.

[40] P. Kolar, K. Schmidt-Bleek, H. Schell, T. Gaber, D. Toben, G. Schmidmaier, C. Perka, F. Buttgereit, and G. N. Duda. The early fracture hematoma and its potential role in fracture healing. *Tissue Eng Part B Rev*, 16(4):427–34, 2010.

[41] J. Lienau, K. Schmidt-Bleek, A. Peters, F. Haschke, G. N. Duda, C. Perka, H. J. Bail, N. Schutze, F. Jakob, and H. Schell. Differential regulation of blood vessel formation between standard and delayed bone healing. *J Orthop Res*, 27(9):1133–40, 2009.

[42] L. C. Gerstenfeld, T. J. Cho, T. Kon, T. Aizawa, A. Tsay, J. Fitch, G. L. Barnes, D. T. Graves, and T. A. Einhorn. Impaired fracture healing in the absence of TNF-alpha signaling: the role of TNF-alpha in endochondral cartilage resorption. *J Bone Miner Res*, 18(9):1584–92, 2003.

[43] J. A. Kanis, O. Johnell, A. Oden, H. Johansson, C. De Laet, J. A. Eisman, S. Fujiwara, H. Kroger, E. V. McCloskey, D. Mellstrom, L. J. Melton, H. Pols, J. Reeve, A. Silman, and A. Tenenhouse. Smoking and fracture risk: a meta-analysis. *Osteoporos Int*, 16(2):155–62, 2005.

[44] P. Vestergaard, L. Rejnmark, and L. Mosekilde. Relative fracture risk in patients with diabetes mellitus, and the impact of insulin and oral antidiabetic medication on relative fracture risk. *Diabetologia*, 48(7):1292–9, 2005.

[45] K. E. Ensrud. Epidemiology of fracture risk with advancing age. *J Gerontol A Biol Sci Med Sci*, 68(10):1236–42, 2013.

[46] T. A. Einhorn and L. C. Gerstenfeld. Fracture healing: mechanisms and interventions. *Nat Rev Rheumatol*, 11(1):45–54, 2015.

[47] R. Fu, S. Selph, M. McDonagh, K. Peterson, A. Tiwari, R. Chou, and M. Helfand. Effectiveness and harms of recombinant human bone morphogenetic protein-2 in spine fusion: a systematic review and meta-analysis. *Ann Intern Med*, 158(12):890–902, 2013.

[48] P. Peichl, L. A. Holzer, R. Maier, and G. Holzer. Parathyroid hormone 1-84 accelerates fracture-healing in pubic bones of elderly osteoporotic women. *J Bone Joint Surg Am*, 93(17):1583–7, 2011.

[49] T. K. Kovach, A. S. Dighe, P. I. Lobo, and Q. Cui. Interactions between MSCs and immune cells: implications for bone healing. *J Immunol Res*, 2015:752510, 2015.

[50] R. Quarto, M. Mastrogiacomo, R. Cancedda, S. M. Kutepov, V. Mukhachev, A. Lavroukov, E. Kon, and M. Marcacci. Repair of large bone defects with the use of autologous bone marrow stromal cells. *N Engl J Med*, 344(5):385–6, 2001.

[51] I. Fernandez-Bances, M. Perez-Basterrechea, S. Perez-Lopez, D. Nunez Batalla, M. A. Fernandez Rodriguez, M. Alvarez-Viejo, A. Ferrero-Gutierrez, Y. Menendez-Menendez, J. M. Garcia-Gala, D. Escudero, J. Paz Aparicio, S. Carnero Lopez, P. Lopez Fernandez, D. Gonzalez Suarez, and J. Otero Hernandez. Repair of long-bone pseudoarthrosis with autologous bone marrow mononuclear cells combined with allogenic bone graft. *Cytotherapy*, 15(5):571–7, 2013.

[52] E. Gomez-Barrena, P. Rosset, D. Lozano, J. Stanovici, C. Ermthaller, and F. Gerbhard. Bone fracture healing: cell therapy in delayed unions and nonunions. *Bone*, 70:93–101, 2015.

[53] P. F. O'Loughlin, S. Morr, L. Bogunovic, A. D. Kim, B. Park, and J. M. Lane. Selection and development of preclinical models in fracture-healing research. *J Bone Joint Surg Am*, 90 Suppl 1:79–84, 2008.

[54] F. Roch and M. A. Bach. Strain differences in mouse cellular responses to Mycobacterium lepraemurium and BCG subcutaneous infections. II. Production of interleukins 2, 4, and 6 and of interferon-gamma by draining lymph node cells. *Clin Immunol Immunopathol*, 60(3):443–54, 1991.

[55] M. B. Manigrasso and J. P. O'Connor. Comparison of fracture healing among different inbred mouse strains. *Calcif Tissue Int*, 82(6):465–74, 2008.

[56] H. Takayanagi. SnapShot: Osteoimmunology. *Cell Metab*, 21(3):502 e1, 2015.

[57] R. S. Taichman and S. G. Emerson. Human osteoblasts support hematopoiesis through the production of granulocyte colony-stimulating factor. *J Exp Med*, 179(5):1677–82, 1994.

[58] S. J. Morrison and D. T. Scadden. The bone marrow niche for haematopoietic stem cells. *Nature*, 505(7483):327–34, 2014.

[59] P. W. Price and J. Cerny. Characterization of CD4+ T cells in mouse bone marrow. I. Increased activated/memory phenotype and altered TCR Vbeta repertoire. *Eur J Immunol*, 29(3):1051–6, 1999.

[60] P. C. Sandel, M. Gendelman, G. Kelsoe, and J. G. Monroe. Definition of a novel cellular constituent of the bone marrow that regulates the response of immature B cells to B cell antigen receptor engagement. *J Immunol*, 166(10):5935–44, 2001.

[61] I. B. Mazo, M. Honczarenko, H. Leung, L. L. Cavanagh, R. Bonasio, W. Weninger, K. Engelke, L. Xia, R. P. McEver, P. A. Koni, L. E. Silberstein, and U. H. von Andrian. Bone marrow is a major reservoir and site of recruitment for central memory CD8+ T cells. *Immunity*, 22(2):259–70, 2005.

[62] J. E. Horton, L. G. Raisz, H. A. Simmons, J. J. Oppenheim, and S. E. Mergenhagen. Bone resorbing activity in supernatant fluid from cultured human peripheral blood leukocytes. *Science*, 177(4051):793–5, 1972.

[63] M. Horowitz, A. Vignery, R. K. Gershon, and R. Baron. Thymus-derived lymphocytes and their interactions with macrophages are required for the production of osteoclast-activating factor in the mouse. *Proc Natl Acad Sci U S A*, 81(7):2181–5, 1984.

[64] H. Takayanagi, K. Ogasawara, S. Hida, T. Chiba, S. Murata, K. Sato, A. Takaoka, T. Yokochi, H. Oda, K. Tanaka, K. Nakamura, and T. Taniguchi. T-cell-mediated regulation of osteoclastogenesis by signalling cross-talk between RANKL and IFN-gamma. *Nature*, 408(6812):600–5, 2000.

[65] H. Takayanagi. Osteoimmunology and the effects of the immune system on bone. *Nat Rev Rheumatol*, 5(12):667–76, 2009.

[66] K. Sato, A. Suematsu, K. Okamoto, A. Yamaguchi, Y. Morishita, Y. Kadono, S. Tanaka, T. Kodama, S. Akira, Y. Iwakura, D. J. Cua, and H. Takayanagi. Th17 functions as an osteoclastogenic helper T cell subset that links T cell activation and bone destruction. *J Exp Med*, 203(12):2673–82, 2006.

[67] Jr. Janeway, C. A. and R. Medzhitov. Innate immune recognition. *Annu Rev Immunol*, 20:197–216, 2002.

[68] D. G. Hesslein and D. G. Schatz. Factors and forces controlling V(D)J recombination. *Adv Immunol*, 78:169–232, 2001.

[69] Y. H. Chien and R. Jores. Gamma delta T cells. T cells with B-cell-like recognition properties. *Curr Biol*, 5(10):1116–8, 1995.

[70] C. Viret and Jr. Janeway, C. A. MHC and T cell development. *Rev Immunogenet*, 1(1):91–104, 1999.

[71] S. L. Swain, M. Croft, C. Dubey, L. Haynes, P. Rogers, X. Zhang, and L. M. Bradley. From naive to memory T cells. *Immunol Rev*, 150:143–67, 1996.

[72] S. M. Kaech and R. Ahmed. Memory CD8+ T cell differentiation: initial antigen encounter triggers a developmental program in naive cells. *Nat Immunol*, 2(5):415–22, 2001.

[73] R. V. Luckheeram, R. Zhou, A. D. Verma, and B. Xia. CD4(+)T cells: differentiation and functions. *Clin Dev Immunol*, 2012:925135, 2012.

[74] F. Sallusto, D. Lenig, R. Forster, M. Lipp, and A. Lanzavecchia. Two subsets of memory T lymphocytes with distinct homing potentials and effector functions. *Nature*, 401(6754):708–12, 1999.

[75] O. Bjorkdahl, K. A. Barber, S. J. Brett, M. G. Daly, C. Plumpton, N. A. Elshourbagy, J. P. Tite, and L. L. Thomsen. Characterization of CC-chemokine receptor 7 expression on murine T cells in lymphoid tissues. *Immunology*, 110(2):170–9, 2003.

[76] J. D. Fontenot, M. A. Gavin, and A. Y. Rudensky. Foxp3 programs the development and function of CD4+CD25+ regulatory T cells. *Nat Immunol*, 4(4):330–6, 2003.

[77] S. Hori, T. Nomura, and S. Sakaguchi. Control of regulatory T cell development by the transcription factor Foxp3. *Science*, 299(5609):1057–61, 2003.

[78] A. M. Bilate and J. J. Lafaille. Induced CD4+Foxp3+ regulatory T cells in immune tolerance. *Annu Rev Immunol*, 30:733–58, 2012.

[79] S. Floess, J. Freyer, C. Siewert, U. Baron, S. Olek, J. Polansky, K. Schlawe, H.-D. Chang, T. Bopp, E. Schmitt, et al. Epigenetic control of the foxp3 locus in regulatory T cells. *PLoS Biol*, 5(2):e38, 2007.

[80] S. Sakaguchi, T. Takahashi, and Y. Nishizuka. Study on cellular events in post-thymectomy autoimmune oophoritis in mice. II. Requirement of Lyt-1 cells in normal female mice for the prevention of oophoritis. *J Exp Med*, 156(6):1577–86, 1982.

[81] S. Sakaguchi, N. Sakaguchi, M. Asano, M. Itoh, and M. Toda. Immunologic self-tolerance maintained by activated T cells expressing IL-2 receptor alpha-chains (CD25). Breakdown of a single mechanism of self-tolerance causes various autoimmune diseases. *J Immunol*, 155(3):1151–64, 1995.

[82] L. B. Clark, M. W. Appleby, M. E. Brunkow, J. E. Wilkinson, S. F. Ziegler, and F. Ramsdell. Cellular and molecular characterization of the scurfy mouse mutant. *J Immunol*, 162(5):2546–54, 1999.

[83] C. L. Bennett, J. Christie, F. Ramsdell, M. E. Brunkow, P. J. Ferguson, L. Whitesell, T. E. Kelly, F. T. Saulsbury, P. F. Chance, and H. D. Ochs. The immune dysregulation, polyendocrinopathy, enteropathy, X-linked syndrome (IPEX) is caused by mutations of FOXP3. *Nat Genet*, 27(1):20–1, 2001.

[84] M. E. Brunkow, E. W. Jeffery, K. A. Hjerrild, B. Paeper, L. B. Clark, S. A. Yasayko, J. E. Wilkinson, D. Galas, S. F. Ziegler, and F. Ramsdell. Disruption of a new forkhead/winged-helix protein, scurfin, results in the fatal lymphoproliferative disorder of the scurfy mouse. *Nat Genet*, 27(1):68–73, 2001.

[85] M. S. Jordan, A. Boesteanu, A. J. Reed, A. L. Petrone, A. E. Holenbeck, M. A. Lerman, A. Naji, and A. J. Caton. Thymic selection of CD4+CD25+ regulatory T cells induced by an agonist self-peptide. *Nat Immunol*, 2(4):301–6, 2001.

[86] E. M. Shevach. From vanilla to 28 flavors: multiple varieties of T regulatory cells. *Immunity*, 25(2):195–201, 2006.

[87] T. Bopp, C. Becker, M. Klein, S. Klein-Hessling, A. Palmetshofer, E. Serfling, V. Heib, M. Becker, J. Kubach, S. Schmitt, S. Stoll, H. Schild, M. S. Staege, M. Stassen, H. Jonuleit, and E. Schmitt. Cyclic adenosine monophosphate is a key component of regulatory T cell-mediated suppression. *J Exp Med*, 204(6):1303–10, 2007.

[88] S. Deaglio, K. M. Dwyer, W. Gao, D. Friedman, A. Usheva, A. Erat, J. F. Chen, K. Enjyoji, J. Linden, M. Oukka, V. K. Kuchroo, T. B. Strom, and S. C. Robson. Adenosine generation catalyzed by CD39 and CD73 expressed on regulatory T cells mediates immune suppression. *J Exp Med*, 204(6):1257–65, 2007.

[89] S. Huang, S. Apasov, M. Koshiba, and M. Sitkovsky. Role of A2a extracellular adenosine receptor-mediated signaling in adenosine-mediated inhibition of T-cell activation and expansion. *Blood*, 90(4):1600–10, 1997.

[90] W. J. Grossman, J. W. Verbsky, W. Barchet, M. Colonna, J. P. Atkinson, and T. J. Ley. Human T regulatory cells can use the perforin pathway to cause autologous target cell death. *Immunity*, 21(4):589–601, 2004.

[91] D. C. Gondek, L. F. Lu, S. A. Quezada, S. Sakaguchi, and R. J. Noelle. Cutting edge: contact-mediated suppression by CD4+CD25+ regulatory cells involves a granzyme B-dependent, perforin-independent mechanism. *J Immunol*, 174(4):1783–6, 2005.

[92] H. Y. Qin, R. Mukherjee, E. Lee-Chan, C. Ewen, R. C. Bleackley, and B. Singh. A novel mechanism of regulatory T cell-mediated down-regulation of autoimmunity. *Int Immunol*, 18(7):1001–15, 2006.

[93] Q. Tang, J. Y. Adams, A. J. Tooley, M. Bi, B. T. Fife, P. Serra, P. Santamaria, R. M. Locksley, M. F. Krummel, and J. A. Bluestone. Visualizing regulatory T cell control of autoimmune responses in nonobese diabetic mice. *Nat Immunol*, 7(1):83–92, 2006.

[94] D. M. Zhao, A. M. Thornton, R. J. DiPaolo, and E. M. Shevach. Activated CD4+CD25+ T cells selectively kill B lymphocytes. *Blood*, 107(10):3925–32, 2006.

[95] F. Fallarino, U. Grohmann, K. W. Hwang, C. Orabona, C. Vacca, R. Bianchi, M. L. Belladonna, M. C. Fioretti, M. L. Alegre, and P. Puccetti. Modulation of tryptophan catabolism by regulatory T cells. *Nat Immunol*, 4(12):1206–12, 2003.

[96] P. Puccetti and U. Grohmann. IDO and regulatory T cells: a role for reverse signalling and non-canonical NF-kappaB activation. *Nat Rev Immunol*, 7(10):817–23, 2007.

[97] M. Feuerer, N. Kamei, D. Cipolletta, A. Li, J. Lee, S. E . Shoelson, C. O. Benoist, and D. J. Mathis. PPARγ is a Major Driver of the Accumulation and Phenotype of Adipose-Tissue Treg Cells. 2012.

[98] D. Burzyn, W. Kuswanto, D. Kolodin, J. L. Shadrach, M. Cerletti, Y. Jang, E. Sefik, T. G. Tan, A. J. Wagers, C. Benoist, et al. A special population of regulatory T cells potentiates muscle repair. *Cell*, 155(6):1282–1295, 2013.

[99] H. Lei, K. Schmidt-Bleek, A. Dienelt, P. Reinke, and H. D. Volk. Regulatory T cell-mediated anti-inflammatory effects promote successful tissue repair in both indirect and direct manners. *Front Pharmacol*, 6:184, 2015.

[100] A. Mantovani, A. Sica, S. Sozzani, P. Allavena, A. Vecchi, and M. Locati. The chemokine system in diverse forms of macrophage activation and polarization. *Trends Immunol*, 25(12):677–86, 2004.

[101] D. Toben, I. Schroeder, T. El Khassawna, M. Mehta, J. E. Hoffmann, J. T. Frisch, H. Schell, J. Lienau, A. Serra, A. Radbruch, and G. N. Duda. Fracture healing is accelerated in the absence of the adaptive immune system. *J Bone Miner Res*, 26(1):113–24, 2011.

[102] S. Kotake, N. Udagawa, N. Takahashi, K. Matsuzaki, K. Itoh, S. Ishiyama, S. Saito, K. Inoue, N. Kamatani, M. T. Gillespie, T. J. Martin, and T. Suda. IL-17 in synovial fluids from patients with rheumatoid arthritis is a potent stimulator of osteoclastogenesis. *J Clin Invest*, 103(9):1345–52, 1999.

[103] M. Croes, F. C. Oner, D. van Neerven, E. Sabir, M. C. Kruyt, T. J. Blokhuis, W. J. Dhert, and J. Alblas. Proinflammatory T cells and IL-17 stimulate osteoblast differentiation. *Bone*, 84:262–70, 2016.

[104] Q. Niu, B. Cai, Z. C. Huang, Y. Y. Shi, and L. L. Wang. Disturbed Th17/Treg balance in patients with rheumatoid arthritis. *Rheumatol Int*, 32(9):2731–6, 2012.

[105] A. M. Tyagi, K. Srivastava, M. N. Mansoori, R. Trivedi, N. Chattopadhyay, and D. Singh. Estrogen deficiency induces the differentiation of IL-17 secreting Th17 cells: a new candidate in the pathogenesis of osteoporosis. *PLoS One*, 7(9):e44552, 2012.

[106] M. Mehta, H. Schell, C. Schwarz, A. Peters, K. Schmidt-Bleek, A. Ellinghaus, H. J. Bail, G. N. Duda, and J. Lienau. A 5-mm femoral defect in female but not in male rats leads to a reproducible atrophic non-union. *Arch Orthop Trauma Surg*, 131(1):121–9, 2011.

[107] P. Strube, M. Mehta, A. Baerenwaldt, J. Trippens, C. J. Wilson, A. Ode, C. Perka, G. N. Duda, and G. Kasper. Sex-specific compromised bone healing in female rats might be associated with a decrease in mesenchymal stem cell quantity. *Bone*, 45(6):1065–72, 2009.

[108] M. D. Brodt, C. B. Ellis, and M. J. Silva. Growing C57Bl/6 mice increase whole bone mechanical properties by increasing geometric and material properties. *J Bone Miner Res*, 14(12):2159–66, 1999.

[109] D. J. Recktenwald. Introduction to flow cytometry: principles, fluorochromes, instrument set-up, calibration. *J Hematother*, 2(3):387–94, 1993.

[110] S. Miltenyi, W. Muller, W. Weichel, and A. Radbruch. High gradient magnetic cell separation with MACS. *Cytometry*, 11(2):231–8, 1990.

[111] A. M. Thornton and E. M. Shevach. CD4+CD25+ immunoregulatory T cells suppress polyclonal T cell activation in vitro by inhibiting interleukin 2 production. *J Exp Med*, 188(2):287–96, 1998.

[112] L. W. Collison and D. A. Vignali. In vitro Treg suppression assays. *Methods Mol Biol*, 707:21–37, 2011.

[113] T. Kawamoto. Light microscopic autoradiography for study of early changes in the distribution of water-soluble materials. *J Histochem Cytochem*, 38(12):1805–14, 1990.

[114] T. Kawamoto. Use of a new adhesive film for the preparation of multi-purpose fresh-frozen sections from hard tissues, whole-animals, insects and plants. *Arch Histol Cytol*, 66(2):123–43, 2003.

[115] H. Z. Movat. Demonstration of all connective tissue elements in a single section; pentachrome stains. *AMA Arch Pathol*, 60(3):289–95, 1955.

[116] J. M. Lucocq and J. Roth. Applications of immunocolloids in light microscopy. III. Demonstration of antigenic and lectin-binding sites in semithin resin sections. *J Histochem Cytochem*, 32(10):1075–83, 1984.

[117] A. H. Coons and M. H. Kaplan. Localization of antigen in tissue cells; improvements in a method for the detection of antigen by means of fluorescent antibody. *J Exp Med*, 91(1):1–13, 1950.

[118] A. H. Coons. The development of immunohistochemistry. *Ann N Y Acad Sci*, 177:5–9, 1971.

[119] L. A. Feldkamp, S. A. Goldstein, A. M. Parfitt, G. Jesion, and M. Kleerekoper. The direct examination of three-dimensional bone architecture in vitro by computed tomography. *J Bone Miner Res*, 4(1):3–11, 1989.

[120] M. L. Bouxsein, S. K. Boyd, B. A. Christiansen, R. E. Guldberg, K. J. Jepsen, and R. Muller. Guidelines for assessment of bone microstructure in rodents using micro-computed tomography. *J Bone Miner Res*, 25(7):1468–86, 2010.

[121] R. Muller, M. Hahn, M. Vogel, G. Delling, and P. Ruegsegger. Morphometric analysis of noninvasively assessed bone biopsies: comparison of high-resolution computed tomography and histologic sections. *Bone*, 18(3):215–20, 1996.

[122] M. A. Curotto de Lafaille and J. J. Lafaille. Natural and adaptive foxp3+ regulatory T cells: more of the same or a division of labor? *Immunity*, 30(5):626–35, 2009.

[123] X. Lin, M. Chen, Y. Liu, Z. Guo, X. He, D. Brand, and S. G. Zheng. Advances in distinguishing natural from induced Foxp3(+) regulatory T cells. *Int J Clin Exp Pathol*, 6(2):116–23, 2013.

[124] C. G. Brunstein, J. S. Miller, Q. Cao, D. H. McKenna, K. L. Hippen, J. Curtsinger, T. Defor, B. L. Levine, C. H. June, P. Rubinstein, P. B. McGlave, B. R. Blazar, and J. E. Wagner. Infusion of ex vivo expanded T regulatory cells in adults transplanted with umbilical cord blood: safety profile and detection kinetics. *Blood*, 117(3):1061–70, 2011.

[125] N. Marek-Trzonkowska, M. Mysliwiec, A. Dobyszuk, M. Grabowska, I. Techmanska, J. Juscinska, M. A. Wujtewicz, P. Witkowski, W. Mlynarski, A. Balcerska, J. Mysliwska, and P. Trzonkowski. Administration of CD4+CD25highCD127- regulatory T cells preserves beta-cell function in type 1 diabetes in children. *Diabetes Care*, 35(9):1817–20, 2012.

[126] P. Trzonkowski, M. Bieniaszewska, J. Juscinska, A. Dobyszuk, A. Krzystyniak, N. Marek, J. Mysliwska, and A. Hellmann. First-in-man clinical results of the treatment of patients with graft versus host disease with human ex vivo expanded CD4+CD25+CD127- T regulatory cells. *Clin Immunol*, 133(1):22–6, 2009.

[127] K. Lahl, C. Loddenkemper, C. Drouin, J. Freyer, J. Arnason, G. Eberl, A. Hamann, H. Wagner, J. Huehn, and T. Sparwasser. Selective depletion of Foxp3+ regulatory T cells induces a scurfy-like disease. *J Exp Med*, 204(1):57–63, 2007.

[128] E. Jones, M. Dahm-Vicker, A. K. Simon, A. Green, F. Powrie, V. Cerundolo, and A. Gallimore. Depletion of CD25+ regulatory cells results in suppression of melanoma growth and induction of autoreactivity in mice. *Cancer Immun*, 2:1, 2002.

[129] W. Li, K. Carper, Y. Liang, X. X. Zheng, C. S. Kuhr, J. D. Reyes, D. L. Perkins, A. W. Thomson, and J. D. Perkins. Anti-CD25 mAb administration prevents spontaneous liver transplant tolerance. *Transplant Proc*, 38(10):3207–8, 2006.

[130] R. Rad, L. Brenner, S. Bauer, S. Schwendy, L. Layland, C. P. da Costa, W. Reindl, A. Dossumbekova, M. Friedrich, D. Saur, H. Wagner, R. M. Schmid, and C. Prinz. CD25+/Foxp3+ T cells regulate gastric inflammation and Helicobacter pylori colonization in vivo. *Gastroenterology*, 131(2):525–37, 2006.

[131] L. J. Raggatt, M. E. Wullschleger, K. A. Alexander, A. C. Wu, S. M. Millard, S. Kaur, M. L. Maugham, L. S. Gregory, R. Steck, and A. R. Pettit. Fracture healing via periosteal callus formation requires macrophages for both initiation and progression of early endochondral ossification. *Am J Pathol*, 184(12):3192–204, 2014.

[132] S. M. Opal. Phylogenetic and functional relationships between coagulation and the innate immune response. *Crit Care Med*, 28(9 Suppl):S77–80, 2000.

[133] S. M. Abdelmagid, M. F. Barbe, and F. F. Safadi. Role of inflammation in the aging bones. *Life Sci*, 123:25–34, 2015.

[134] K. L. Spiller, R. R. Anfang, K. J. Spiller, J. Ng, K. R. Nakazawa, J. W. Daulton, and G. Vunjak-Novakovic. The role of macrophage phenotype in vascularization of tissue engineering scaffolds. *Biomaterials*, 35(15):4477–88, 2014.

[135] G. Mori, P. D'Amelio, R. Faccio, and G. Brunetti. Bone-immune cell crosstalk: bone diseases. *J Immunol Res*, 2015:108451, 2015.

[136] L. Rifas. T-cell cytokine induction of BMP-2 regulates human mesenchymal stromal cell differentiation and mineralization. *J Cell Biochem*, 98(4):706–14, 2006.

[137] E. Faist, C. Schinkel, and S. Zimmer. Update on the mechanisms of immune suppression of injury and immune modulation. *World J Surg*, 20(4):454–9, 1996.

[138] N. Ni Choileain, M. MacConmara, Y. Zang, T. J. Murphy, J. A. Mannick, and J. A. Lederer. Enhanced regulatory T cell activity is an element of the host response to injury. *J Immunol*, 176(1):225–36, 2006.

[139] J. A. Lederer, M. L. Rodrick, and J. A. Mannick. The effects of injury on the adaptive immune response. *Shock*, 11(3):153–9, 1999.

[140] V. E. Strong, P. J. Mackrell, E. M. Concannon, H. A. Naama, P. A. Schaefer, G. W. Shaftan, P. P. Stapleton, and J. M. Daly. Blocking prostaglandin E2 after trauma attenuates pro-inflammatory cytokines and improves survival. *Shock*, 14(3):374–9, 2000.

[141] E. J. Wherry, V. Teichgraber, T. C. Becker, D. Masopust, S. M. Kaech, R. Antia, U. H. von Andrian, and R. Ahmed. Lineage relationship and protective immunity of memory CD8 T cell subsets. *Nat Immunol*, 4(3):225–34, 2003.

[142] F. Sallusto, J. Geginat, and A. Lanzavecchia. Central memory and effector memory T cell subsets: function, generation, and maintenance. *Annu Rev Immunol*, 22:745–63, 2004.

[143] K. J. Maloy, L. Salaun, R. Cahill, G. Dougan, N. J. Saunders, and F. Powrie. CD4+CD25+ T(R) cells suppress innate immune pathology through cytokine-dependent mechanisms. *J Exp Med*, 197(1):111–9, 2003.

[144] T. J. Murphy, N. Ni Choileain, Y. Zang, J. A. Mannick, and J. A. Lederer. CD4+CD25+ regulatory T cells control innate immune reactivity after injury. *J Immunol*, 174(5):2957–63, 2005.

[145] M. O. Al-Sebaei, D. M. Daukss, A. C. Belkina, S. Kakar, N. A. Wigner, D. Cusher, D. Graves, T. Einhorn, E. Morgan, and L. C. Gerstenfeld. Role of Fas and Treg Cells in Fracture Healing as Characterized in the Fas-Deficient (lpr) Mouse Model of Lupus. *Journal of Bone and Mineral Research*, 29(6):1478–1491, 2014.

[146] J. A. Pasco, M. A. Kotowicz, M. J. Henry, G. C. Nicholson, H. J. Spilsbury, J. D. Box, and H. G. Schneider. High-sensitivity C-reactive protein and fracture risk in elderly women. *JAMA*, 296(11):1353–5, 2006.

[147] J. A. Cauley, M. E. Danielson, R. M. Boudreau, K. Y. Forrest, J. M. Zmuda, M. Pahor, F. A. Tylavsky, S. R. Cummings, T. B. Harris, A. B. Newman, and A. B. C. Study Health. Inflammatory markers and incident fracture risk in older men and women: the Health Aging and Body Composition Study. *J Bone Miner Res*, 22(7):1088–95, 2007.

[148] R. Gruber, H. Koch, B. A. Doll, F. Tegtmeier, T. A. Einhorn, and J. O. Hollinger. Fracture healing in the elderly patient. *Exp Gerontol*, 41(11):1080–93, 2006.

[149] A. H. Kverneland, M. Streitz, E. Geissler, J. Hutchinson, K. Vogt, D. Boes, N. Niemann, A. E. Pedersen, S. Schlickeiser, and B. Sawitzki. Age and gender leucocytes variances and references values generated using the standardized ONE-Study protocol. *Cytometry A*, 89(6):543–64, 2016.

[150] D. F. Tough, P. Borrow, and J. Sprent. Induction of bystander T cell proliferation by viruses and type I interferon in vivo. *Science*, 272(5270):1947–50, 1996.

[151] C. Franceschi, M. Bonafe, S. Valensin, F. Olivieri, M. De Luca, E. Ottaviani, and G. De Benedictis. Inflamm-aging. An evolutionary perspective on immunosenescence. *Ann N Y Acad Sci*, 908:244–54, 2000.

[152] T. Takahashi, Y. Kuniyasu, M. Toda, N. Sakaguchi, M. Itoh, M. Iwata, J. Shimizu, and S. Sakaguchi. Immunologic self-tolerance maintained by CD25+CD4+ naturally anergic and suppressive T cells: induction of autoimmune disease by breaking their anergic/suppressive state. *Int Immunol*, 10(12):1969–80, 1998.

[153] M. Stassen, H. Jonuleit, C. Muller, M. Klein, C. Richter, T. Bopp, S. Schmitt, and E. Schmitt. Differential regulatory capacity of CD25+ T regulatory cells and preactivated CD25+ T regulatory cells on development, functional activation, and proliferation of Th2 cells. *J Immunol*, 173(1):267–74, 2004.

[154] X. Ren, F. Ye, Z. Jiang, Y. Chu, S. Xiong, and Y. Wang. Involvement of cellular death in TRAIL/DR5-dependent suppression induced by CD4(+)CD25(+) regulatory T cells. *Cell Death Differ*, 14(12):2076–84, 2007.

[155] Y. Y. Kong, U. Feige, I. Sarosi, B. Bolon, A. Tafuri, S. Morony, C. Capparelli, J. Li, R. Elliott, S. McCabe, T. Wong, G. Campagnuolo, E. Moran, E. R. Bogoch, G. Van, L. T. Nguyen, P. S. Ohashi, D. L. Lacey, E. Fish, W. J. Boyle, and J. M. Penninger. Activated T cells regulate bone loss and joint destruction in adjuvant arthritis through osteoprotegerin ligand. *Nature*, 402(6759):304–9, 1999.

[156] S. Cenci, G. Toraldo, M. N. Weitzmann, C. Roggia, Y. Gao, W. P. Qian, O. Sierra, and R. Pacifici. Estrogen deficiency induces bone loss by increasing T cell proliferation and lifespan through IFN-gamma-induced class II transactivator. *Proc Natl Acad Sci U S A*, 100(18):10405–10, 2003.

[157] A. McNally, G. R. Hill, T. Sparwasser, R. Thomas, and R. J. Steptoe. CD4+CD25+ regulatory T cells control CD8+ T-cell effector differentiation by modulating IL-2 homeostasis. *Proc Natl Acad Sci U S A*, 108(18):7529–34, 2011.

[158] K. Gobel, S. Bittner, N. Melzer, S. Pankratz, A. Dreykluft, M. K. Schuhmann, S. G. Meuth, and H. Wiendl. CD4(+) CD25(+) FoxP3(+) regulatory T cells suppress cytotoxicity of CD8(+) effector T cells: implications for their capacity to limit inflammatory central nervous system damage at the parenchymal level. *J Neuroinflammation*, 9:41, 2012.

[159] W. Kastenmuller, G. Gasteiger, N. Subramanian, T. Sparwasser, D. H. Busch, Y. Belkaid, I. Drexler, and R. N. Germain. Regulatory T cells selectively control CD8+ T cell effector pool size via IL-2 restriction. *J Immunol*, 187(6):3186–97, 2011.

[160] M. Murakami, A. Sakamoto, J. Bender, J. Kappler, and P. Marrack. CD25+CD4+ T cells contribute to the control of memory CD8+ T cells. *Proc Natl Acad Sci U S A*, 99(13):8832–7, 2002.

[161] F. M. Mbitikon-Kobo, M. Vocanson, M. C. Michallet, M. Tomkowiak, A. Cottalorda, G. S. Angelov, C. A. Coupet, S. Djebali, A. Marcais, B. Dubois, N. Bonnefoy-Berard, J. F. Nicolas, C. Arpin, and J. Marvel. Characterization of a CD44/CD122int memory CD8 T cell subset generated under sterile inflammatory conditions. *J Immunol*, 182(6):3846–54, 2009.

[162] L. Xu, A. Kitani, I. Fuss, and W. Strober. Cutting edge: regulatory T cells induce CD4+CD25-Foxp3- T cells or are self-induced to become Th17 cells in the absence of exogenous TGF-beta. *J Immunol*, 178(11):6725–9, 2007.

[163] X. O. Yang, R. Nurieva, G. J. Martinez, H. S. Kang, Y. Chung, B. P. Pappu, B. Shah, S. H. Chang, K. S. Schluns, S. S. Watowich, X. H. Feng, A. M. Jetten, and C. Dong. Molecular antagonism and plasticity of regulatory and inflammatory T cell programs. *Immunity*, 29(1):44–56, 2008.

[164] X. Zhou, S. L. Bailey-Bucktrout, L. T. Jeker, C. Penaranda, M. Martinez-Llordella, M. Ashby, M. Nakayama, W. Rosenthal, and J. A. Bluestone. Instability of the transcription factor Foxp3 leads to the generation of pathogenic memory T cells in vivo. *Nat Immunol*, 10(9):1000–7, 2009.

[165] Y. P. Rubtsov, R. E. Niec, S. Josefowicz, L. Li, J. Darce, D. Mathis, C. Benoist, and A. Y. Rudensky. Stability of the regulatory T cell lineage in vivo. *Science*, 329(5999):1667–71, 2010.

[166] F. Osorio, S. LeibundGut-Landmann, M. Lochner, K. Lahl, T. Sparwasser, G. Eberl, and C. Reis e Sousa. DC activated via dectin-1 convert Treg into IL-17 producers. *Eur J Immunol*, 38(12):3274–81, 2008.

[167] H. J. Koenen, R. L. Smeets, P. M. Vink, E. van Rijssen, A. M. Boots, and I. Joosten. Human CD25highFoxp3pos regulatory T cells differentiate into IL-17-producing cells. *Blood*, 112(6):2340–52, 2008.

[168] G. Beriou, C. M. Costantino, C. W. Ashley, L. Yang, V. K. Kuchroo, C. Baecher-Allan, and D. A. Hafler. IL-17-producing human peripheral regulatory T cells retain suppressive function. *Blood*, 113(18):4240–9, 2009.

[169] K. G. Elpek, C. Lacelle, N. P. Singh, E. S. Yolcu, and H. Shirwan. CD4+CD25+ T regulatory cells dominate multiple immune evasion mechanisms in early but not late phases of tumor development in a B cell lymphoma model. *J Immunol*, 178(11):6840–8, 2007.

[170] S. A. Quezada, K. S. Peggs, T. R. Simpson, Y. Shen, D. R. Littman, and J. P. Allison. Limited tumor infiltration by activated T effector cells restricts the therapeutic activity of regulatory T cell depletion against established melanoma. *J Exp Med*, 205(9):2125–38, 2008.

[171] K. N. Couper, P. A. Lanthier, G. Perona-Wright, L. W. Kummer, W. Chen, S. T. Smiley, M. Mohrs, and L. L. Johnson. Anti-CD25 antibody-mediated depletion of effector T cell populations enhances susceptibility of mice to acute but not chronic Toxoplasma gondii infection. *J Immunol*, 182(7):3985–94, 2009.